Millimetre-Wave Rotman Lens-Based Array Beamforming Networks for Next-Generation Wireless Subsystems

by

Ardavan Rahimian

A thesis submitted in partial fulfilment of the requirements

for the degree of Doctor of Philosophy

School of Electronic Engineering and Computer Science

Queen Mary University of London

London E1 4NS, United Kingdom

November 2018

© QUEEN MARY UNIVERSITY OF LONDON

Statement of Originality

I, ARDAVAN RAHIMIAN, confirm that the research included within this thesis is my own work or that where it has been carried out in collaboration with, or supported by others, that this is duly acknowledged below and my contribution indicated. Previously published material is also acknowledged.

I attest that I have exercised reasonable care to ensure that the work is original, and does not to the best of my knowledge break any UK law, infringe any third party's copyright or other Intellectual Property Right, or contain any confidential material.

I accept that the College has the right to use plagiarism detection software to check the electronic version of the thesis.

I confirm that this thesis has not been previously submitted for the award of a degree by this or any other university.

The copyright of this thesis rests with the author and no quotation from it or information derived from it may be published without the prior written consent of the author.

Signature: ARDAVAN RAHIMIAN

Date: November 2018

"Thoughts without content are empty, intuitions without concepts are blind.

The understanding cannot intuit anything, the senses cannot think anything.

Only from their union can knowledge arise."

–Critique of Pure Reason, Immanuel Kant

***To My Family*.**

Abstract

This thesis undertakes thorough analytical designs, as well as numerical and experimental performance evaluations, of millimetre-wave beamforming networks based on the Rotman lens-based feeding concept. The developed passive switched-beam networks are intended for operation in the 28-GHz and 60-GHz bands, covering the whole frequency ranges of 18–38 GHz and 50–70 GHz, respectively. The primary objective of this work is to investigate the feasibility of designing a number of high-performance and low-profile array beamformers. This has been accomplished based on the flexible liquid-crystal polymer substrates, for the potential deployment in the next-generation wireless communications. The developed lens devices, and their output characteristics, in terms of the scattering parameters, accuracy, device efficiency, and surface current distributions, have been comprehensively evaluated. Moreover, this has been extended to the detailed designs of the lens beamformers based on the four different proposed flexural cases, namely the concave-axial bending, convex-axial bending, concave-circumferential bending, and convex-circumferential bending. Each of the flexures has been analysed in detail, and the performance in terms of the linear progressive phase behaviour, as the primary figure of merit, has been reported. Furthermore, based on the conducted analytical designs and validations a prototype has been accurately fabricated, using the laser-centric radio frequency circuit structuring technique, and a setup has been further deployed to carry out the measurements. This has been done in order to validate the analytical results, as well as to demonstrate the experimental 28-GHz beamforming. The presented array beamformers outperform other existing millimetre-wave beamformers, to be potentially utilised as the efficient integrated units of the transceiver modules and large-scale antennas, mostly in the multiple-input multiple-output systems. Lastly, the developed lens beamformers provide the next-generation conformal and flexible subsystems with the essential functional requirements for the millimetre-wave beam steering mechanisms.

Acknowledgments

I would like to express my deepest thanks and sincere gratitude to my primary supervisor, Dr Yasir Alfadhl, for his patience, guidance, support, and encouragement, and for giving me the opportunity to carry out my PhD studies. His immense knowledge and profound vision truly enabled me to develop my research and critical thinking skills.

I would like to sincerely thank my second supervisor, Dr Akram Alomainy, for his persistent and enormously helpful technical support and guidance throughout this work. I feel very fortunate to have had the chance to work with him.

Moreover, I would like to thank Dr Khalid Z. Rajab, for contributing to my supervisory panel, and for his insightful and constructive suggestions that greatly improved this work.

My sincere appreciation goes to Dr Qammer H. Abbasi and Prof Clive G. Parini, for their great cooperation and support that enabled me to conduct the experimental stage of this work.

A special thanks to Dr Kamyar Mehran, for sharing with me his valuable professional and academic experiences, and for enduring scientific and intellectual conversations.

Many thanks go to Mrs Melissa Yeo, for her continued and kind advice and motivation, and for helping me progress through all the stages of my PhD studies.

I would also like to sincerely acknowledge Remcom Inc., for the great support regarding the provision of the software solutions for my research work.

Lastly, I would like to thank all my friends and colleagues for their kindness, enthusiasm, support, and friendship, and for making the Antennas Group a vibrant place to work.

Ardavan Rahimian

Mile End, London, UK

November 2018

Table of Contents

List of Figures

List of Abbreviations

5G	Fifth generation
AP	Access point
BFN	Beamforming network
BTS	Base transceiver station
DoA	Direction of arrival
EIRP	Effective isotropic radiated power
EM	Electromagnetic
FIT	Finite integration technique
LBA	Link budget analysis
LCP	Liquid-crystal polymer
LoS	Line-of-sight
MIMO	Multiple-input multiple-output
mm-wave	Millimetre-wave
NLoS	Non-line-of-sight
P2P	Point-to-point
PHY	Physical
RF	Radio frequency
RL	Rotman lens
Rx	Receiver
SLL	Sidelobe level
SNR	Signal-to-noise ratio
TTD	True-time-delay
TL	Transmission line
Tx	Transmitter

Chapter 1:

Introduction and Research Motivation

1.1 Introduction

In order to maintain the sustainability of advanced cellular networks, and to manage the potential system resources, it is crucial to develop the essential infrastructures for the optimal operation, and the efficient implementation of the next-generation intelligent solutions and services. In addition, to deploy the ultimate enhancements, it is of vital importance to rethink the fundamental improvements for the effective realisation of the future communication systems and radio frequency (RF) channels in the propagation media. The rapid increase in the data traffic volume as well as the usage of smart devices, have already initiated the deployment of the subsystems for operation in the millimetre-wave (mm-wave) spectrum. This electromagnetic (EM) range is thoroughly examined as a potential candidate for the effective exploitation of the links and access technologies for the high data rate communication systems with indoor and outdoor interconnections in the ultra-dense networks (UDNs) [1].

The large-scale antenna systems, known as massive multiple-input multiple-output (MIMO), along with the mm-wave communications are considered as the two main

physical (PHY) layer key enabling techniques and promising candidate technologies to address the requirements of the modern communications [2, 3]. These emerging platforms and systems include the fifth generation (5G) networks and the associated infrastructures and systems, such as the wireless backhaul, base station (BS), access point (AP), and user equipment (UE) units, and the high-performance UDNs.

Federal Communications Commission (FCC) and Office of Communications (Ofcom), as the governmental regulatory agencies for broadcasting and telecommunications, have approved the 28-GHz (i.e., 27–29 GHz) and 60-GHz (i.e., 57–71 GHz) bands (i.e., Fig. 1, at the end of this section) to provide the spectrum for the deployment of a number of multi-Gbps RF systems. The technologies include the 60-GHz multimedia devices using the IEEE 802.11ad, data centre connectivity with independent radio channels, wireless backhauling, and point-to-point (P2P) communications [4–6].

Therefore, as a promising way in order to boost the network capacity, the mentioned technologies based on the novel architectures and enhanced RF link planning, utilise the bandwidths with multiple GHz, and convey very high data rates to provide the high capacity with low-latency. This is also to deliver the multi-Gbps transmissions, and to meet the enormous growth demands for the exploit of large bandwidth and higher spectral efficiency. All of the essential factors are required for the deployment of the advanced future communication systems and mobile broadband [7–10].

1.2 Next-Generation Millimetre-Wave Communications

However, RF propagation with the quasi-static time-varying channel characteristics in the mm-wave bands of the EM spectrum suffers from a number of severe losses. This introduces a number of challenges for the efficient utilisation of the bands, and

further results in the link quality degradation and wireless channel impairment, due to the shorter wavelengths than the sub-6 GHz microwave systems. These path loss components mainly include the atmospheric oxygen absorption caused by the gases and precipitation, water vapour absorption, rain and foliage attenuations, blockage effects, and penetration, reflection, diffraction, and scattering losses. However, this attenuation enables the spatial frequency reuse (i.e., the number of accommodated concurrent transmissions), as well as the establishment of secure RF links through a noticeable immunity to interference between the neighbouring connections [11].

Although this can be achieved in both the line-of-sight (LoS) and non-line-of-sight (NLoS) conditions, as part of the system development framework, it necessitates the conduct of a thorough RF link budget analysis (LBA). This would improve the overall service coverage, enhance the reliable communications, confirm the feasibility of the full-duplex radio operation (i.e., the simultaneous transmission and reception), and further provide the guaranteed scalable quality of service (QoS) solutions to the UEs [12]. In view of this, the beamforming networks (BFNs), as one of the optimal system design techniques to mitigate the high propagation path loss in the mm-wave bands, are used to constructively create the narrow RF beams with significant gains, and to accommodate the directional transmission required for the antenna arrays [13, 14].

The array BFNs, as the integrated subsystems of the large-scale transceiver systems at the mm-waves, allow for the appropriate provision of a number of distinctive RF features such as maintaining the acceptable signal-to-noise ratio (SNR), providing the high precoding gains and sufficient radio signal power, and further improving the spectral efficiency (SE) and overall performance. Moreover, thanks to the small

wavelengths of the intended mm-wave frequency bands, a large number of antenna array elements can be integrated within a relatively compact dimension, at both the transmitter (Tx) and receiver (Rx) of the wireless communication transceivers. This leads to synthesising highly directional RF beams, consequently resulting in the high beamforming gains with low-interference, and realising the mm-wave subsystems based on the essential conduct of the LBA in the UDN's zone of operation [15–17].

In this regard, for the purpose of exploiting the multiplexing gains and supporting the data stream transmission, as well as controlling the phase at each element of the array, a single BFN is connected to multiple antennas. This further applies complex coefficients to fully utilise the signals to compensate for the path loss at the intended bands. In addition, this provides the phased array with the baseband signal per RF chain, in which an extra radio at each port of the MIMO system can be integrated for the microwave-digital processing. This hybrid process is conducted to perform the direction of arrival (DoA) estimation, to mitigate the co-channel interference (CCI), and to optimise the capacity using the hybrid beamforming techniques [18–20]. In order to deploy the intelligent RF communications, the BFN, as the dominant core of the multibeam antenna arrays and hybrid UDN components, is able to remarkably improve the performance of the transceivers. These BFNs realise this key objective through maintaining the consistent characteristics, improving the throughput and data rate, and accommodating the directional transmissions. Moreover, the compact and lightweight BFNs offer cost-effective solutions for the communication scenarios in which a large number of array elements are utilised to steer the direction of the main lobe of the radiation. This is conducted to compensate for the path loss, and to further realise the reliable links; i.e., currently deployed based on the costly and high

power consumption methods using the conventional MIMO systems with separate chains and digital units, along with the complex signal processing. Hence, the BFNs enable the desired distributions of the amplitude and phase coefficients to excite a corresponding number of elements for the deployment of beam steering. Thereby, facilitating a higher effective isotropic radiated power (EIRP) in the Tx mode, and an improved SNR in the Rx mode, as part of the transceiver implementation [21].

1.3 Next-Generation Flexible Devices and Systems

On the other hand, the intrinsic structural geometries of the flexible microwave and mm-wave components, devices, antennas, and systems are conformed to particular surfaces, including the cylindrical, spherical, and conical shapes. This unique feature enables compliance of the EM systems with various state-of-the-art requirements to extend both the aerodynamic and hydrodynamic properties of the platforms. This is also important for modern wireless communication systems, such as the 5G cellular networks. These flexible RF circuits and systems, with their practical characteristics and manufacturing processes, are able to expand and enhance the functionalities, in terms of the wideband operation and electronic beam steering in the UDNs [22–24].

Moreover, the flexible devices introduce the integrability with the existing installed elements of the network infrastructure, as in the BTS and backhaul architectures, in which the other structures have limitations and certain drawbacks. In addition, the flexible RF subsystems can be extensively employed as a core of the implementation requirements for the next-generation backhaul. Additionally, they can be effectively integrated with the systems where the high-capacity and reliable data transmission,

are of critical demand among the APs to efficiently maintain the RF electronic beam steering functionality based on the low-cost and lightweight RF modules [25–28].

This further implies a substantial need for employment of the BFNs to maintain the LBA requirements for both the LoS and NLoS scenarios, and to compensate for the path losses in the mm-wave channel, resulting in the overall quality enhancement of the channel and wireless transmission. Hence, the multibeam antenna arrays are fed by the BFNs as the core subsystems in the APs that perform the beam steering [29]. Hence, appropriate deployment of this architecture results in the SNR improvement, and in the CCI reduction, by pointing the directional RF beams to the desired spatial directions enforcing the nulls for the set of undesired ones, rather than broadcasting in many directions at once. Therefore, to provide the extended range and angular coverage, along with the adaptation to enable the spatial multiplexing, the feasibility of the realisation of the RF beam steering based on the flexible devices is essential. The field of microwave and mm-wave BFN circuits and systems incorporates mainly two types of feeding systems, namely the circuit-based BFNs and lens-based BFNs. Several RF beamforming techniques using a number of different architectures are reported in the literature, based on the circuit-based BFNs, such as the Butler, Blass, and Nolen matrices, as well as the lens-based and innovative RF methods [30–40].

These BFNs are employed to effectively generate multiple independent beams that are focused at different directions and to have control over the amplitude and phase at each element of the antenna array. The Rotman lens (RL), as a cost-effective and high-performance BFN with the true-time-delay (TTD) switched-beam capabilities, realises the linear phase progression, exciting consecutive radiating array elements

for the realisation of the next-generation transceiver subsystems. This investigation is of vital importance to thoroughly take into account the systematic wireless design framework for the potential flexible, conformal, and large-scale RF integration at the AP level. Hence, the RL-fed BFN architectures provide the MIMO transceiver system in the UDNs with the optimal provision of flexibility and adaptability. These systems, as the innovative solutions that require a fewer number of baseband components, are able to maintain the energy consumption, and to further sustain the reliability issues at affordable levels regarding the viable implementation cost and complexity.

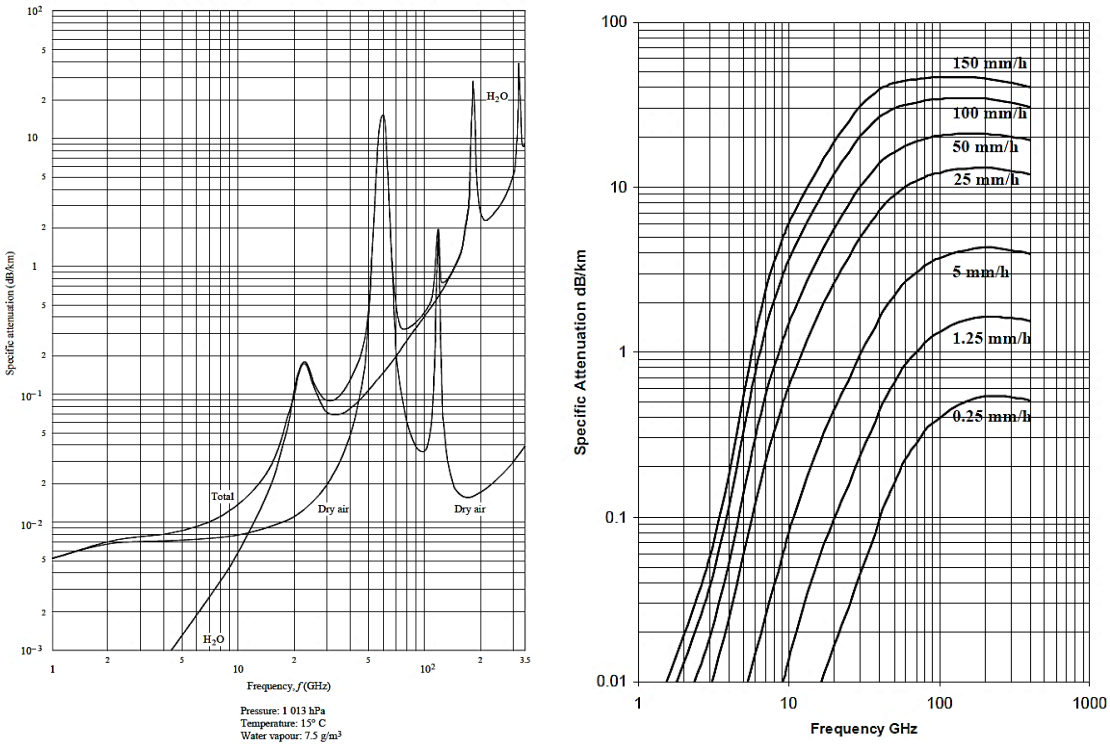

(a) (b)

Fig. 1.1. (a) Specific attenuation due to atmospheric gases, and (b) rainfall attenuation vs. frequency, for the feasibility study of the next-generation operating wireless bands [41].

1.4 Thesis Organisation

This thesis can be further divided into the following chapters:

Chapter 2 covers the comprehensive background study and literature review on the RL-based array BFNs, in order to establish a solid framework for this work.

Chapter 3 presents the proposed planar RL-based BFNs based on the employed LCP substrates, for operation in both the 28- and 60-GHz frequency bands. The chapter also covers the experimental RF beamforming based on the fabricated 28-GHz RL, as well as the conducted in-house measurements for the planar case.

Chapter 4 presents the proposed LCP-based flexible 60-GHz and conformal 28-GHz RLs based on the numerical high-resolution full-wave EM simulations. The chapter also covers the experimental RF beamforming based on the fabricated 28-GHz RL, as well as the conducted in-house measurements for the conformal case.

Chapter 5 addresses the proposed large-scale RL-based array BFNs based on the LCP substrates for a number of lens configurations, for operation in the 28-GHz band.

Chapter 6 summarises the conducted work and primary contributions, and further addresses the concluding remarks. Moreover, a number of extensions are suggested, as the potential future work, in order for the next-generation communications to be further developed based on the thoroughly presented investigations of this work.

In addition, the Appendices A and B cover the absorbing material characterisation, and the analytical modelling of the trifocal RL-based array BFNs, respectively.

Chapter 2:

Background Study and Review of Multibeam Antennas and RF/Microwave Array Beamforming Networks for Wireless Communication Systems

2.1 Introduction

Generating multiple radio beams using an antenna array system, along with having wide bandwidth and beam steering capability, are of crucial importance for the next-generation wireless communications [11]. For this purpose, various array BFNs are introduced, in order to have control over the amplitude and phase at each element of the antenna array [14]. Microwave and mm-wave passive circuit-based or lens-based networks form an important class of these multibeam networks. Two well-known examples of such circuit-based BFNs are Blass matrix and Butler matrix [30]. In this chapter, the arrays and multibeam antennas are discussed and are followed by the analysis of the RL-BFNs, in order to develop a well-established framework for the design of the subsystems based on the microwave and mm-wave techniques.

2.2 Principles of Antenna Arrays

An antenna array is an entity consisting of two or more element antennas. Antenna array systems may exhibit many useful properties, which cannot be achieved with a single element, such as high gain, narrow beam, and scanning or adaptive beam. Fig. 1 presents an antenna array that consists of two elements having a separation of *d*.

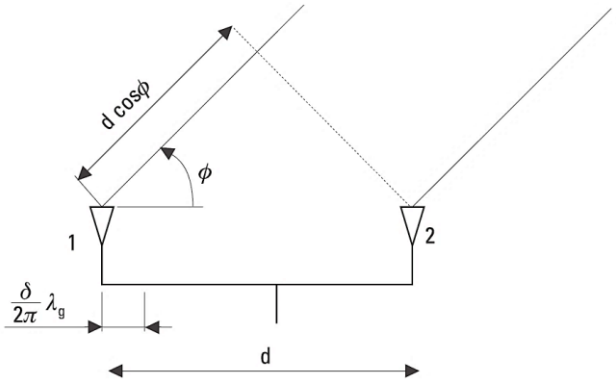

Fig. 2.1. An antenna array consisting of two elements [42].

It is assumed that the far-field EM patterns of the antennas are $E_1(\phi)$ and $E_2(\phi)$ (i.e., the normalised electric field intensity in volts per meter as a function of direction), and that the phase difference of the feed currents is δ (i.e., in this case, the lengths of the feed lines are different). The total field produced by the array is given as (1) [42]:

$$\stackrel{\text{def}}{=} E(\phi) = E_1 e^{-j(kd\cos\phi+\delta)} + E_2(\phi). \quad (2.1)$$

The path length difference of $d\cos(\phi)$ in free space produces the phase difference of $kd\cos(\phi)$. The fields of the array elements are in the same phase in directions ϕ_{max}, and have opposite phases in directions ϕ_{min}, which meet the following conditions of (2) and (3), respectively; where *n* is an integer.

$$kd\cos(\phi_{max}) + \delta = 2n\pi; \quad (2.2)$$

$$kd\cos(\phi_{min}) + \delta = 2n\pi + \pi. \quad (2.3)$$

Furthermore, if the elements of the antenna array are similar, i.e., E_1 (ϕ) = E_2 (ϕ), and they are fed in phase, i.e., δ = 0, equation (1) can then be written as (4):

$$\xrightarrow{yields} E(\phi) = E_1(\phi)\left(1 + e^{-jkd\,cos\phi}\right). \tag{2.4}$$

Furthermore, the array factor (AF) is a function of the geometry of the array element and the excitation phase, in which its EM characteristics can be controlled by varying the separation and phase between the elements. It quantifies the effect of combining the radiating array elements without the radiation pattern taken into account. The AF is defined based on the number of elements, their geometrical arrangement, their relative magnitudes and phases, and their array element spacings [43].

Therefore, the antenna array pattern can be defined as the product of the pattern of the array element, and the AF. The antenna array may be linear, planar, or conformal (i.e., shaped according to the bearing surface). Moreover, different patterns can be realised for the array using different types of elements such as microstrip, stripline, dipoles, horns, and slots [44]. An array incorporating the identical elements with the same magnitude and each with a progressive phase is considered as a uniform array. Hence, the generalised AF of an *N*-element array is given by equations (5) and (6):

$$\stackrel{\text{def}}{=} \text{AF} = a_1 e^{j(kd\,cos\phi + \delta_1)} + a_2 e^{j2(kd\,cos\phi + \delta_2)} + \cdots + a_N e^{j(N-1)(kd\,cos\phi + \delta_N)}; \tag{2.5}$$

$$\xrightarrow{yields} \text{AF} = \sum_{n=1}^{N} a_n\, e^{j(n-1)(kd\,cos\phi + \delta_n)}. \tag{2.6}$$

where ϕ is the beam angle, d is the displacement of the elements, δ is the difference in phase excitation between the elements, and a_n's are the excitation coefficients.

Furthermore, the normalised pattern of the discussed two-element antenna array may look like that depicted in Fig. 2, in which the pattern of the array (i.e., solid line)

equals the pattern of the element multiplied by the AF. Moreover, an antenna array is referred to as a broadside array when it has a maximum radiation in the direction perpendicular to the axis of the array (i.e., when ϕ = 90˚). An array is also referred to as an end-fire array when it has a maximum radiation in the direction along the axis of the array (i.e., when ϕ = 0˚ or ϕ = 180˚). The direction of the radiation for the main beam depends on the phase difference between the array elements. Therefore, it is possible to continuously steer the main beam in any direction by appropriately varying the progressive phase between the elements; the type of array that the beam is steered to the desired direction is referred to as a phased array antenna [44].

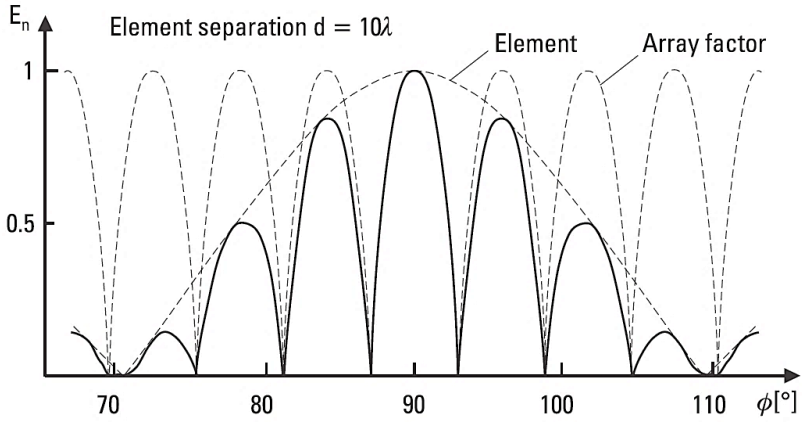

Fig. 2.2. Radiation pattern of the two-element antenna array [42].

If there are electronically controlled phase shifters in the feeding an antenna array, the direction of the main beam can be changed rapidly without rotating the antenna. This kind of electronic beam scanning is much faster than conventional mechanical scanning. A phased array antenna combined with digital signal processing (DSP)-based algorithms may operate as a smart adaptive antenna, in which the radiation pattern changes according to the radiowave propagation environment. This would offer impressive performance properties in terms of the signal quality, interference- and noise-suppression capabilities, and network information capacity.

The hybrid RF-digital network combines multiple elements with DSP to optimise the EM radiation pattern, in response to the signal environment in the imperfect radio channels encountering multipath, interference, and fading. This network forms the radio beams in different orientations based on the BFNs for the intelligent mobile sensing, and for the robustness improvement of the wireless communications.

Moreover, RF beam steering is required in the microwave and mm-wave systems to provide the hybrid versatility and high-resolution, with more symmetrical patterns and lower SLLs, along with providing the estimation of channel parameters and the DoA in wireless communications. In these multibeam systems, the independence of the array elements is crucial to the performance of the associated DSP algorithms, in which the powerful and enhanced DSP methods; e.g., multiple signal classification (MUSIC); are employed for the implementation of the smart adaptive systems.

These robust algorithms, integrated in a high-performance BFN architecture, would compensate for the errors and imperfections of the system components. The mutual coupling effects (i.e., surface currents on the surrounding elements generated from the EM field radiation, due to the induction of a current when an element is excited) between the elements would degrade this independence. The decoupled terminal voltages would be then applied to the algorithm to estimate the DOA in a multibeam system and to enhance the channel capacity and throughput without expanding the spectral bandwidth. This is to maintain the reliability of the RF propagation channel between the Tx and Rx, based on the directional transmissions using the BFNs, in order to retain the inherent dependence among the cell density, spectral efficiency, and bandwidth. In this regard, the following section covers the discussion and RF

analysis of the multibeam antennas and lens-based BFNs, as the central and primary core of the high-performance next-generation wireless communication subsystems.

The EM far-field corresponds to the distances where the spherical wavefronts can be approximated to the planar ones, which is restricted to the RF radiating aperture. Moreover, the EM near-field can be further categorised into two regions, namely the reactive near-field and radiating one. The far-field and near-field distances can be defined as (7), where *d* is the antenna's maximum dimension and λ is the wavelength of the radiation. Furthermore, the radiation pattern is a graphical representation of the EM-based properties, such as the radiation intensity, polarisation of an antenna with respect to the spatial coordinates, and strength of the electric field. In addition, the ability of the antenna to focus the power in an intended direction is measured by its directivity that results in the gain, when it is multiplied by the efficiency. The latter also considers the losses at the input terminal of the antenna that is fed by the intended BFN subsystem, as well as the reflection, conduction, and dielectric losses.

$$\xrightarrow{yields} r_N \leq \frac{2 \times d^2}{\lambda} \leq r_F. \tag{2.7}$$

2.3 Multibeam Antennas and RF Beamforming Techniques

A multibeam antenna is the one with a capability to form a number of RF beams in different directions from the same aperture [42]. It includes separate well-isolated ports with the simultaneous independent operations, to be connected to a separate Tx/Rx through a multiple-way switch resulting in a sequentially scanning antenna. The field of RF and microwave beamforming encompasses two major areas, namely

the quasi-optical-based techniques and circuit-based ones. The quasi-optical types involve a hybrid arrangement of either a reflector or lens with a feeding array [45].

Moreover, the illumination of the radiating array elements is accomplished via the optically distributing the source RF signals through the space. In this regard, both surfaces of the lens require matching, in order to optimise the output performance and to provide an efficient aperture illumination with the lower spillover loss. The latter can be defined as the coupling of EM energy from the input beam ports to the output array ports due to the sidewall reflections within the lens and vice versa [45].

Fig. 3 depicts the generalised concept of the lens-fed feeding networks, including the principles of the Ruze and Rotman lenses, which have evolved over the years [45]. The lens contains the metal plates capable of constraining the rays to travel parallel to the axis, i.e., the electrical path length P–Q. Using the ray tracing method through points P, Q, and the origin, two equations result that interrelate the lens thickness and refractive index and that specifies the inner contour to be circular assuming that only F_1 and F_2 are focal points. This would result in the appropriate control of the RF amplitude, phase deviations, and multiple reflections within the lens. In addition, if RF lens interconnections are no longer parallel to the axis, but a connection P–Q' is specified, a Rotman-type lens-based array feeding network is formed. Moreover, the refractive index is controlled by the electrical path length P–Q'. This would allow a third focal point to exist on the axis, which would reduce the deviation, and would allow the inputs and outputs to be displaced to optimise the lens performance [46].

Furthermore, when a feeding point is placed at any one of the lens focal points, the corresponding wavefront has no phase error (i.e., the deviation in the electrical path

length from that providing a plane phase-front for a general point) [46]. Moreover, when the feeding is displaced from these focal points, the corresponding wavefront would have a phase error. However, for the wide-angle beam scanning, the lens must be focused at all intermediate points along the circular focal arc. It should be noted that the phase error is a function of the lens aperture and scan angle.

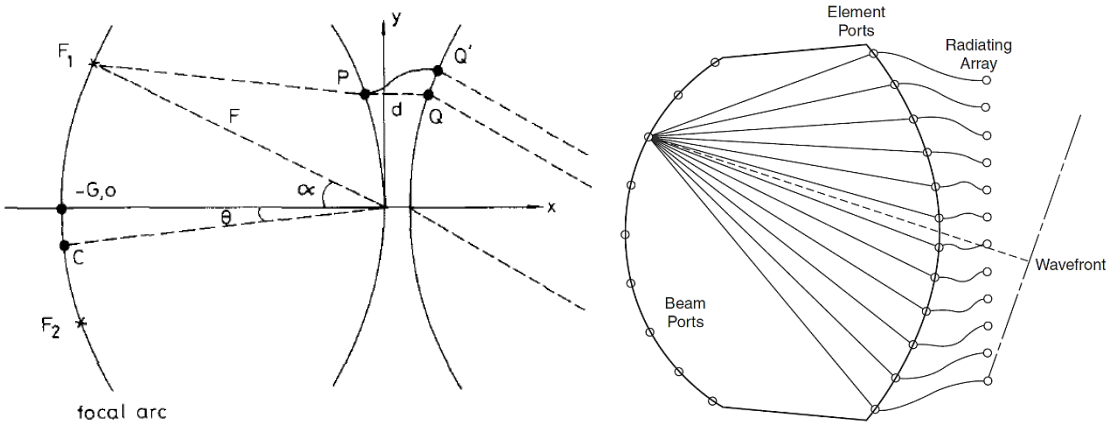

(a) (b)

Fig. 2.3. Geometry of the constrained lens-based BFNs: (a) P–Q specifies the Ruze lens BFN, and P–Q' specifies the Rotman lens BFN; (b) configuration of the RL-BFN [45].

The Rotman lens-based BFN enables multibeam phased array systems to generate scanning beams for the reliable RF beam steering applications. This switched-beam passive network is properly designed in order to provide the array with the correct phase and acceptable amplitude distributions across the RL aperture [47]. The low-profile BFN is capable of focusing the energy into a geometrically-configured cavity, in order to appropriately produce a wavefront across the output that is phased by the time-delay in the signal transmission, and to scan a beam in the desired pattern that radiates a circular phase-front within the lens cavity [46–48].

The theoretical lens formulations have been modified and improved over the years, based on the rigorous equations derived from the geometrical optics (GO) [48]. The design of the trifocal lens-based BFN with the homogeneous medium is controlled by a series of equations that set the RL focal points, array positions, and lengths of transmission lines (TLs) to provide the antenna array with the beam patterns that can be steered in certain directions, along with suppressing the undesired ones [49]. The RL design and synthesis procedure ensure the parameters to be tuned, in order to optimise the overall performance of the RF lens device, in terms of the phase and amplitude errors, reflection and transmission coefficients, and SLLs [49, 50].

Fig. 4 shows a schematic diagram of a trifocal RL-BFN with input (i.e., beam contour) and output (i.e., array contour) ports lie on either side of the RL cavity (i.e., an etched thin copper layer on the RF dielectric substrate). It incorporates three theoretically perfect focal points (i.e., no phase errors), namely F_1, F_2, and F_0, in which the latter is located on the central lens axis (i.e., on-axis focal point), while the other two are symmetrically located on the circular focal arc at $\pm\alpha$ (i.e., off-axis focal points). For all the other points of the lens device, the phase errors occur, since the path length will not be a linear function of the input beam position. At the wavefront, all the EM rays must be in phase independent of the path they travel [49–51].

The coordinates of the two off-axis focal points F_1 and F_2 and one on-axis focal point F_0 are $(-F\cos(\alpha), F\sin(\alpha))$, $(-F\cos(\alpha), -F\sin(\alpha))$, and $(-G, 0)$, respectively [52]. TL_0 and TL are the microstrip TLs, with lengths denoted by W_0 and W, respectively; θ is defined as the radiation angle corresponding to the RF lens focal points. The relative permittivity factors for the cavity and EM radiation environment are given as ε_r and

ε_i, respectively. The TLs, with the effective dielectric constant of ε_e, are routed with the appropriate curvature in order to guarantee the separation and non-overlapping required for the lens array contour, and also to maintain the same electrical length among all the output meandered TLs. In the generalised RL model, it is assumed that the focal angle α is equal to the scan angle θ, and although the angles can be different, by applying which, it can be used for the potential computations and optimisations regarding the compactness of the beam region and phase error reductions [52–54].

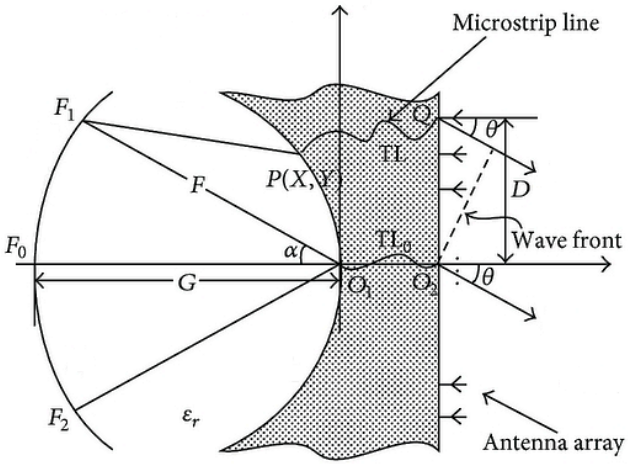

Fig. 2.4. Configuration and design parameters of the trifocal RL-BFN [51].

The equations (8)–(10) govern the design of the trifocal RL-BFN based on the GO, in order to maintain the performance of the device, in terms of generating multiple RF beams with a linear progressive phase shift across the array ports. This is due to the different electrical lengths between a specific input port and all the output ports, as well as preventing the array from changing the scanning direction with frequency variation (i.e., the wideband TTD operation of the lens). Hence, the TTD-based BFN provides the linear phase progression over the array ports based on maintaining a constant time-delay over a wide frequency range of operation. In addition, the lens

shape also determines the mutual coupling between the ports, multiple scattering, and spillover losses. As the value of α increases, the output array contour closes (i.e., the lens curvature increases), and the feeding contour opens [52–55].

In the design procedure, the main governing equations impose the condition of path equality based on the ray tracing model to derive the lens geometry. The equations also address methods of explicitly solving for the geometry of the receiver contour, i.e., $P(X, Y)$. The latter is defined by the position of the three focal points, as well as the width of the output array contour (i.e., $2D$); and W, as the primary parameters that enable the array to scan into a certain known direction (i.e., Appendix B).

$$(\overrightarrow{F_1P})\sqrt{\varepsilon_r} + W\sqrt{\varepsilon_e} + D\sqrt{\varepsilon_i}\sin(\theta) = F\sqrt{\varepsilon_r} + W_0\sqrt{\varepsilon_e}; \tag{2.8}$$

$$(\overrightarrow{F_2P})\sqrt{\varepsilon_r} + W\sqrt{\varepsilon_e} - D\sqrt{\varepsilon_i}\sin(\theta) = F\sqrt{\varepsilon_r} + W_0\sqrt{\varepsilon_e}; \tag{2.9}$$

$$(\overrightarrow{F_0P})\sqrt{\varepsilon_r} + W\sqrt{\varepsilon_e} = G\sqrt{\varepsilon_r} + W_0\sqrt{\varepsilon_e}. \tag{2.10}$$

A number of RL-based BFNs operating at the mm-wave frequency bands, based on the different topologies, are reported in the literature [56]. They are introduced for a diverse set of antenna and microwave applications, and are realised using different technologies, such as microstrip [57, 58], low-temperature co-fired ceramic (LTCC) [59], silicon [60], system-on-package [61, 62], substrate integrated waveguide [63], and surface micromachining [64]. This work has been carried out as an attempt to develop a number of low-profile flexible and conformal array beamformers, for the employment as the mm-wave subsystems in the next-generation communications.

2.4 Summary

The move to the mm-wave communications is potentially one of the biggest changes that would be seen in consumer electronics, in the next decade. The drive for higher data rates, wider bandwidth, and more capacity would increase, requiring extensive development to the existing RF and microwave technologies. Each component in the network infrastructure must be improved to keep pace with the network demands. The focus here has been on enhancements to mm-wave subsystems and large-scale beamforming devices that would eventually be critical to meeting the requirements of next-generation wireless communication networks. Therefore, in this regard, this chapter has thoroughly discussed the important principles and essential concepts of the multibeam antenna systems and array beamforming techniques. The primary objective of this background study has been to build up an informative overview on the lens-based antenna beamformers, which can also be effectively served as a fundamental platform for the optimal RF design and performance evaluation of the RL-BFNs in the subsequent chapters of this research work.

Chapter 3:

Numerical and Experimental Evaluation of Planar 28-GHz and 60-GHz Rotman Lens-Based BFNs for Next-Generation Wireless Communication Subsystems

3.1 Introduction

In the development of the flexible and conformable high-performance devices and components, substrate materials are crucial to the deployment of the low-cost and power-efficient systems [65–68]. In this regard, the Rogers ULTRALAM 3850 liquid-crystal polymer (LCP) laminates exhibit significant combination of the electrical, thermal, chemical, and mechanical properties, for the enhanced implementation of the high-speed devices and systems at the higher temperatures (i.e., the permeation of gases through the dielectric material is not affected by the humidity) [69–72].

The substrate has low moisture absorption and can withstand chemical exposure, as well as temperature variations and exhibits the dielectric constants of 2.9–3.1 and loss tangent less than 0.005, throughout the whole frequency range up to 110-GHz

[73]. Therefore, these unique features make the LCP substrate very appealing as one of the primary enabling technologies for the RF development of the next-generation multi-environmental wireless communication applications and infrastructures [74].

3.2 Planar Design and Evaluation: The 28-GHz 5×8 RL-BFN

The design equations provide the method for thoroughly designing the mm-wave lens-based BFN shown in Fig. 1, in order to operate in the 18–38 GHz band, with the switched-beam scanning coverage of ±30°. The RL is developed based on the Rogers ULTRALAM LCP flexible laminate with the dielectric constant of ε_r = 2.9, loss tangent of tanδ = 0.0025, substrate thickness of h = 0.18 mm, and top- and bottom-cladding of t = 17.5 μm. The port-pointing feature is effectively enabled in the design, as well. Therefore, the beam and array ports are adjusted so that the boresight of each taper points to the centre of the opposite contour, rather than being normal to the surface, in order to enhance the overall RF performance of the proposed lens-based BFN.

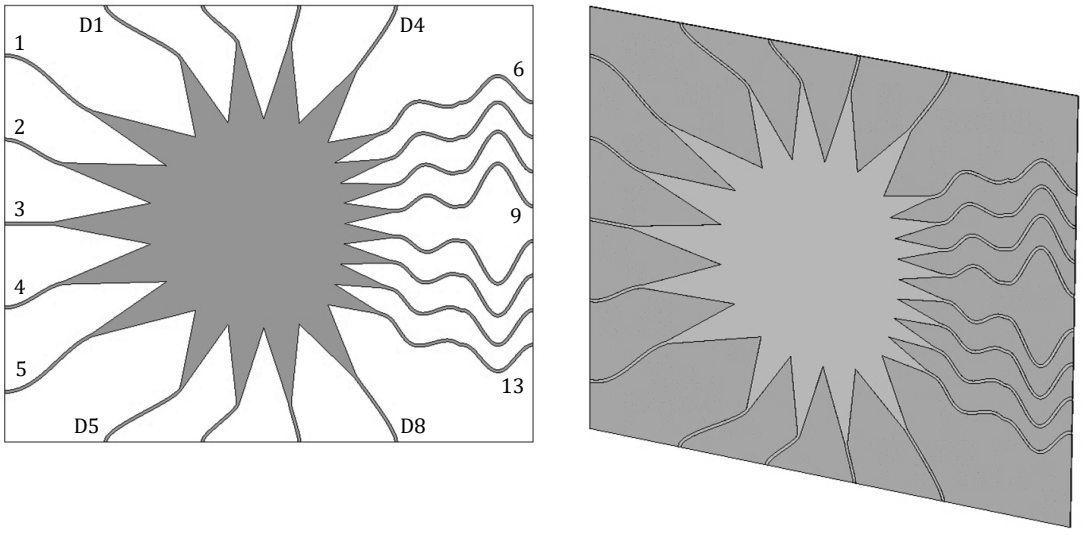

(a) (b)

Fig. 3.1. LCP-based 28-GHz BFN: (a) wideband RL with 5 input beam ports (i.e., 1 to 5), 8 output array ports (i.e., 6 to 13), and 8 absorbing dummy ports (i.e., D1 to D8), with the dimensions of 67.45 × 81.87 mm^2, front view; (b) perspective view; the TLs connected to the output ports are meandered to maintain an identical electrical length among the array elements. Also, the order of enumerating the ports are uniform in the subsequent lenses.

The high-performance computing (HPC)-based full-wave and very high-resolution EM simulations have been conducted, based on the finite integration technique (FIT) using the robust transient solver (i.e., CST STUDIO SUITE software), to rigorously evaluate the time-domain characteristics of the electrically-large RL. The FIT is the discretisation of the integral form of Maxwell's equations [75–77]. Fig. 2 depicts the characteristics of the dummy ports as an integral part of the BFN, over the mm-wave frequency range of operation, which are all terminated with the 50-Ω matched loads. Furthermore, the sidewall contours along with the dummy ports, are appropriately designed and implemented to minimise the EM reflections and standing waves from the sidewalls. This consequently results in the improved performance of the lens, in terms of the RF device efficiency, as also defined in [78]. Fig. 2 presents the primary contribution levels of the match-terminated dummy ports, denoted by the elements 1 to 8, for the excited input beam ports one and three, corresponding to exertions of the minimum and maximum RF device efficiencies, respectively. In this case, dummy port 1 is located adjacent to input beam port one, and progressively, dummy port 8 is located adjacent to output array port thirteen. Also, the graphical representations of the surface currents in the subsequent sections primarily depict the impact of the dummy ports on the overall EM-centric behaviour of the developed RL-BFNs.

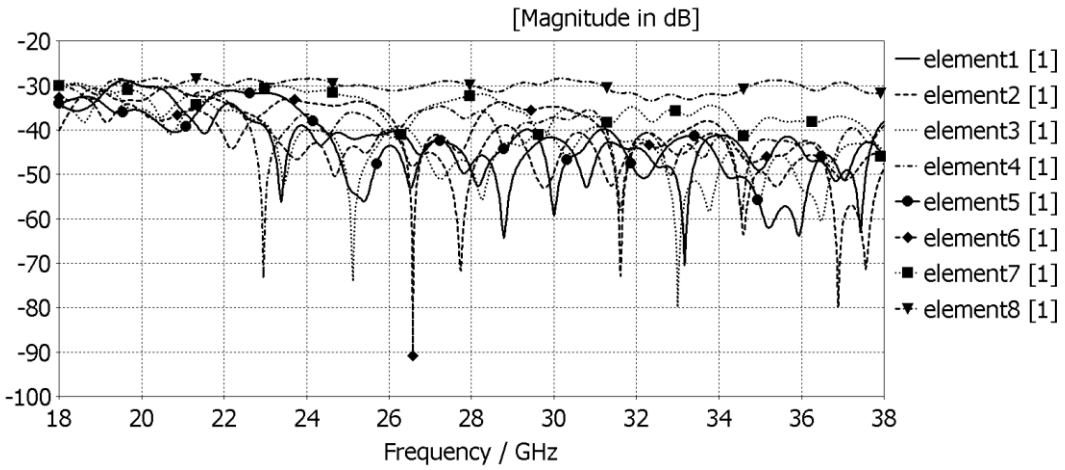

(a)

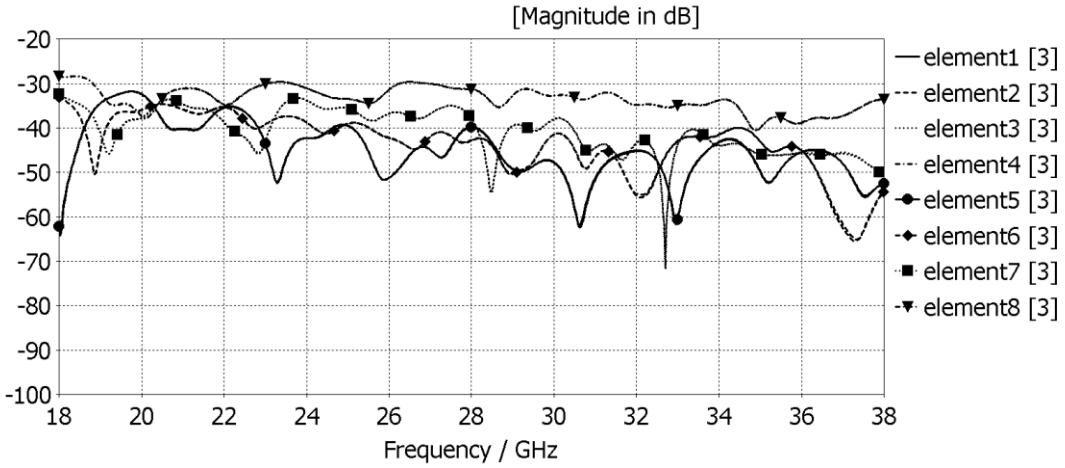

(b)

Fig. 3.2. Current plots of the absorbing dummy ports (i.e., element 1: D1 to element 8: D8) of the developed LCP-based wideband 5 × 8 RL-BFN: (a) magnitude plots for input beam port 1 active; (b) magnitude plots for central input beam port 3 active. It should be noted that the element term in the figures refers only to these absorbing dummy ports.

Figs. 3 (a) to (e) present the transmission coefficients of the proposed lens for the excited ports one to five, respectively. As the scattering (*S*)-parameters depict, the RL exhibits the desired wideband characteristics across the whole frequency range,

and further maintains an almost uniform power distribution through the RL cavity, based on the behavioural conformity according to the generalised trifocal RL theory. The isolation characteristics among the beam ports have been analysed to confirm the significant operation of the RF lens, in terms of providing the required isolations among the input beam ports to retain the performance of the BFN for the efficient operation in the whole frequency range. It should also be noted that the overall EM distribution behaviour of input beam ports one and two are theoretically identical to the output characteristics of input beam ports five and four, respectively, due to the intrinsic symmetrical structure of the developed RL-BFN. Moreover, the device efficiency at the centre frequency of 28-GHz is numerically computed as 45.1%. In addition, Fig. 3 (f) depicts the reflection coefficient plots for the activated beam ports one to five, which also confirms the wideband maintenance of the RF transmission.

Furthermore, Figs. 4 (a) to (e) thoroughly present the output phase characteristics of the developed LCP-based BFN across the entire operating RF band of 18–38 GHz, when input beam ports one to five are appropriately fed, respectively. It can also be noticed that the developed mm-wave lens device exhibits outstanding performance for the effective realisation of the electronic beam steering, in terms of the constant phase difference, as a function of frequency, as well as the linear progressive phase distributions among the output array ports of the BFN. This feature can be exploited further, in order for the lens to be integrated with the RF peripherals, incorporating the active and passive components and elements at the transceiver level. This would then result in the implementation of a fully integrated phased array module.

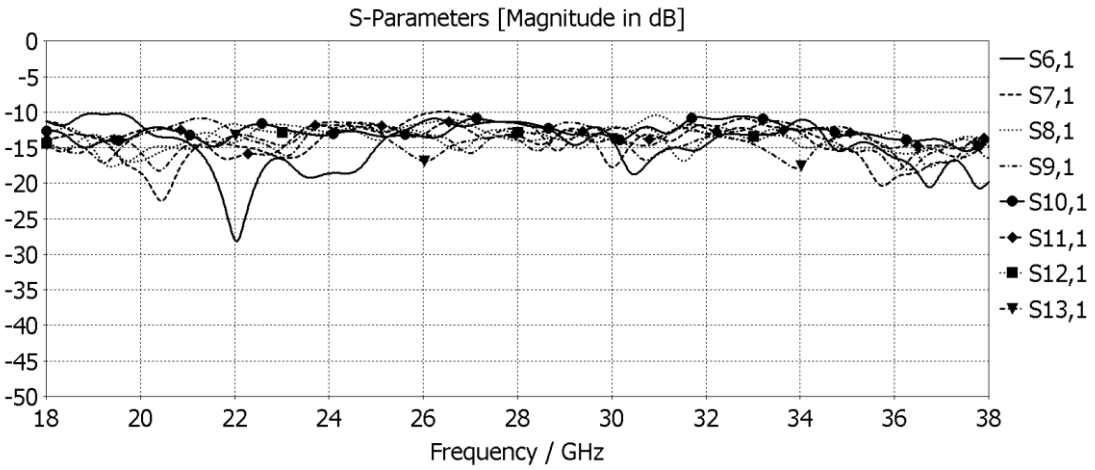
S-Parameters [Magnitude in dB]
0
-5
-10
-15
-20
-25
-30
-35
-40
-45
-50
18
20
22
24
26
28
30
32
34
36
38
Frequency / GHz
S6,1
S7,1
S8,1
S9,1
S10,1
S11,1
S12,1
S13,1

(a)

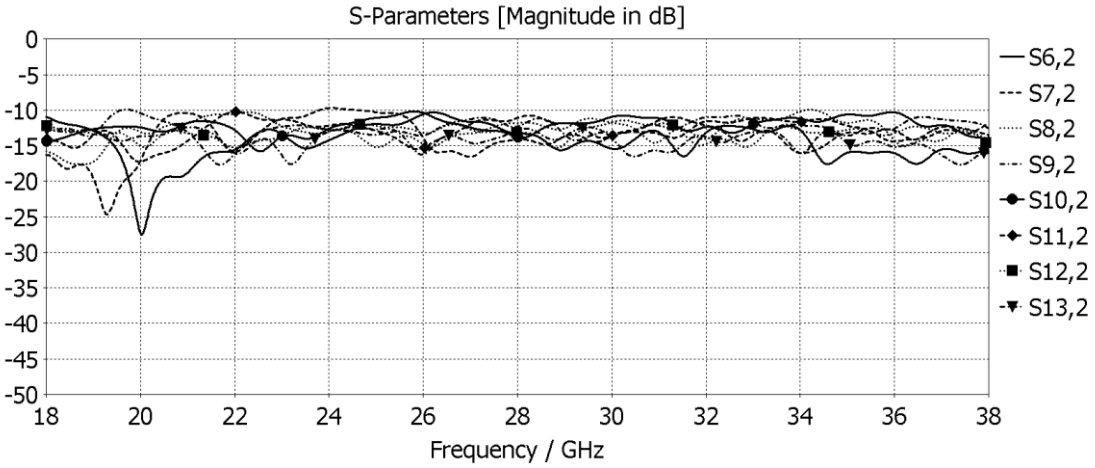
S-Parameters [Magnitude in dB]
0
-5
-10
-15
-20
-25
-30
-35
-40
-45
-50
18
20
22
24
26
28
30
32
34
36
38
Frequency / GHz
S6,2
S7,2
S8,2
S9,2
S10,2
S11,2
S12,2
S13,2

(b)

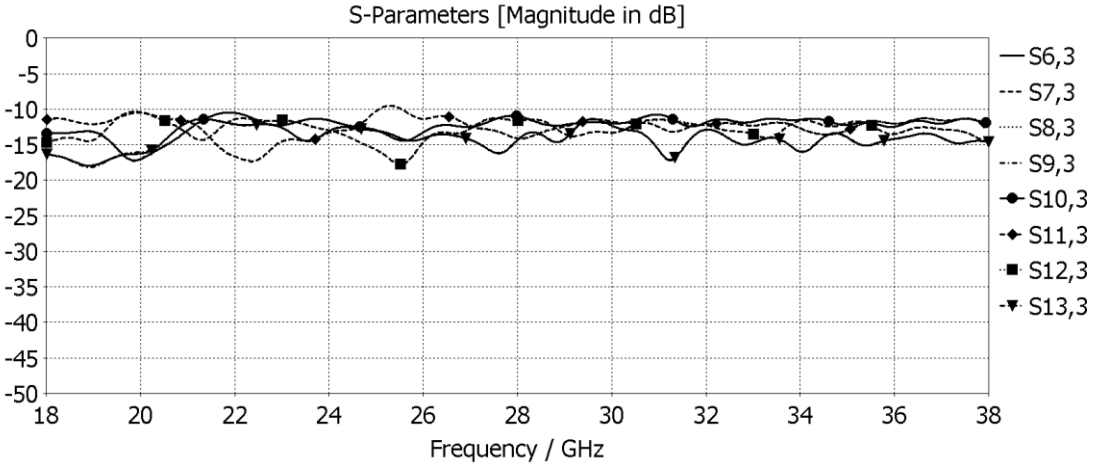
S-Parameters [Magnitude in dB]
0
-5
-10
-15
-20
-25
-30
-35
-40
-45
-50
18
20
22
24
26
28
30
32
34
36
38
Frequency / GHz
S6,3
S7,3
S8,3
S9,3
S10,3
S11,3
S12,3
S13,3

(c)

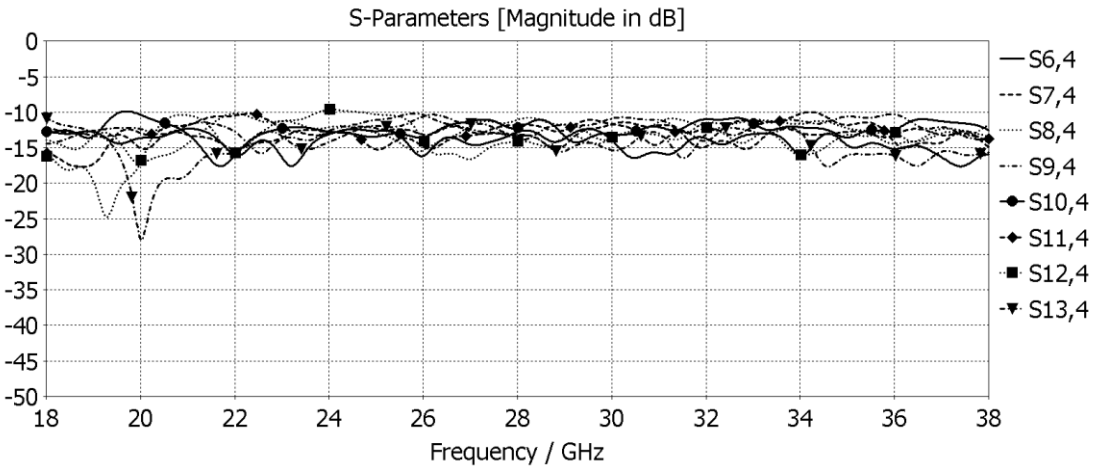
S-Parameters [Magnitude in dB]
0
-5
-10
-15
-20
-25
-30
-35
-40
-45
-50
18
20
22
24
26
28
30
32
34
36
38
Frequency / GHz
S6,4
S7,4
S8,4
S9,4
S10,4
S11,4
S12,4
S13,4

(d)

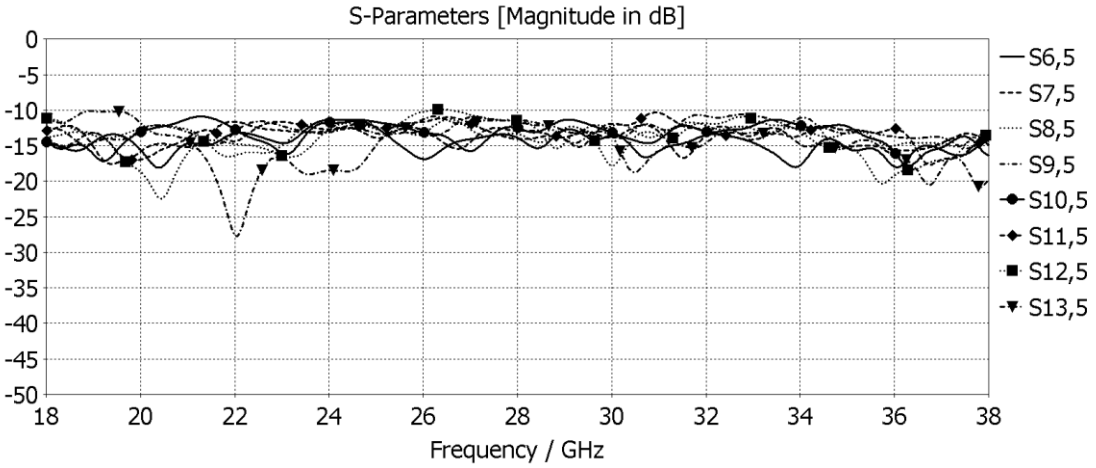
S-Parameters [Magnitude in dB]
0
-5
-10
-15
-20
-25
-30
-35
-40
-45
-50
18
20
22
24
26
28
30
32
34
36
38
Frequency / GHz
S6,5
S7,5
S8,5
S9,5
S10,5
S11,5
S12,5
S13,5

(e)

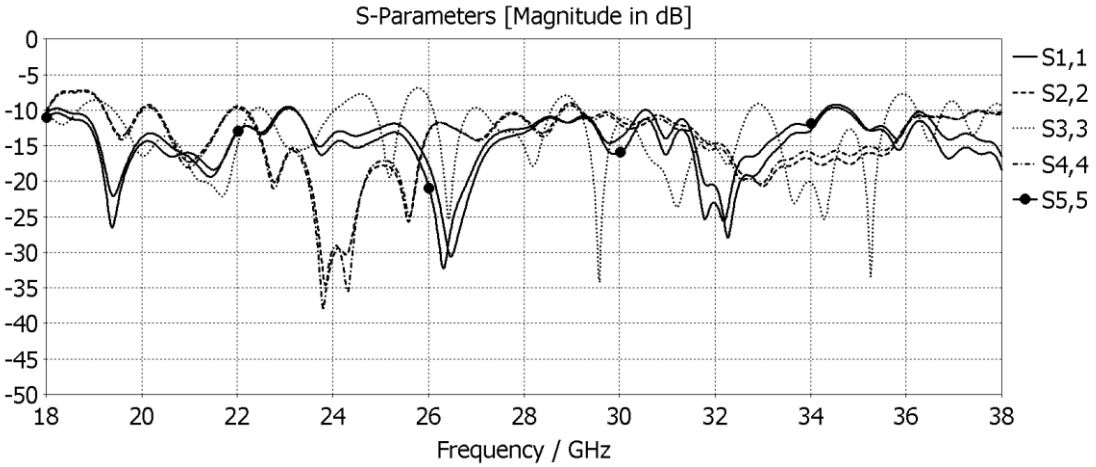
S-Parameters [Magnitude in dB]
0
-5
-10
-15
-20
-25
-30
-35
-40
-45
-50
18
20
22
24
26
28
30
32
34
36
38
Frequency / GHz
S1,1
S2,2
S3,3
S4,4
S5,5

(f)

Fig. 3.3. Simulated *S*-parameters and output characteristics of the developed planar LCP-based RL for the wideband operation: (a) transmission coefficient plots for input beam port 1 active; (b) transmission coefficient plots for beam port 2 active; (c) transmission coefficient plots for central input beam port 3 active; (d) transmission coefficient plots for input beam port 4 active; (e) transmission coefficient plots for beam port 5 active; (f) reflection coefficient plots for the excited input beam ports 1 to 5 of the lens device.

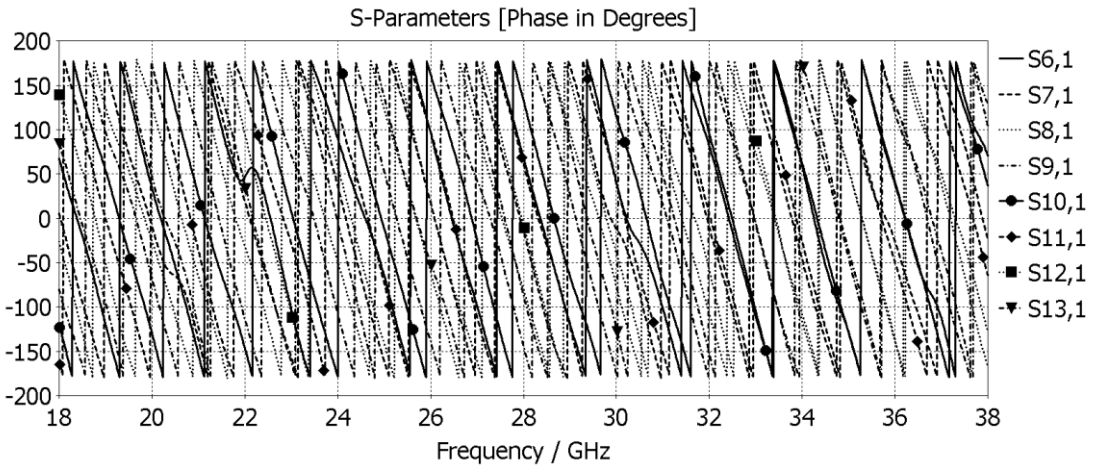

(a)

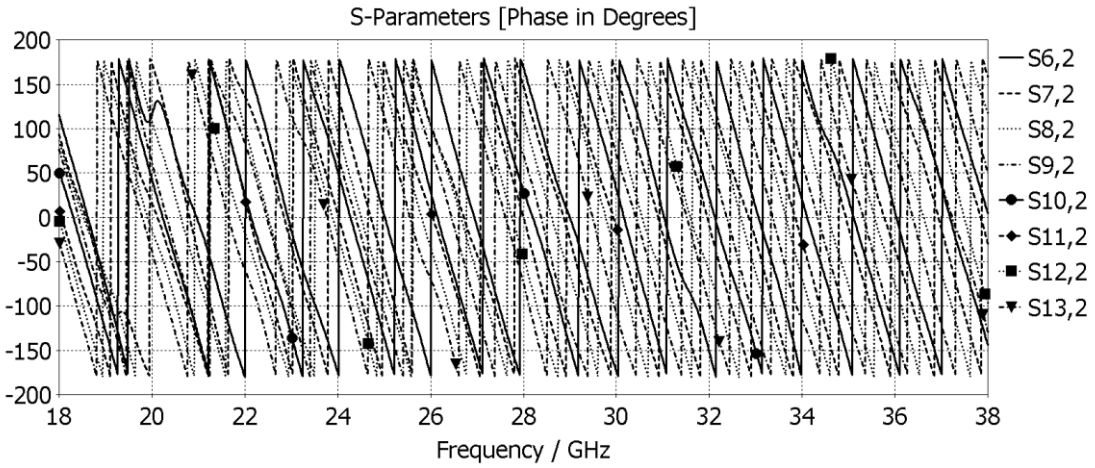

(b)

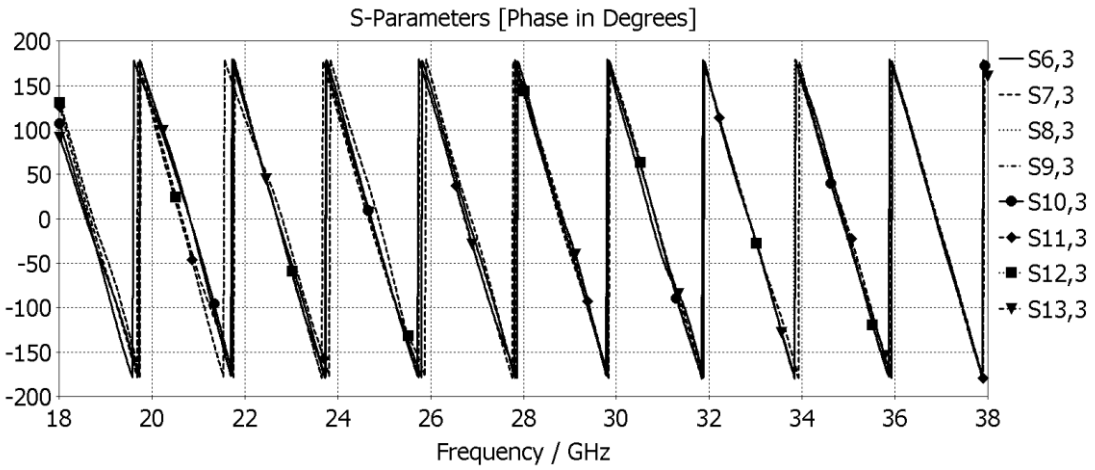
S-Parameters [Phase in Degrees]
200
150
100
50
0
-50
-100
-150
-200
18
20
22
24
26
28
30
32
34
36
38
Frequency / GHz
S6,3
S7,3
S8,3
S9,3
S10,3
S11,3
S12,3
S13,3

(c)

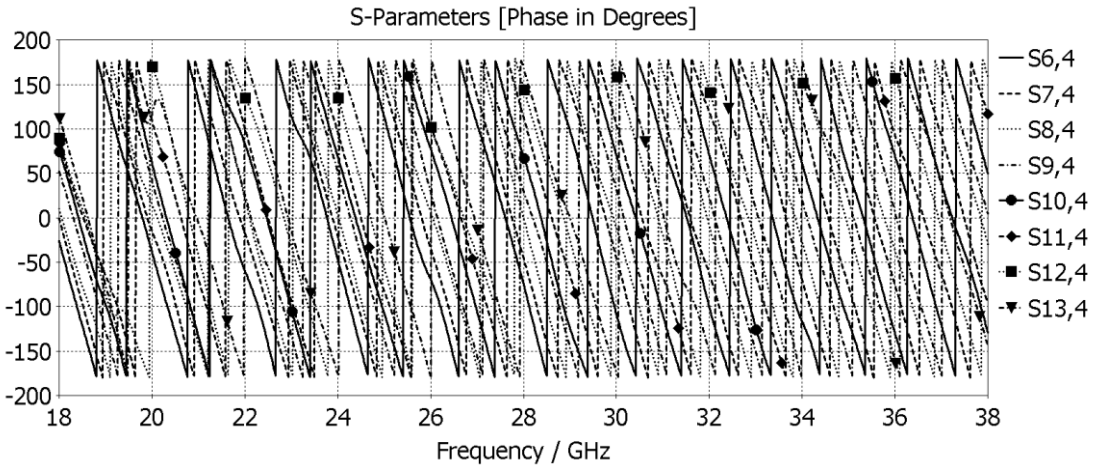
S-Parameters [Phase in Degrees]
200
150
100
50
0
-50
-100
-150
-200
18
20
22
24
26
28
30
32
34
36
38
Frequency / GHz
S6,4
S7,4
S8,4
S9,4
S10,4
S11,4
S12,4
S13,4

(d)

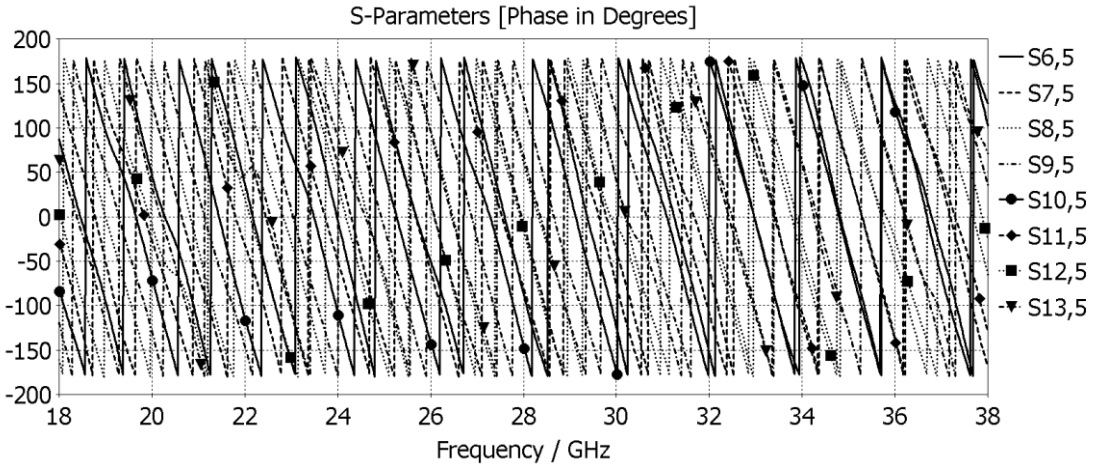
S-Parameters [Phase in Degrees]
200
150
100
50
0
-50
-100
-150
-200
18
20
22
24
26
28
30
32
34
36
38
Frequency / GHz
S6,5
S7,5
S8,5
S9,5
S10,5
S11,5
S12,5
S13,5

(e)

Fig. 3.4. Simulated *S*-parameters and output characteristics of the developed planar LCP-based RL for the wideband operation: (a) linear progressive phase distributions for beam port 1 active; (b) linear progressive phase distributions for beam port 2 active; (c) linear progressive phase distributions for beam port 3 active; (d) linear progressive phase distributions for beam port 4 active; (e) linear progressive phase distributions for beam port 5 active. The tuned value of the focal ratio is set to 1.085 to minimise the phase error.

The maximum EM power is delivered to the output array ports of the lens device, and the progressive low-ripple amplitude, as well as the phase distributions, further confirm the high-performance operation of the developed mm-wave lens. Moreover, the RL-BFN conducts the distribution of the energy across the array ports, therefore resulting in the provision of the electronic beam scanning to be effectively deployed for the advanced next-generation wireless communication subsystems.

Figs. 5 (a) to (e) present the computed surface current distributions of the RL when input beam ports one to five are fed, respectively. The results depict the progressive distributions of the energy across the output array ports, as well as the intensities of the power throughout the device. Fig. 5 (f) indicates the lens with the deployed range, i.e., the same scale for the other developed configurations. The generation of the beams in different orientations results in the provision of the hybrid versatility and robustness in the Gbps mm-wave communications along with the optimised and symmetrical radiation patterns, in response to the propagation environment in the imperfect RF channels encountering the multipath, interference, and fading, for the efficient deployment of the integrated RF and wireless electronic submodules.

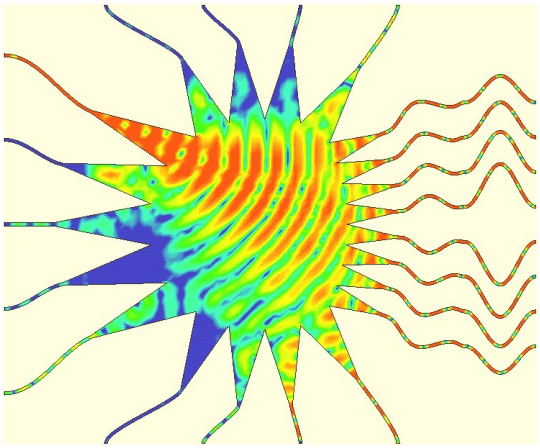

(a)

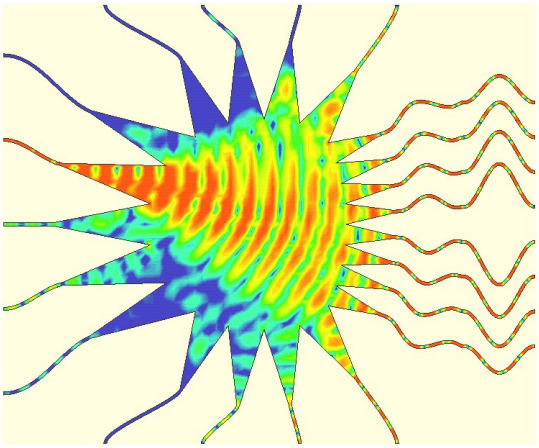

(b)

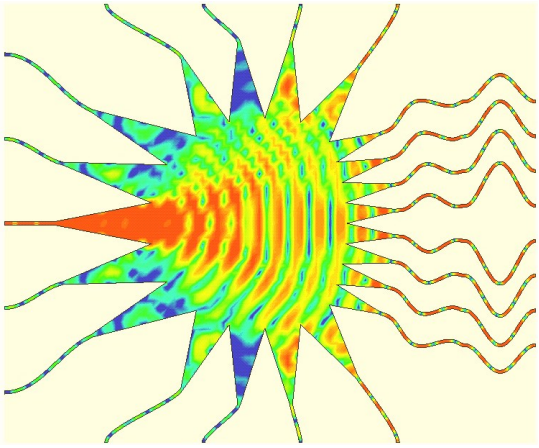

(c)

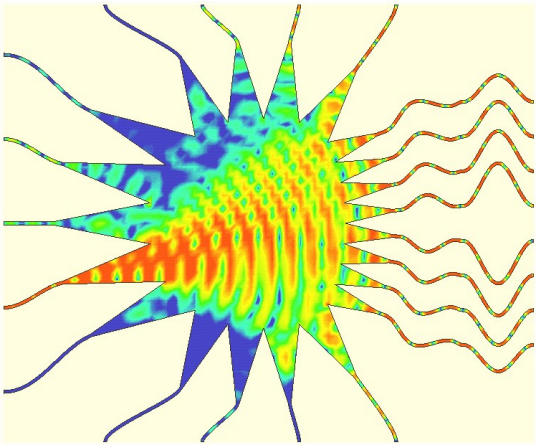

(d)

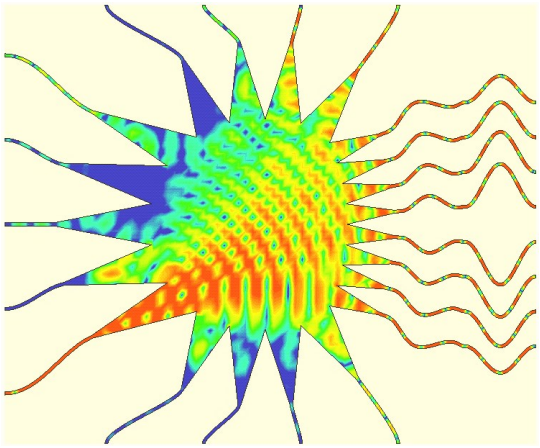

(e)

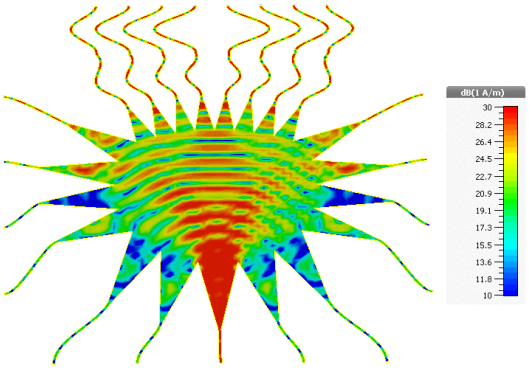

(f)

Fig. 3.5. Surface current distributions of the developed LCP-based wideband RL-BFN for the excited input beam ports at mm-wave centre frequency f = 28-GHz: (a) input beam port 1 active; (b) input beam port 2 active; (c) central input beam port 3 active; (d) input beam port 4 active; (e) input beam port 5 active; (f) developed lens device with central input beam port 3 active, along with the deployed EM scale.

In order to experimentally validate the developed 28-GHz RL, a lens prototype has been accurately fabricated using the LPKF ProtoLaser U4 to deploy the laser-centric micromaterial and RF circuit structuring technique. Fig. 6 depict the fabricated lens prototype along with the peripherals as well as the RF measurement setup deployed for the testing. Moreover, Figs. 7 and 8 present the measured results, obtained based on the thorough measurements using the in-house vector network analyser (VNA), i.e. Keysight Technologies PNA-X, in order to rigorously measure both the amplitude and phase properties for the evaluation of the RF characteristics of the realised RL.

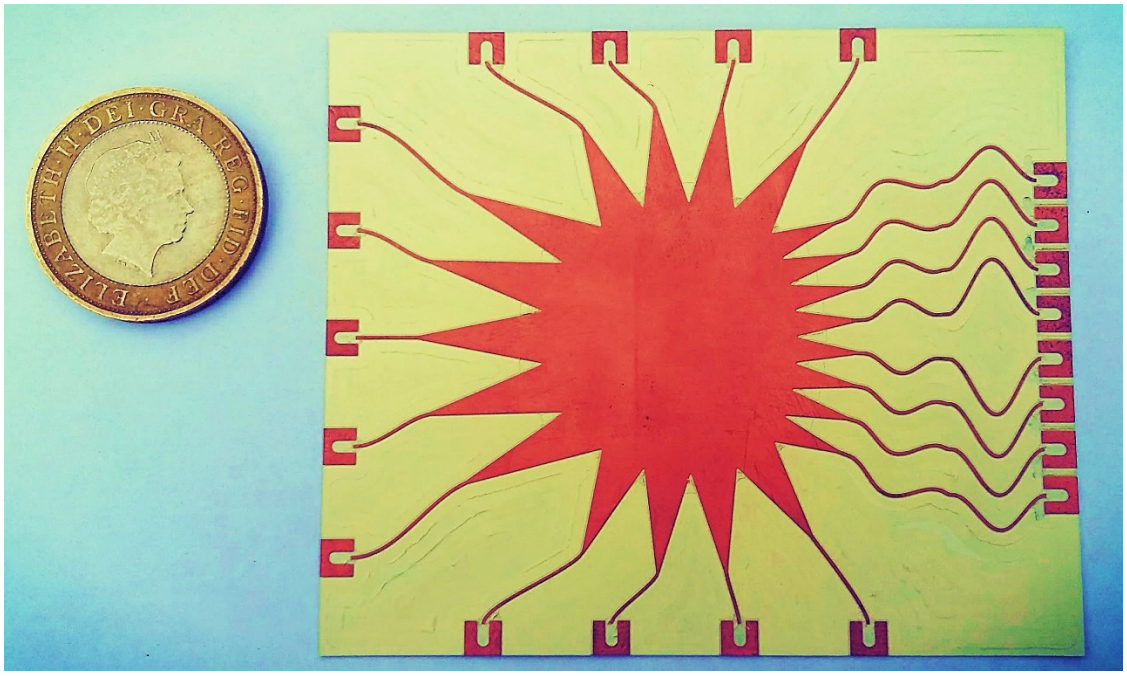

(a)

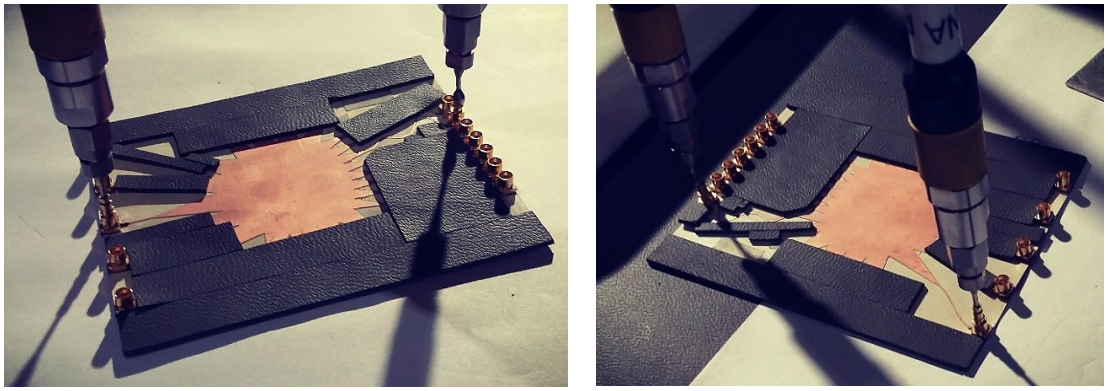

(b) (c)

Fig. 3.6. Experimental wideband mm-wave beamforming: (a) fabricated LCP-based 28-GHz 5 × 8 RL-BFN; (b) subsystem under test (SUT) for the excited central input beam port 3; (c) SUT for input beam port 1 active.

As Figs. 7 and 8 present, the measurements for the realised BFN has been conducted, in order to effectively examine the RF output performance of the lens device in terms of the magnitude levels, as well as the linear progressive phase division behaviour. The lens exhibits a wideband operation in the whole frequency range of 18–38 GHz, and the magnitudes are experiencing low-ripple profiles throughout the spectrum.

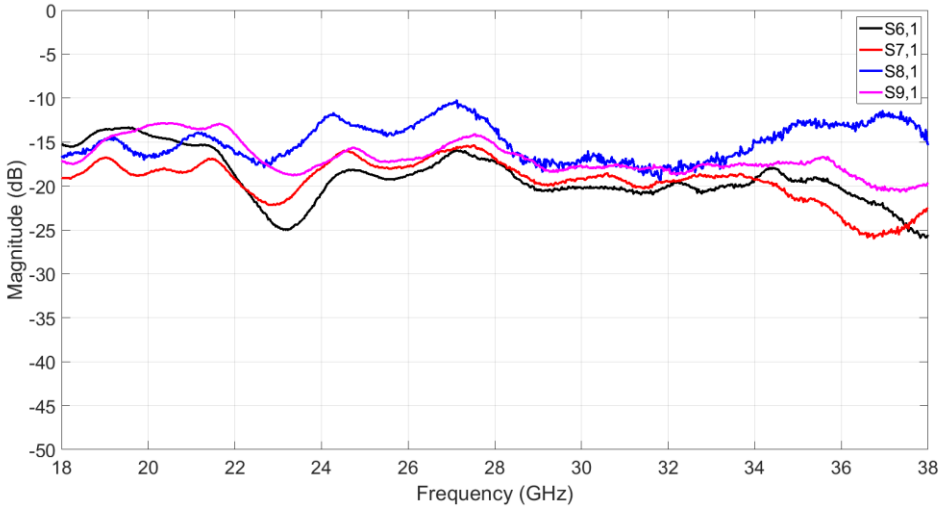

(a)

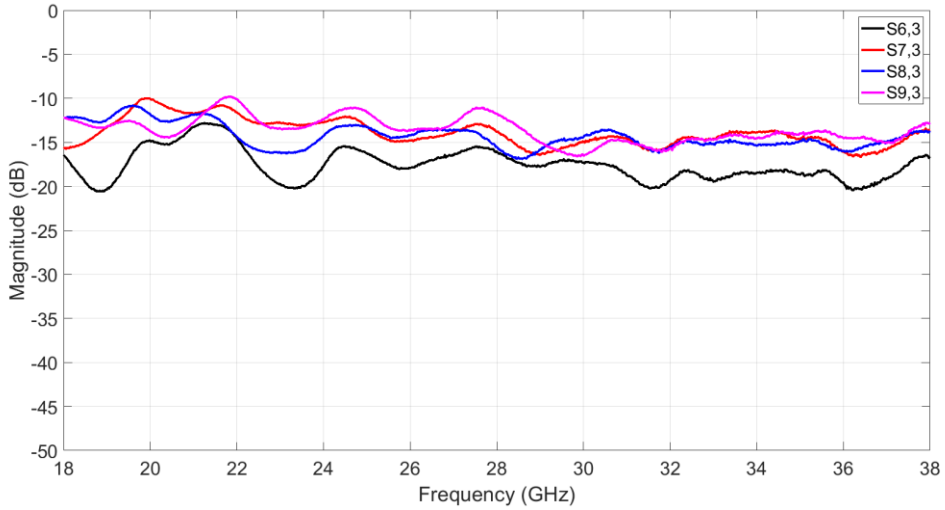

(b)

Fig. 3.7. Measured *S*-parameters of the planar LCP-based RL for the wideband operation: (a) transmission coefficients for RL port 1 active; (b) transmission coefficients for central port 3 active. It should be noted that the Pasternack PE44489 mini SMP male connectors have been used for the measurement, as well as the thin and flexible absorbing material ECCOSORB FGM-40 for terminating the ports except the two under test (i.e., Appendix A). The silver-filled conductive epoxy is also used for maintaining the electrical conductivity and high-strength conductive bonding, required for the connectors and terminals.

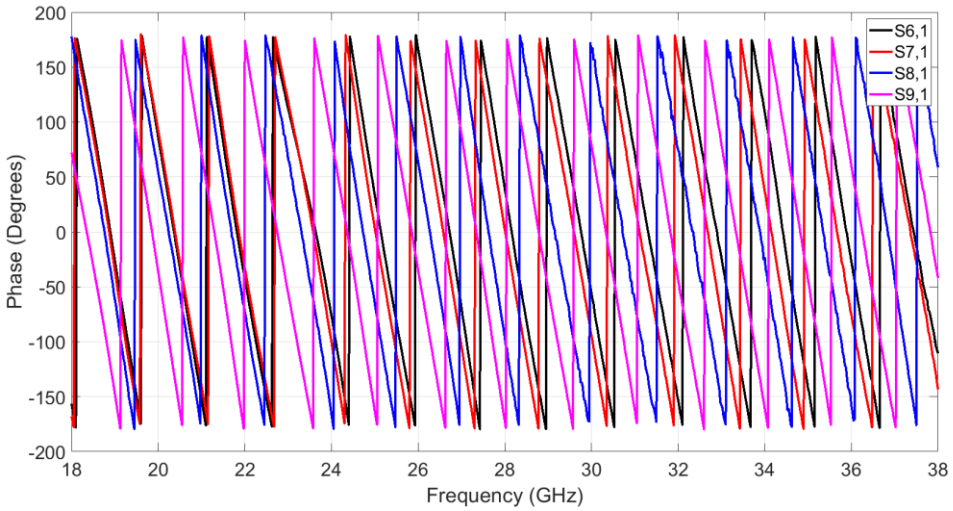

(a)

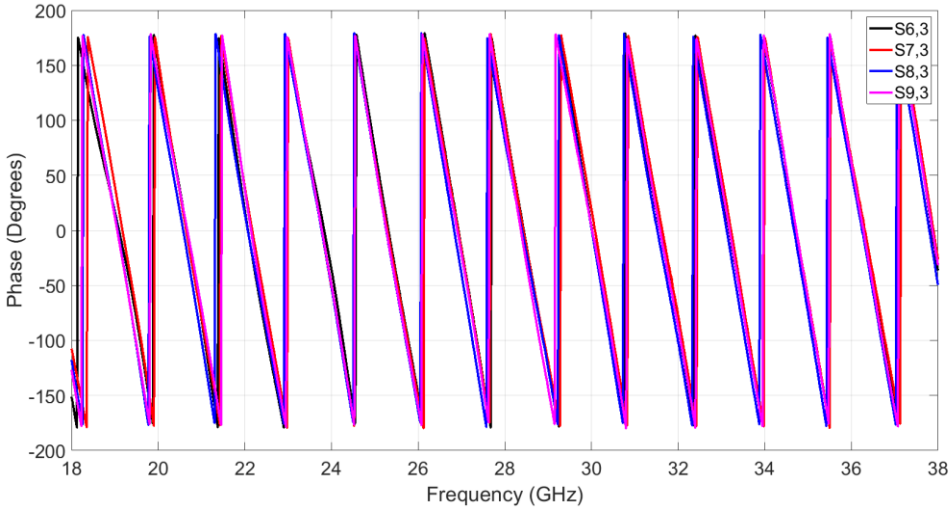

(b)

Fig. 3.8. Measured *S*-parameters of the planar LCP-based RL for the wideband operation: (a) linear phase distributions for input beam port 1 active; (b) linear phase distributions for central input beam port 3 active. It should be noted that the measurement has been conducted for the output array ports 6 to 9 due to the intrinsic symmetrical structure of the RL, and to further reduce the complexity and overhead of the measurement process.

3.3 Planar Design and Evaluation: The 28-GHz 7×10 RL-BFN

The design of the lens-based BFN has been further continued based on the original trifocal RL theory (i.e., Appendix B), in order to thoroughly design the mm-wave RL shown in Fig. 9 for operation in the 18–38 GHz frequency band. This lens has been enhanced in terms of the minimised phase error, as well as the improved scanning coverage of ±45˚. This lens has been also developed based on the Rogers ULTRALAM LCP substrate, with the dielectric constant of ε_r = 2.9, loss tangent of tanδ = 0.0025, substrate thickness of h = 0.1 mm, and top- and bottom-cladding of t = 9 μm. The focal ratio (g) is tuned to the value of 1.215, in order to minimise the phase error.

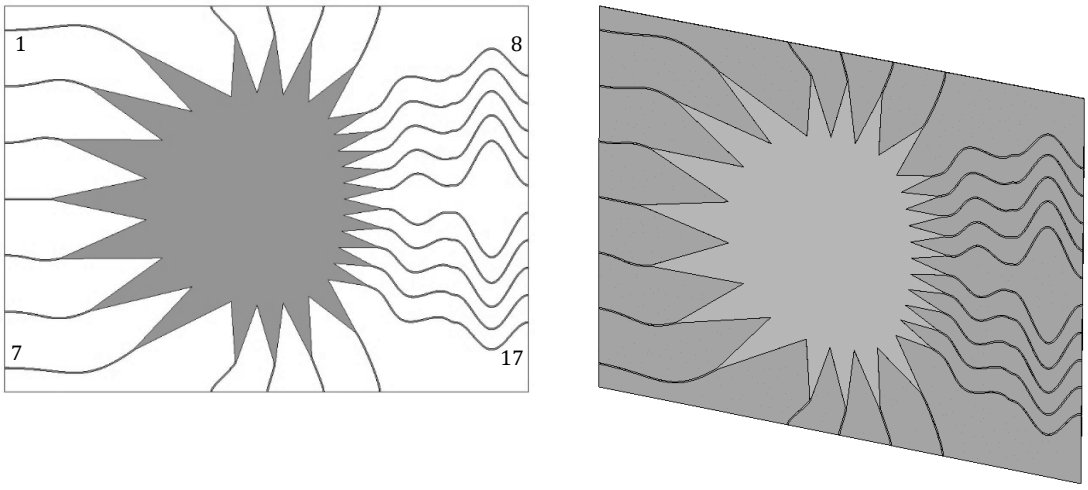

(a) (b)

Fig. 3.9. Planar LCP-based wideband 28-GHz RL-BFN: (a) wideband RL device with 7 input beam ports, 10 output array ports, and 8 absorbing dummy ports, with the dimensions of 75.38 × 102.46 mm², front view; (b) perspective view.

Figs. 10 and 11 comprehensively present the output characteristics of the developed 28-GHz RL-BFN, in terms of the transmission coefficients, isolations among the input ports, reflection coefficients, and linear progressive phase divisions, for input beam ports one and four (i.e., the central input beam port) activated. In addition, Fig. 12 depicts the surface current distributions for the excited beam ports one and four.

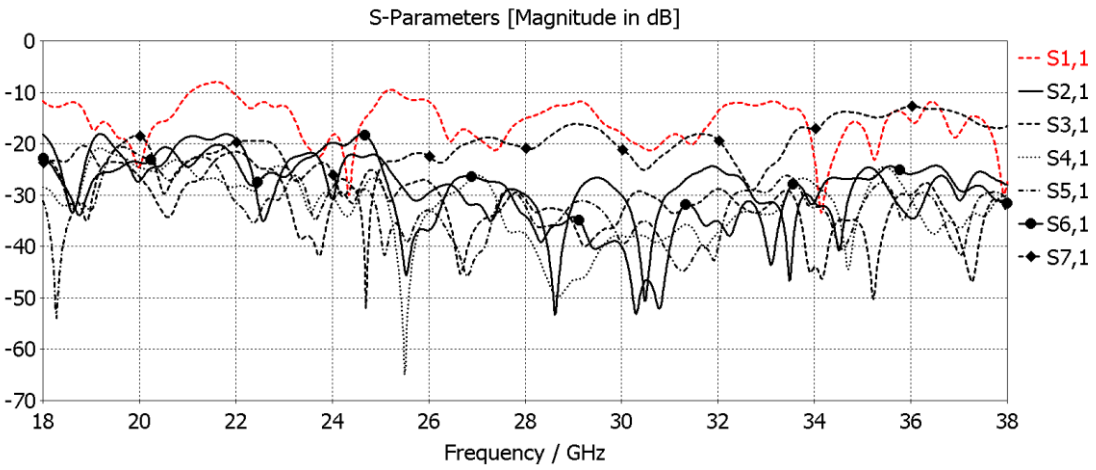

(a)

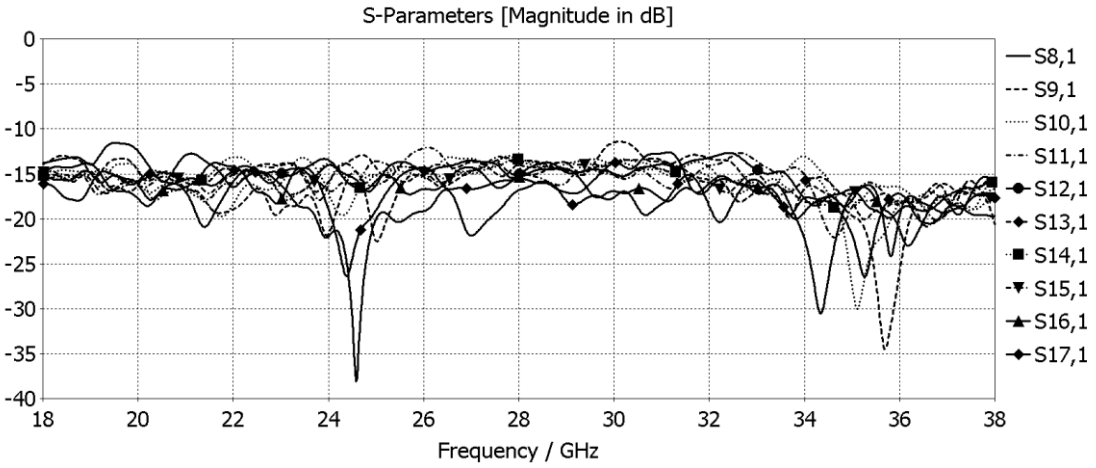
S-Parameters [Magnitude in dB]
0
-5
-10
-15
-20
-25
-30
-35
-40
18
20
22
24
26
28
30
32
34
36
38
Frequency / GHz
S8,1
S9,1
S10,1
S11,1
S12,1
S13,1
S14,1
S15,1
S16,1
S17,1

(b)

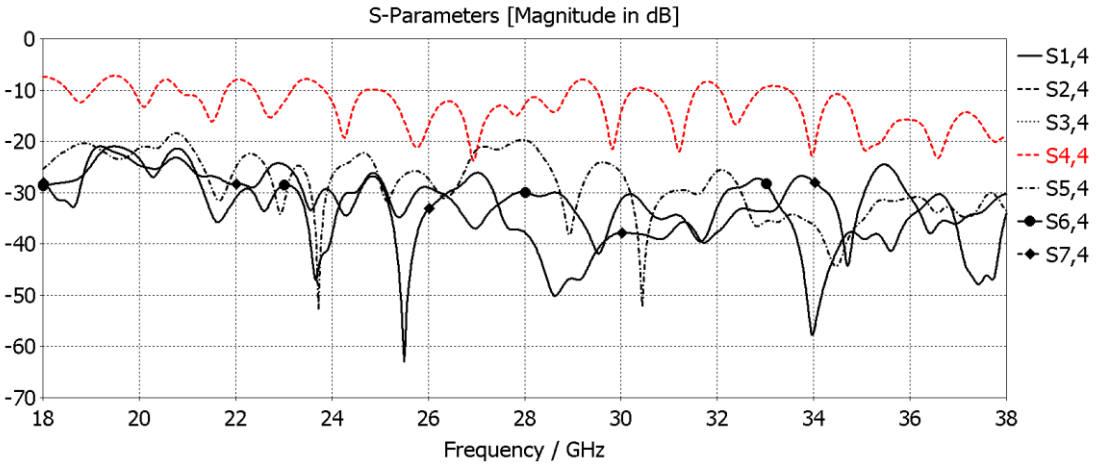
S-Parameters [Magnitude in dB]
0
-10
-20
-30
-40
-50
-60
-70
18
20
22
24
26
28
30
32
34
36
38
Frequency / GHz
S1,4
S2,4
S3,4
S4,4
S5,4
S6,4
S7,4

(c)

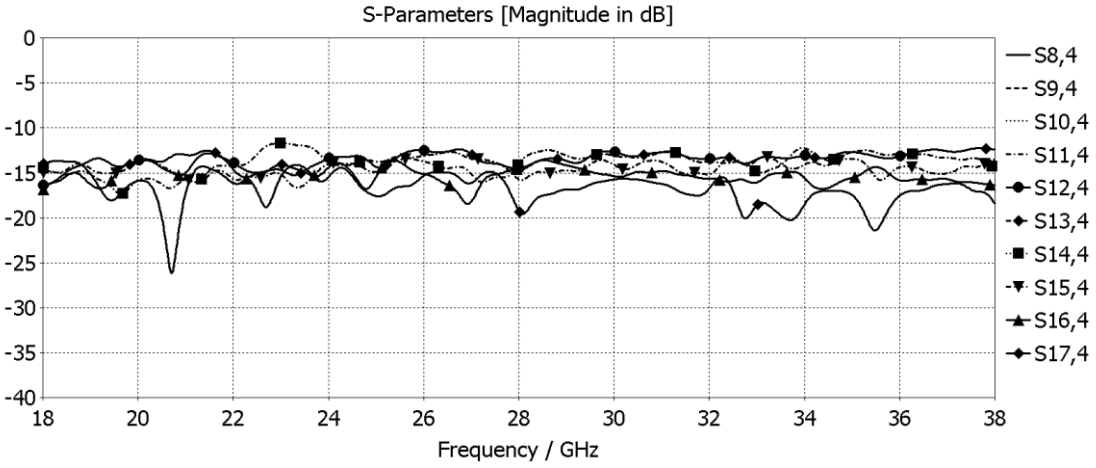
S-Parameters [Magnitude in dB]
0
-5
-10
-15
-20
-25
-30
-35
-40
18
20
22
24
26
28
30
32
34
36
38
Frequency / GHz
S8,4
S9,4
S10,4
S11,4
S12,4
S13,4
S14,4
S15,4
S16,4
S17,4

(d)

Fig. 3.10. Simulated *S*-parameters of the planar LCP-based RL for the wideband operation: (a) reflection coefficients for port 1 active; (b) transmission coefficients for port 1 active; (c) reflection coefficients for port 4 active; (d) transmission coefficients for port 4 active.

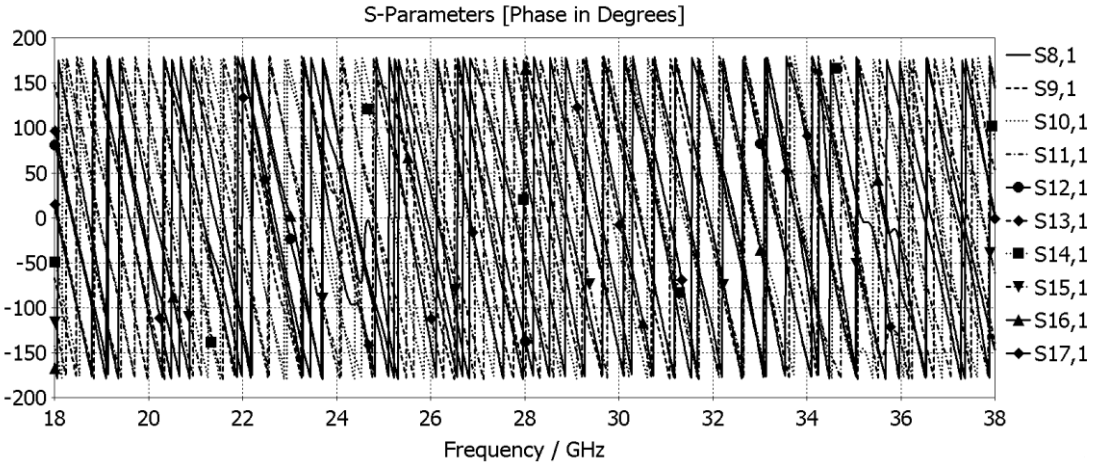

(a)

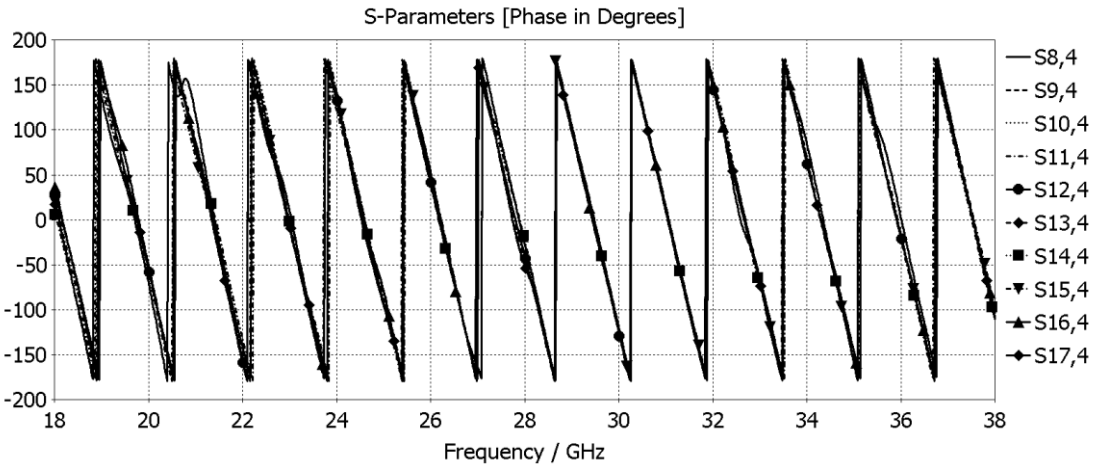

(b)

Fig. 3.11. Simulated *S*-parameters of the developed planar LCP-based 28-GHz RL-BFN for the wideband operation: (a) linear progressive phase distributions for input beam port 1 active; (b) linear progressive phase distributions for central input beam port 4 active.

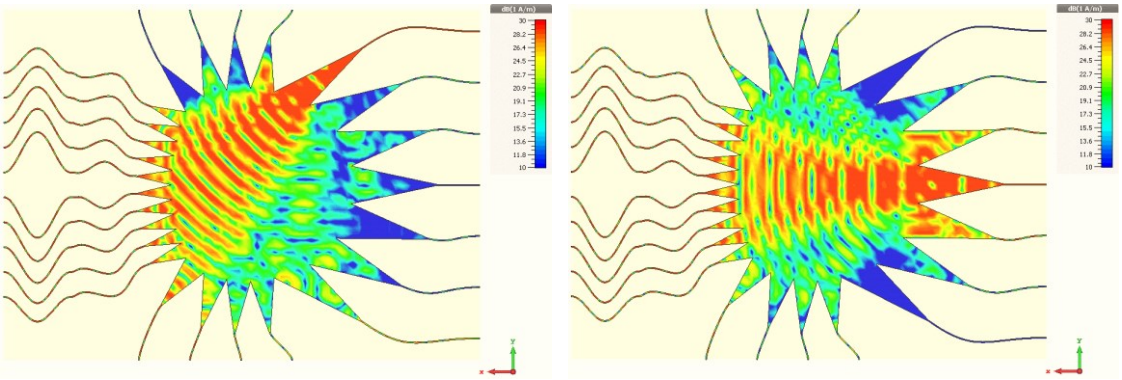

(a) (b)

Fig. 3.12. Surface current distributions of the developed LCP-based wideband RL-BFN for the excited beam ports at mm-wave centre frequency f = 28-GHz: (a) input beam port 1 active, exerting the minimum device efficiency of 34.9%; (b) central input beam port 4 active, exerting the maximum device efficiency of 39.1%.

3.4 Planar Design and Evaluation: The 60-GHz 5×8 RL-BFN

The full-wave EM simulations regarding the design of the planar 60-GHz lens have been thoroughly carried out, and the output characteristics, including the beam to array coupling amplitudes, and the return and insertion losses, have been presented for the operating frequency band, i.e., Fig. 13. The lens has been developed based on the 5 × 8 configuration, in which the LCP-based BFN incorporates five input beam ports and eight output array ports, suitable for an eight-element array, along with eight dummy ports, to absorb the energy and to reduce the reflections on each side of the lens cavity. The RL has the scan angle of ±30˚ with the half-wavelength array element spacing. The designed RL has the structure that connects the beam contour to the output array contour for the optimum power distribution across the output array ports, along with the linear phase progression among the adjacent elements.

As Fig. 13 shows, the lens has been implemented based on the LCP substrates with different configurations and curvatures, namely the square-shaped substrate, edge-shaped substrate, and extrusion-shaped substrate. These substrates incorporate the copper layers for the lens and ground planes at the top and bottom of the device, in order to assess the effects of the introduced configurations on the performances. All the introduced variations in the substrates have been analysed based on the HPC-based full-wave EM simulations, in order to evaluate the performance of the RLs.

Moreover, the parameters have been examined according to the variations in the *S*-parameters, consequently in the device efficiencies, based on the excited ports. The results confirm an almost uniform behaviour among the RL-BFNs with the different substrate configurations. This process can facilitate the analysis of the interaction in the case of the presence of the active and passive RF components within a module for the integration purposes, as in the embedded systems development (ESD).

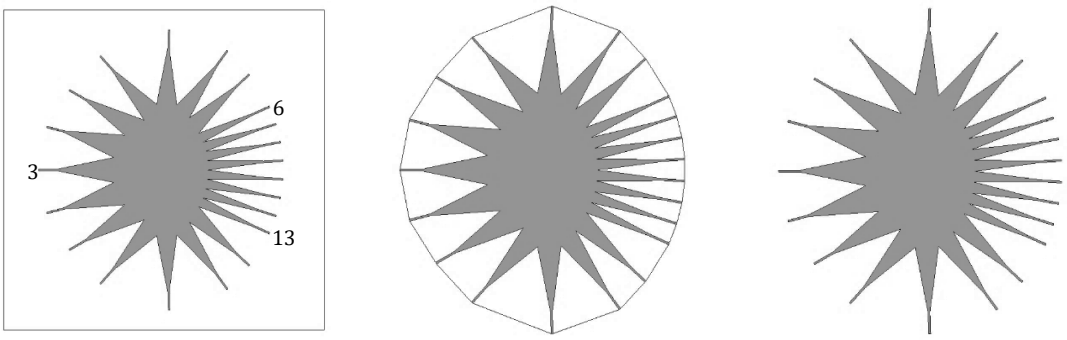

(a) (b) (c)

Fig. 3.13. Planar LCP-based 60-GHz (i.e., h = 0.1 mm and t = 9 μm) BFNs with 5 beam ports, 8 array ports, and 8 absorbing dummy ports, with the dimensions of 38.12 × 43.86 mm^2: (a) RL-I: the square-shaped substrate configuration; (b) RL-II: the edge-shaped substrate configuration; (c) RL-III: the extrusion-shaped substrate configuration.

The comprehensive simulations have been carried out to analyse the characteristics of the proposed designs. Fig. 14 indicates the *S*-parameters' magnitudes for the lens with beam ports one to three excited. Because of the intrinsic symmetrical structure of the lens, the performances of beam ports one and two are theoretically identical to the performances of beam ports five and four, respectively. The magnitudes have low-ripples (i.e., less than 6 dB) over the intended frequency range exhibiting almost linear distributions across the array ports. Moreover, the *S*-parameters confirm the wideband operation of the lens device, and further realise the output performances based on the behavioural conformity according to the generalised RL-BFN theory.

Furthermore, as Fig. 15 presents in detail, an extra output analysis and performance evaluation of the developed 60-GHz RL-BFN has been conducted for input beam port three active, based on the increased numerical discretisation's resolution using the deployed robust EM transient solver. This has been performed to further assess the accuracy of the conducted simulations, and to examine the margin of error using the employed software. This process has resulted in the increased level of precision for the verification and comparison of the simulated results and can be used for the RF sensitivity assessments based on the background materials, permittivity values, and EM boundary conditions. Fig. 15 also presents the characteristics for the input beam port three, based on the mesh-discretisation with 20 lines per wavelength. As it can be seen from the *S*-parameters' magnitude plots, the lens device still conforms to the expected behaviour, in both the high-resolution EM cases (i.e., the 10 and 20 lines per wavelength, introduced as part of the software-stage design) that have resulted in the isolation among the inputs, and the reflection and transmission coefficients.

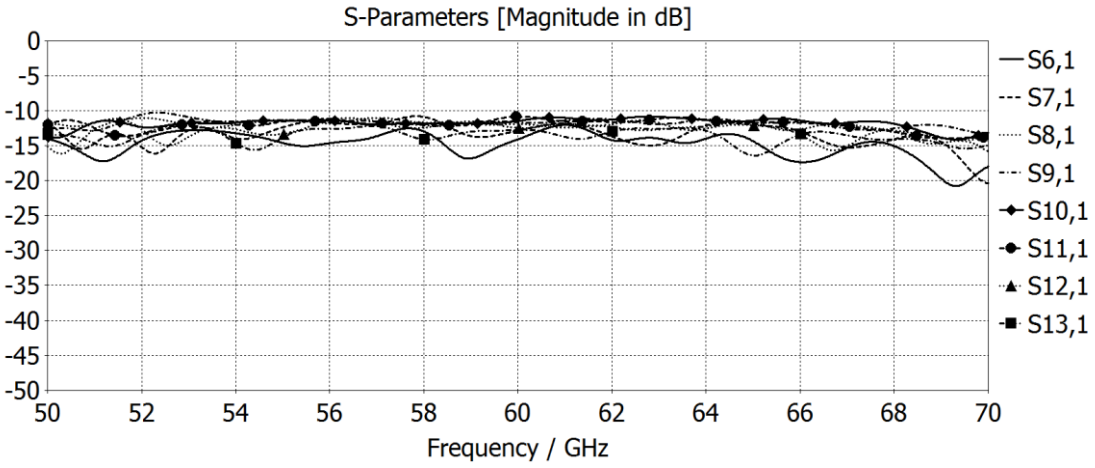
S-Parameters [Magnitude in dB]
0
-5
-10
-15
-20
-25
-30
-35
-40
-45
-50
50
52
54
56
58
60
62
64
66
68
70
Frequency / GHz
S6,1
S7,1
S8,1
S9,1
S10,1
S11,1
S12,1
S13,1

(a)

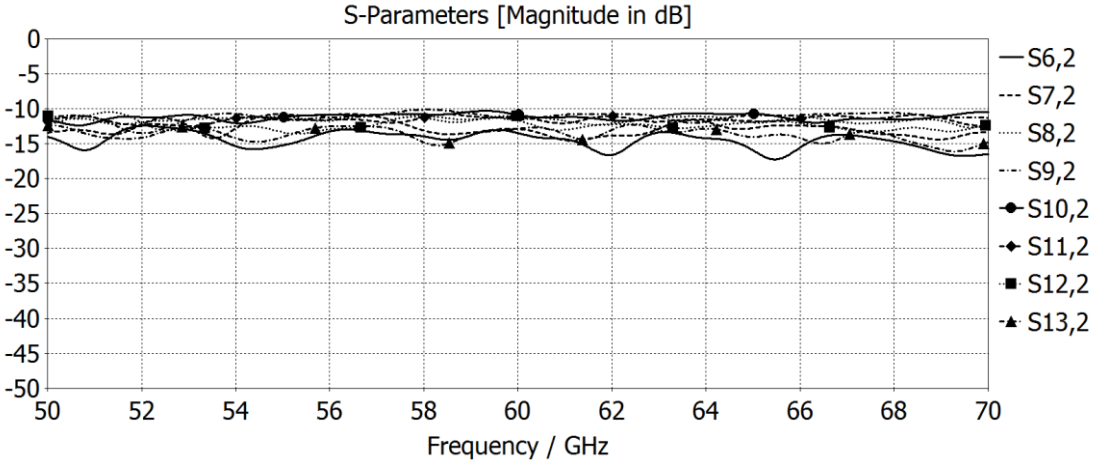
S-Parameters [Magnitude in dB]
0
-5
-10
-15
-20
-25
-30
-35
-40
-45
-50
50
52
54
56
58
60
62
64
66
68
70
Frequency / GHz
S6,2
S7,2
S8,2
S9,2
S10,2
S11,2
S12,2
S13,2

(b)

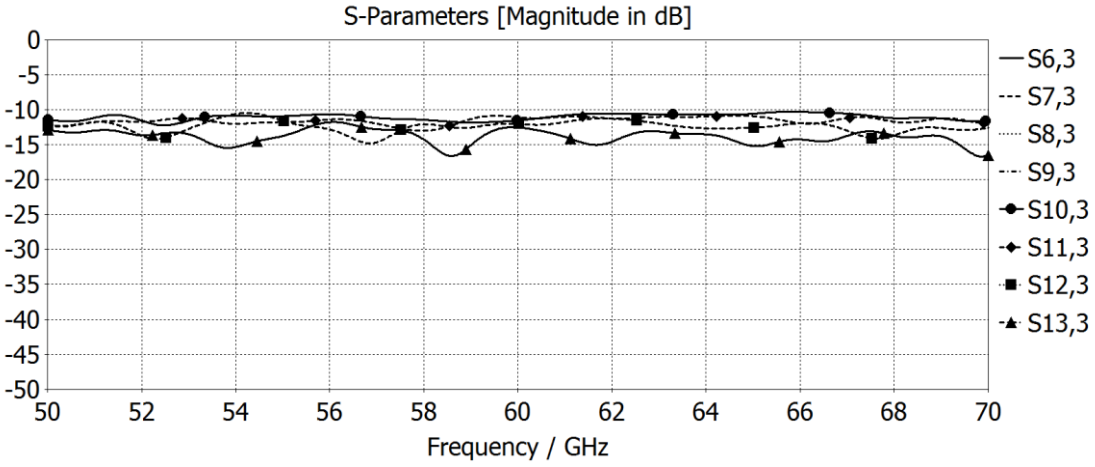
S-Parameters [Magnitude in dB]
0
-5
-10
-15
-20
-25
-30
-35
-40
-45
-50
50
52
54
56
58
60
62
64
66
68
70
Frequency / GHz
S6,3
S7,3
S8,3
S9,3
S10,3
S11,3
S12,3
S13,3

(c)

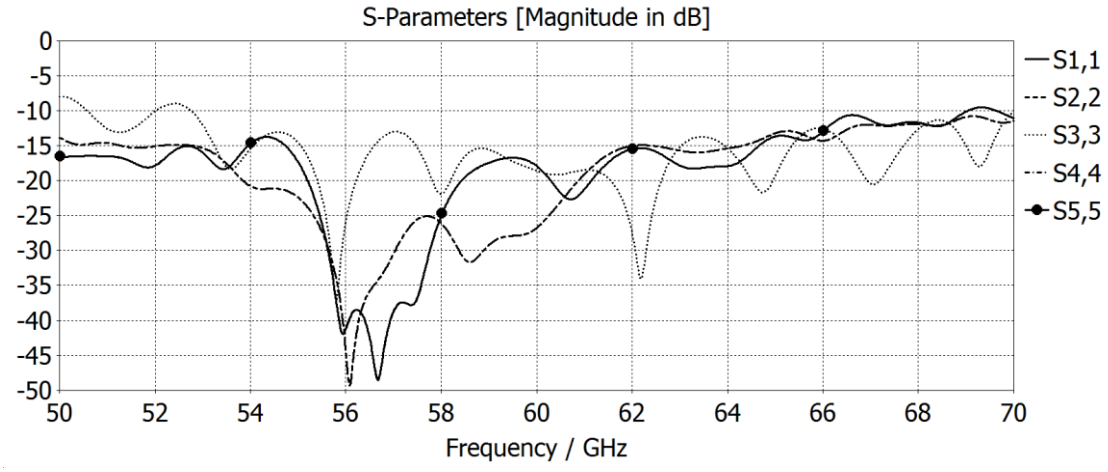

(d)

Fig. 3.14. Simulated *S*-parameters and output characteristics of the developed planar LCP-based RL for the wideband operation: (a) transmission coefficient plots for input beam port 1 active; (b) transmission coefficient plots for beam port 2 active; (c) transmission coefficient plots for beam port 3 active; (d) reflection coefficient plots for excited input beam ports 1 to 5.

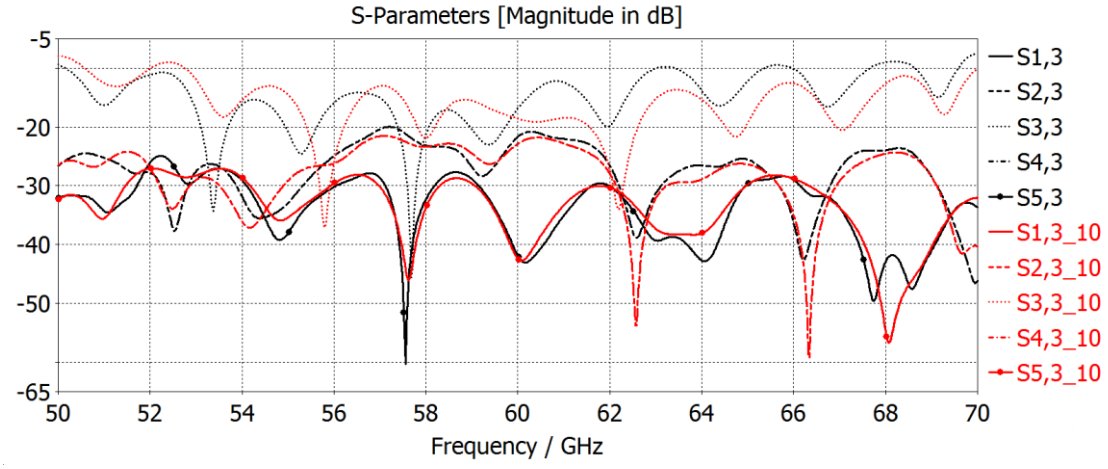

(a)

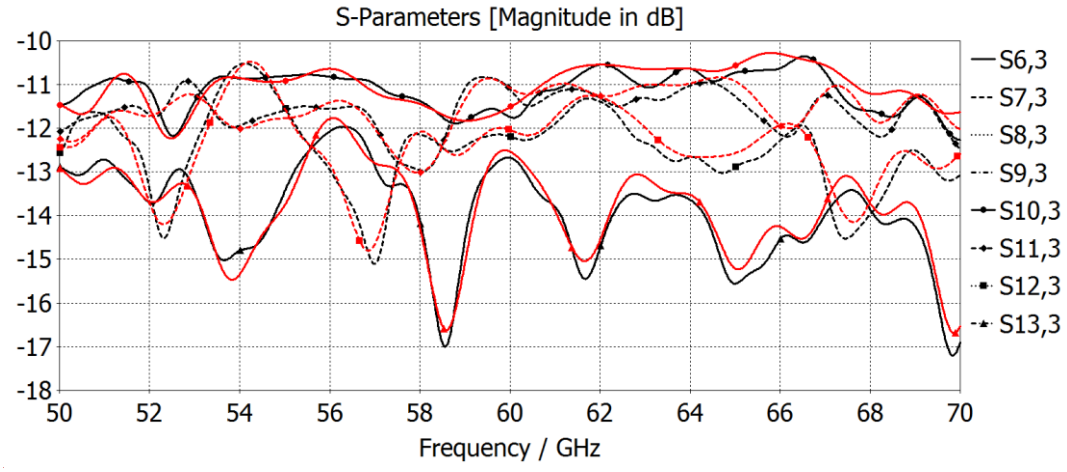

(b)

Fig. 3.15. Comparison of the simulated characteristics of the LCP-based 60-GHz RL-BFN for central input beam port 3 active, based on different mesh-discretisation resolutions: (a) reflection coefficient and isolation plots; (b) transmission coefficient plots.

Moreover, Fig. 16 shows the surface current distributions of the planar LCP-based RL for the activated input beam ports one to five. As Fig. 16 presents, the maximum power is delivered to the output array ports, and the progressive surface currents confirm the high-performance operation of the device. The lens efficiently conducts the energy distributions across the array ports, effectively resulting in the provision of the beam scanning functionality for the utilisation of the wireless subsystems.

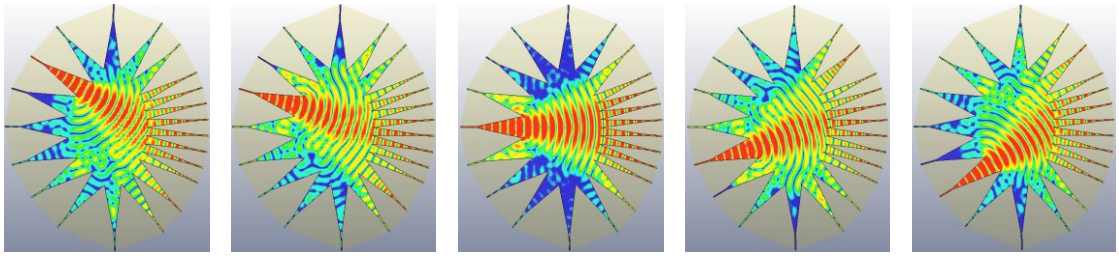

(a) (b) (c) (d) (e)

Fig. 3.16. Surface current distributions of the LCP-based wideband RL-BFN for the excited input beam ports at mm-wave centre frequency f = 60-GHz: (a) input beam port 1 active; (b) input beam port 2 active; (c) central input beam port 3 active; (d) input beam port 4 active; (e) input beam port 5 active. It should be noted that the EM scale for this RL design, as well as the other 60-GHz ones, are uniformly deployed as the one in Chapter 4, Fig. 5.

3.5 Summary

This chapter has thoroughly presented the numerical and experimental design and performance evaluations of the wideband mm-wave RL-based array BFNs, based on the rigorous and high-resolution computational full-wave EM simulations, as well as the experimental performance verifications using the fabricated lens prototype and the conducted RF measurements for the RL device. The thoroughly shown simulated and measured results confirm the high-performance operation of the mm-wave RLs, in terms of exhibiting significant output characteristics, including the linear and low-ripple amplitude distributions across the array ports of the RLs, progressive phase division among the output array ports, wideband operation of the mm-wave lenses with the minimised phase error, and efficient surface current distributions over the output array contours. The developed LCP-based RLs realised based on the original trifocal constituent design equations (i.e., Appendix B), as well as the RL parameters' intrinsic functionalities. Therefore, the proposed BFNs provide the antenna systems with the high-performance and low-profile subsystems capable of electronic beam steering, required for the efficient deployment and utilisation of the next-generation wireless communication systems, based on the advanced mm-wave technologies.

Chapter 4:

Analytical and Experimental Evaluation of Flexible 28-GHz and 60-GHz Rotman Lens-Based BFNs for Next-Generation Wireless Communication Subsystems

4.1 Introduction

This chapter presents the design and analysis of the LCP-based flexible 60-GHz and conformal 28-GHz RL-BFNs, in order to investigate the feasibility of the flexural and conformal functionality, introduced intrinsically into the case of the Rotman lenses. The full-wave EM simulations have been thoroughly carried out for the developed structures with the specific flexural degrees, based on the four introduced flexures. Furthermore, the comprehensive HPC-based EM simulations for the surface current distributions and phase profile behaviour along with the numerical device efficiency analysis, as the primary figures of merit for the validation of the high-performance mm-wave operation, have been appropriately conducted for each flexural case. This is of crucial importance to propose the concept of the conformal and flexible RLs.

4.2 Design and Analysis of Flexible 5×8 RL-BFNs

Fig. 1 presents the four unique proposed flexures, namely the concave-axial bending, convex-axial bending, concave-circumferential bending, and convex-circumferential bending. Moreover, their individual characteristics, in terms of the surface currents and phase distributions, are presented in the following sections. The performances of the RL-BFNs conform to the deployment requirements of the advanced wireless communication systems and can be further integrated with the radiating elements, in order to build up the flexible modules for the potential hybrid applications, such as the conformal wireless backhaul subsystems. The lens devices can be used for the potential realisation of the retrodirective systems. In this case, the characteristics of the devices enable the generated beams to be received from specific directions and to be transmitted back to the same sources without physical arrangements, in order to realise the intelligent beam alignment functionalities. This kind of beam scanning is faster than the conventional methods, and further provides the feasibility for the realisation of smart antennas, in which the patterns are changed according to the environment, that offer impressive properties, including the high-performance in terms of the RF signal quality, interference and noise-suppression, and capacity.

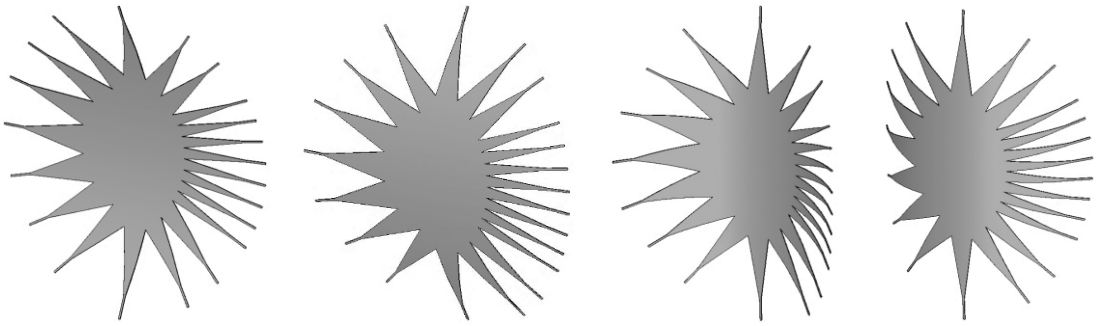

(a) (b) (c) (d)

Fig. 4.1. Perspective views of the proposed flexural cases based on the developed 60-GHz 5×8 RL-BFN: (a) the concave-axial bending; (b) the convex-axial bending; (c) the concave-circumferential bending; (d) the convex-circumferential bending. The developed flexures are the main flexibility and deformation cases, in order to evaluate their individual effects.

4.3 Flexural Case-I: The Concave-Axial Bending

Fig. 2 presents the surface current distributions for the 60-GHz RL based on the first flexural case (i.e., the concave-axial bending), along with the corresponding linear phase behaviour, for the excited input beam ports one and three, as the primary RF functionality indicators. It is worth noting that beam ports one and five determine the minimum device efficiency, since they are symmetrical on both ends of the lens and are placed on the furthest distance from the central focal point of the RF device. The activated beam port three exerts the maximum efficiency into the component, since it is placed on the central axis. Hence, the device efficiency can be expressed as the sum of the absolute squares of the output ports' linear transmission coefficients. Each set of parameters indicate different results, from which the device efficiency is determined. As Figs. 2 (a) and (c) depict, the surface current distributions confirm the efficient EM power division along the array ports of the component, and further confirming the linear phase distributions required for the mm-wave beam steering, in Figs. 2 (b) and (d). The minimum and maximum device efficiencies at the centre frequency of 60-GHz for the excited input beam ports one and three are numerically obtained as 47.1% and 51.7%, respectively, based on the presented equation (1).

$$RL\ BFN\ Device\ Efficiency = \frac{P_{RL_{out}}}{P_{RL_{in}}} = \sum_{n} \left|S_{(n,1),linear}\right|^2$$
$$= \left({S_{6,1}}^2 + {S_{7,1}}^2 + {S_{8,1}}^2 + {S_{9,1}}^2 + {S_{10,1}}^2 + {S_{11,1}}^2 + {S_{12,1}}^2 + {S_{13,1}}^2\right). \quad (4.1)$$

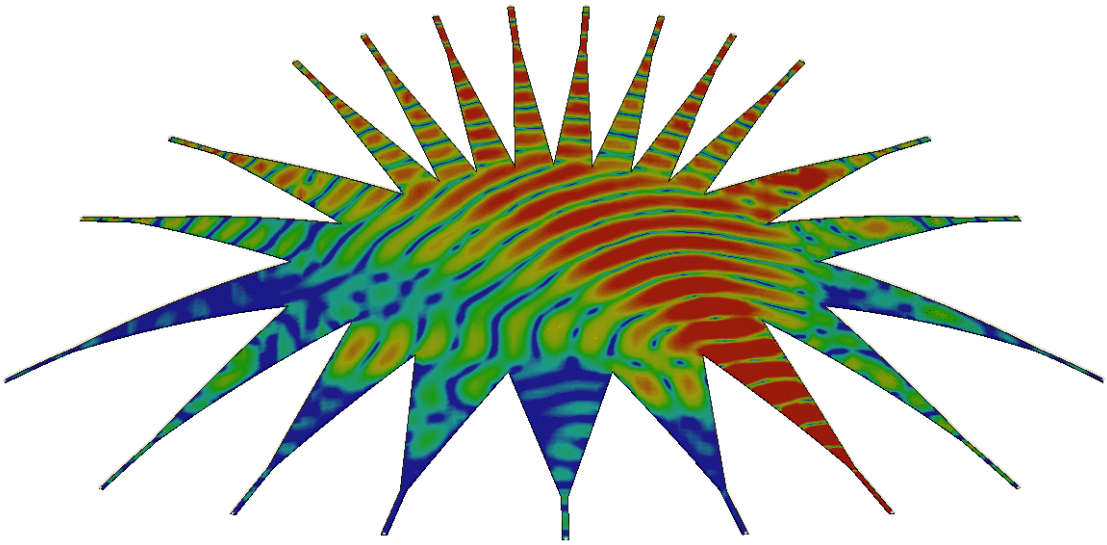

(a)

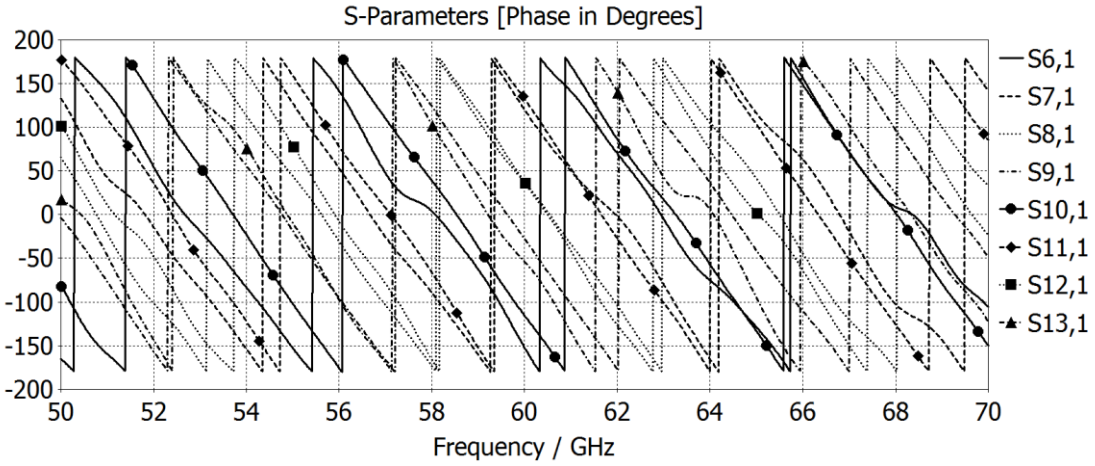

(b)

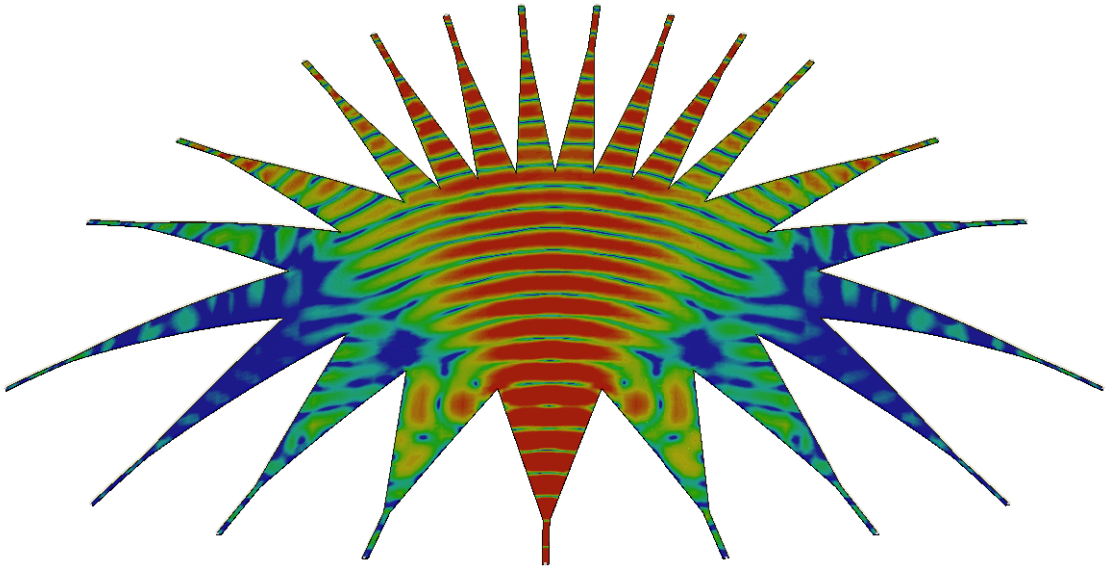

(c)

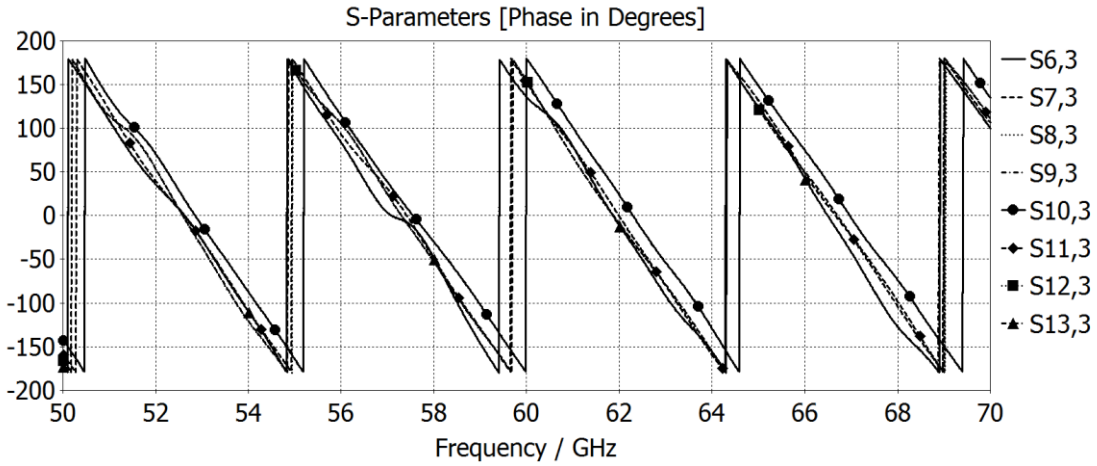

(d)

Fig. 4.2. RF performance characteristics of the 60-GHz LCP-based RL based on the flexural case of the concave-axial bending, in which the device is bent around a cylinder of radius R = 40 mm: (a) surface currents for input beam port 1 active; (b) linear progressive phase distributions for input beam port 1 active; (c) surface currents for central input beam port 3 active; (d) linear progressive phase distributions for central input beam port 3 active.

4.4 Flexural Case-II: The Convex-Axial Bending

This section presents the characteristics of the designed flexible RL based on the flexure of the convex-axial bending. Fig. 3 presents the surface current distributions for the excited input beam ports one and three corresponding to the exertions of the minimum and maximum device efficiencies, respectively. The phase distributions based on the activated ports are shown in Figs. 3 (b) and (d), in order to present the RF beam steering in terms of the required phase behaviour. Hence, multiple beams without the need for phase shifters have been generated based on the proposed RF component with the wideband operation and wide-angle scanning capabilities. All the generated beams can be used simultaneously or can be switched at high rates, which results in the pattern diversity for the potential MIMO systems, in which an extra RF radio at each beam port can be further integrated for the hybrid mm-wave module development to be deployed for the next-generation wireless subsystems.

Moreover, the minimum and maximum device efficiencies are obtained as 47.8% and 51.7% for the excited input beam ports one and three, respectively. The flexible RL can be extensively used as a subsystem core of the requirements for the backhaul infrastructures. The device can also be integrated with the systems where the high-capacity and reliable data transmission, based on the implemented components and adaptive processing, are of critical demand among the APS, in order to effectively maintain the electronic beam steering functionality based on the advanced low-cost and lightweight mm-wave modules. Hence, the deployment of the 60-GHz conformal antenna array, in hybrid, integrated, or multilayer configurations, would effectively result in the constructive spatial power distribution based on the vector sum of the

EM fields radiated by the individual antenna elements, and the amplitude and phase distributions applied to the individual elements of the array based on the RL-BFN.

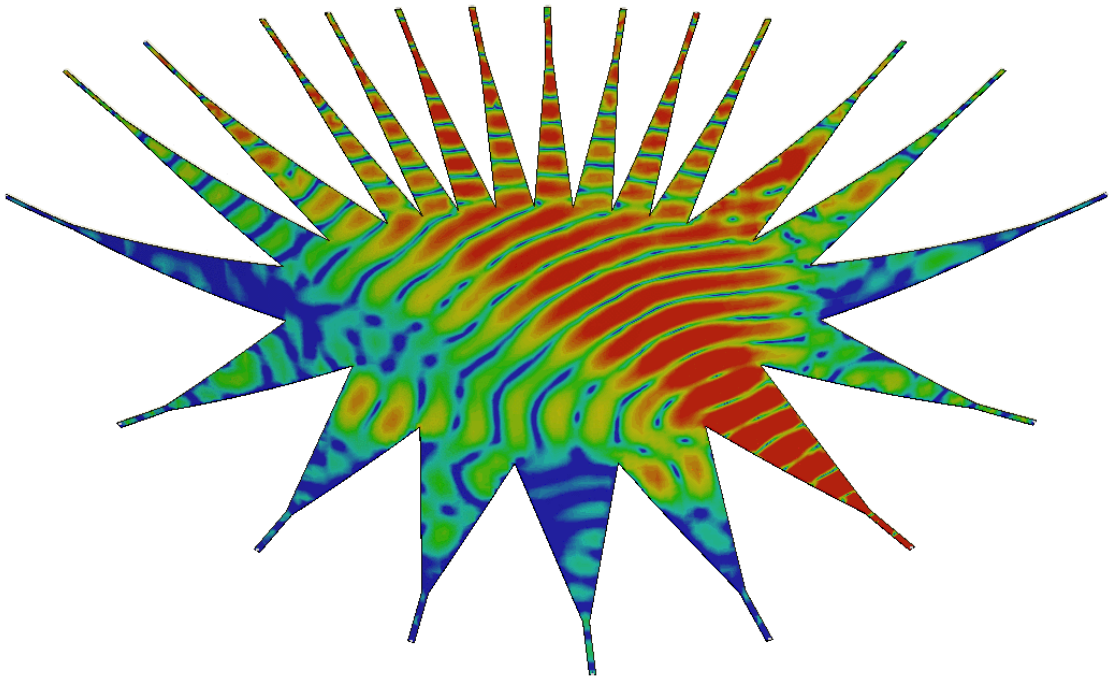

(a)

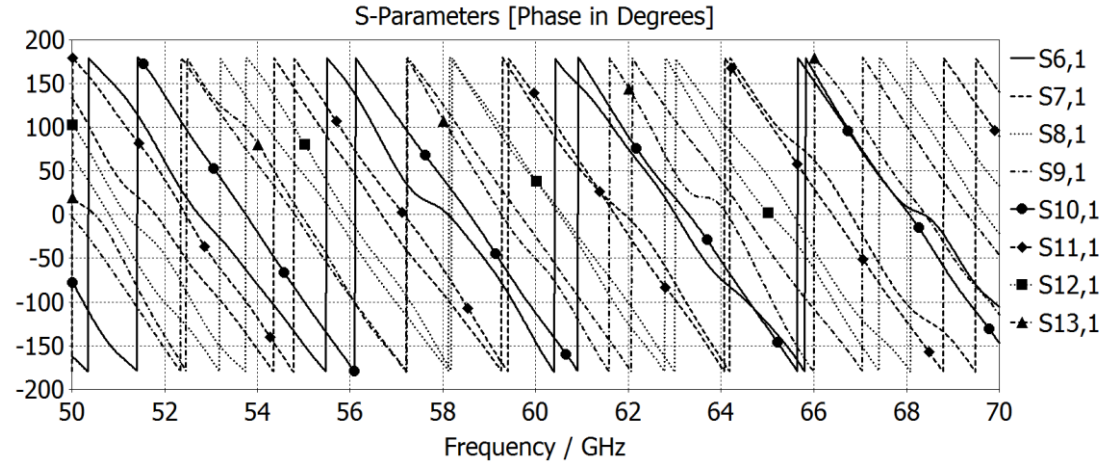

(b)

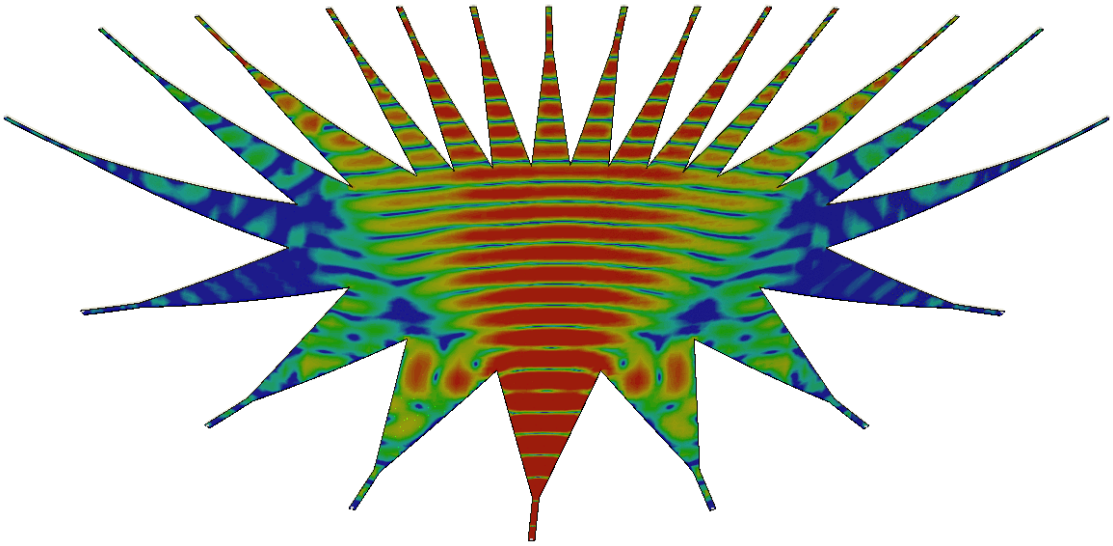

(c)

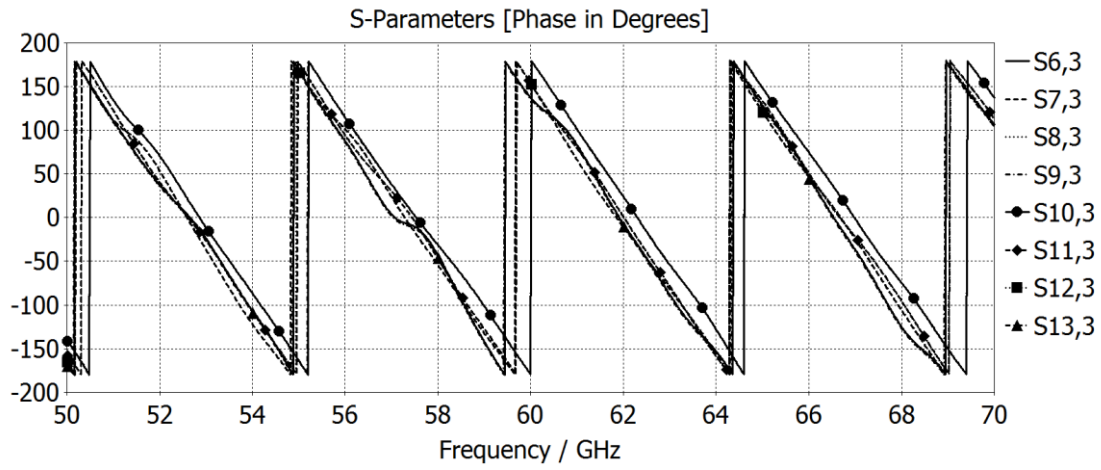

(d)

Fig. 4.3. RF performance characteristics of the 60-GHz LCP-based RL based on the flexural case of the convex-axial bending, in which the device is bent around a cylinder of radius R = 40 mm: (a) surface currents for input beam port 1 active; (b) linear progressive phase distributions for input beam port 1 active; (c) surface currents for central input beam port 3 active; (d) linear progressive phase distributions for central beam port 3 active.

4.5 Flexural Case-III: The Concave-Circumferential Bending

This section shows the performance of the proposed mm-wave component based on the third flexural case, in which the 60-GHz LCP-based beamformer is bent around a cylinder to form the structure of the concave-circumferential bending. Hence, Fig. 4 shows the characteristics of this flexure, for the excited input ports one and three. As Figs. 4 (a) and (c) show, the surface current distributions throughout the RF lens confirm the effective energy distribution along the array ports, with the maximum and minimum intensities being appropriately delivered to the output array ports and dummy ports, respectively. As Figs. 4 (b) and (d) depict, the phase behaviour of each individual excited beam port confirms the linear distributions required for the systematic RF electronic beam scanning functionality. The minimum and maximum device efficiencies, for the excited input ports one and three at the centre frequency of 60-GHz, are also numerically computed as 45.8% and 54.2%, respectively.

The RL is operative based on the TTD functionality, and as expressed in (2), when the lens is switching between the input ports, the radiated RF beam can be scanned through the field of view (FOV) of the RF device to achieve a high angular resolution through the progressive linear time-delay (i.e., denoted by $\Delta\tau$) across the RF output array elements. This further results in the constructive interference, along with the delay between the adjacent elements with the constant separation (i.e., denoted by D) that generates the EM radiation pattern relative to the central axis of the RF lens. Hence, as noted in (2), where c is the speed of light and θ_s is the scan angle, the RL is the TTD device, which confirms that the beam scan angle depends solely on the time-

delay, since in the TEM-based transmission mediums, $\Delta\tau$ is frequency-independent. Hence, the scan angle does not vary with the frequency, which enables the provision of RF features to be further exploited for the conformal wireless applications.

$$\xrightarrow{TTD} \theta_s = sin^{-1}\left(\frac{c\Delta\tau}{D}\right). \tag{4.2}$$

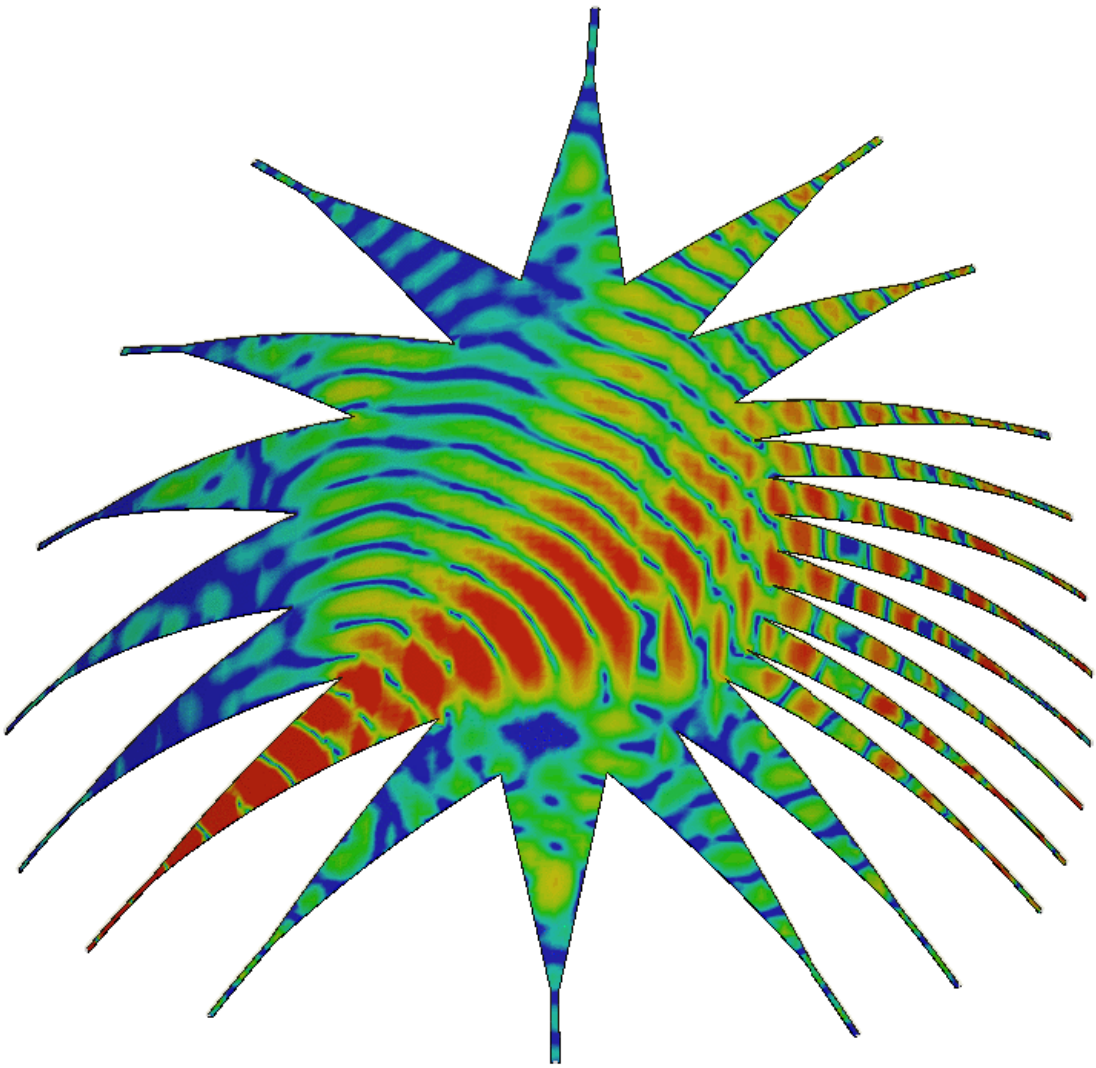

(a)

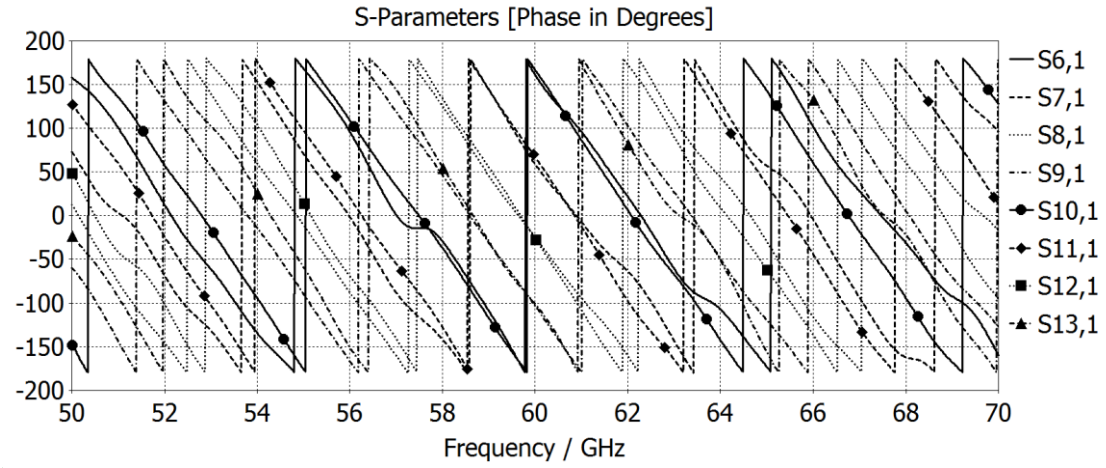
S-Parameters [Phase in Degrees]
200
150
100
50
0
-50
-100
-150
-200
50
52
54
56
58
60
62
64
66
68
70
Frequency / GHz
S6,1
S7,1
S8,1
S9,1
S10,1
S11,1
S12,1
S13,1

(b)

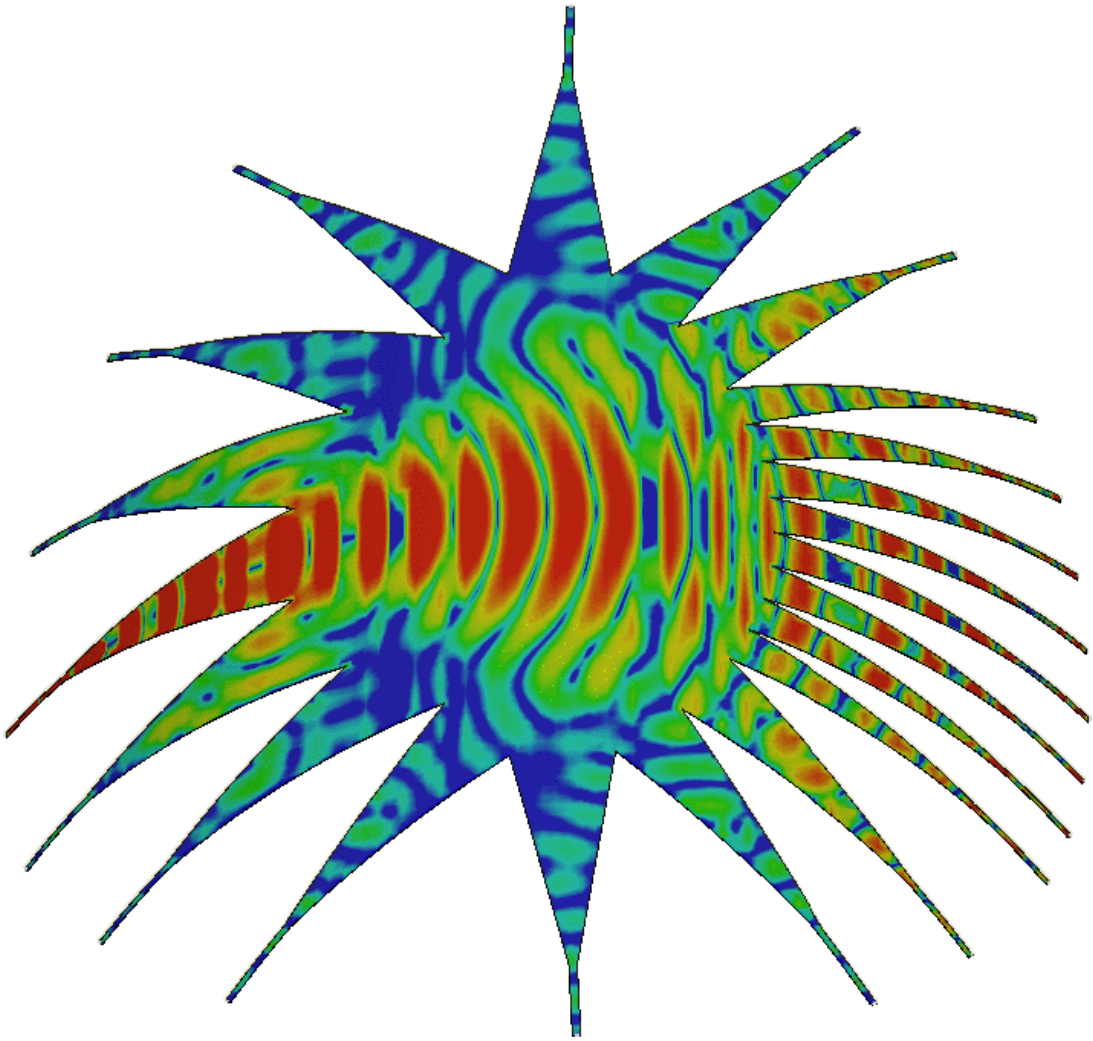

(c)

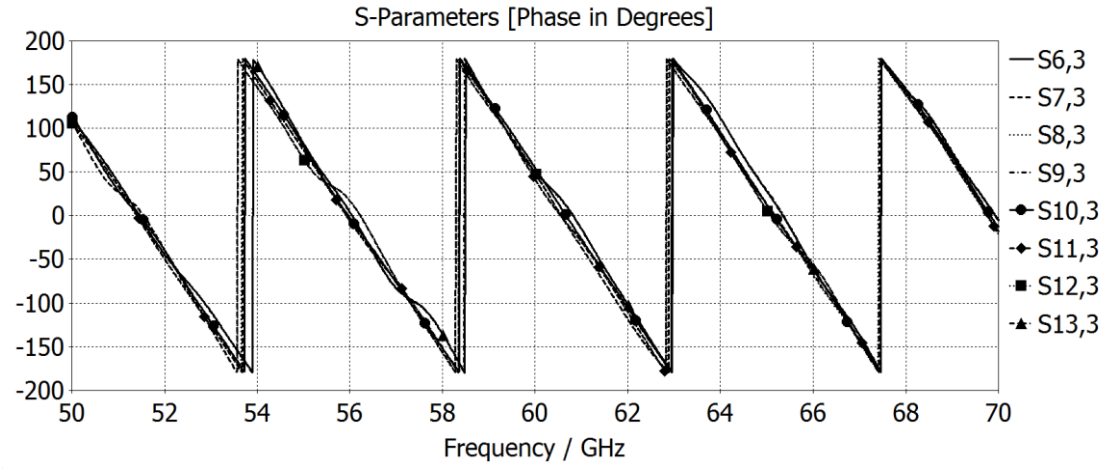

(d)

Fig. 4.4. RF performance characteristics of the 60-GHz LCP-based RL based on the flexural case of the concave-circumferential bending, in which the device is bent around a cylinder of radius R = 20 mm: (a) surface currents for the excited input beam port 1; (b) surface currents for the excited input beam port 3; (c) linear progressive phase behaviour for the excited input beam port 1; (d) linear progressive phase behaviour for the excited central input port 3 over the main axis, incorporating the elements of the central beam of the AF.

4.6 Flexural Case-IV: The Convex-Circumferential Bending

Figure 5 (a) shows the surface current distributions for the lens device based on the flexural case of the convex-circumferential bending with beam port one active, along with the corresponding linear phase behaviour, as presented in Fig. 5 (b). Also, Fig. 5 (c) shows the surface current distributions in the case of the maximum efficiency's exertion based on the excited beam port three, which is followed by its linear phase behaviour, as shown in Fig. 5 (d). The minimum and maximum device efficiencies at

the centre frequency of 60-GHz for the excited input ports one and three are 46.6% and 54.8%, respectively. The lens is bent under the extreme flexure as well, in order to examine the performance of the BFN under this condition. Fig. 5 (e) indicates the flexural structure under the extreme bending, in which it is bent around a cylinder with the radius of R_2. Fig. 5 (f) presents the output in terms of the surface currents, which depicts the efficient distribution across the output array ports. The EM range indicates the intensities throughout the component. This scale has been set for the other flexures as well (i.e., Figs. 2, 3, and 4), in order to deploy a uniform EM range among the proposed 60-GHz flexures.

The RL device efficiency for this extreme case, in which only input beam port three is excited for the exertion of the maximum efficiency, is computed as 53.1%. The RLs have confirmed the maintenance of the RF output performance for the exploit of the wideband mm-wave operation. Hence, the flexible devices are promising solutions in order to effectively facilitate the deployment of the RF beam steering and to rank the deficient conventional services in the microwave infrastructures [79–84]. They exhibit significant features, as the multi-environmental electronic beam-switching cores, for the conformal platforms at the network AP level with the interconnecting links, in order to improve the overall performance and coverage. Furthermore, the output characteristics of the device, as the high-performance fixed-weight mm-wave beamformer, incorporate the intrinsic segments of the beam scanning functionality to apply the constant weights (i.e., the amplitude and phase) to the individual array elements to steer the main beam toward the desired signal angle direction [85–89].

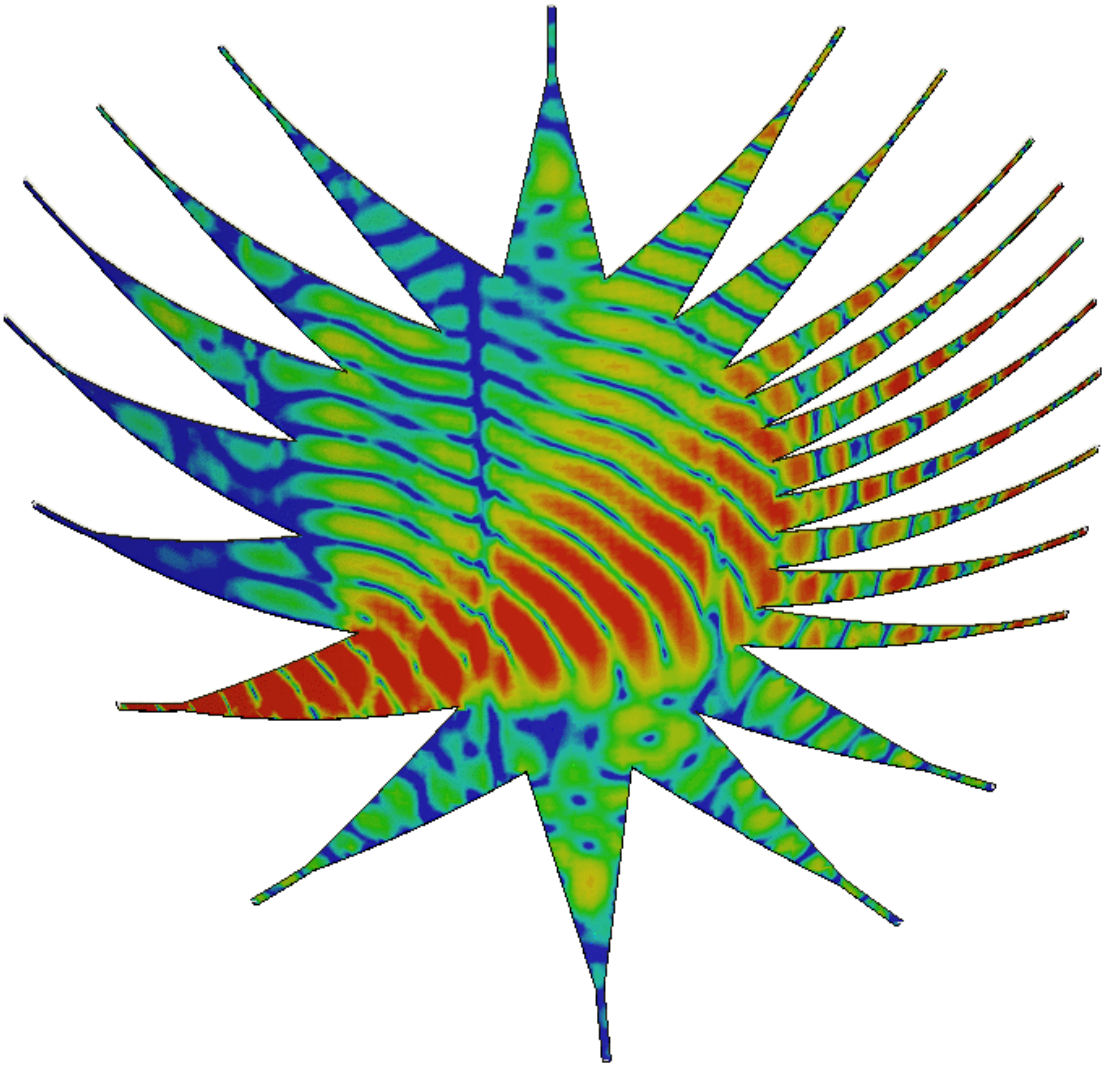

(a)

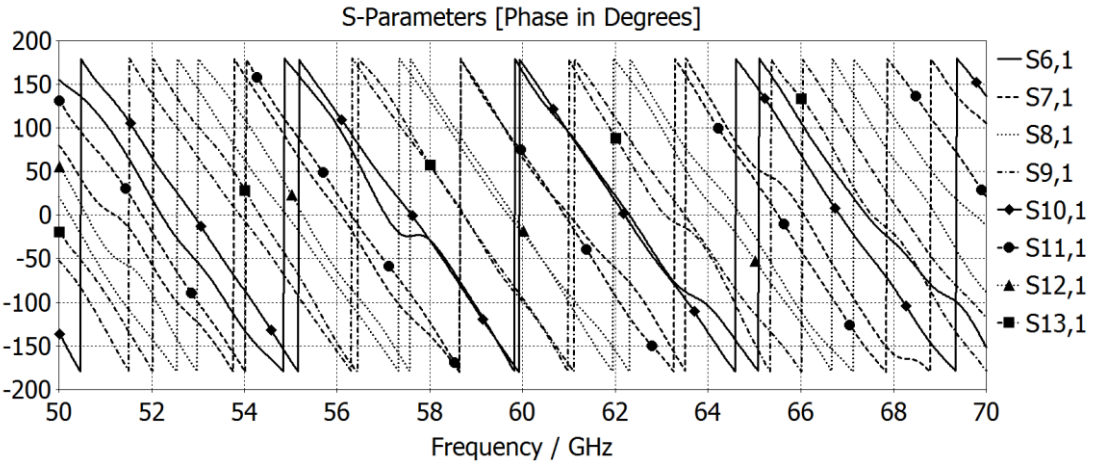
S-Parameters [Phase in Degrees]
200
150
100
50
0
-50
-100
-150
-200
50
52
54
56
58
60
62
64
66
68
70
Frequency / GHz
S6,1
S7,1
S8,1
S9,1
S10,1
S11,1
S12,1
S13,1

(b)

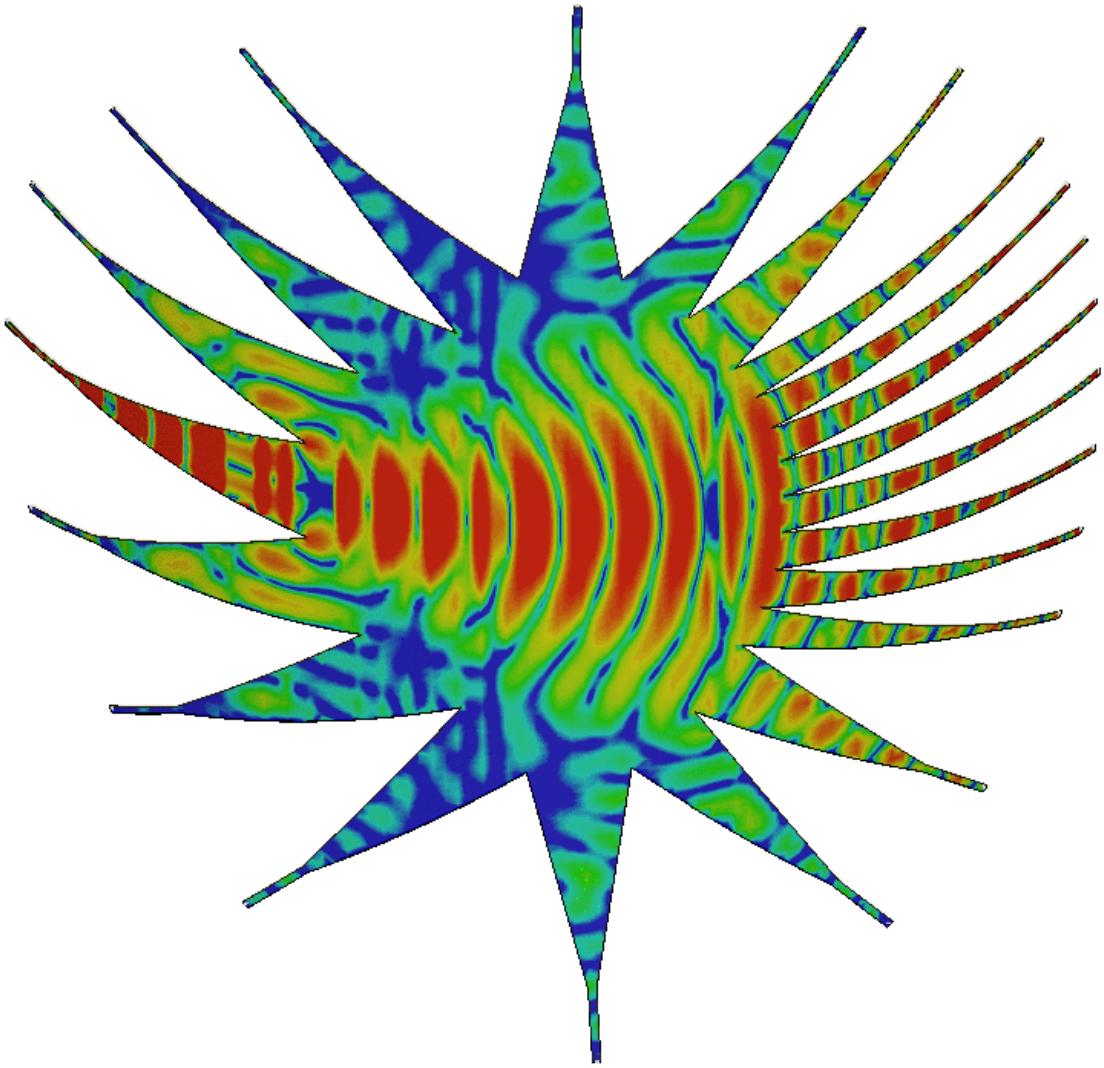

(c)

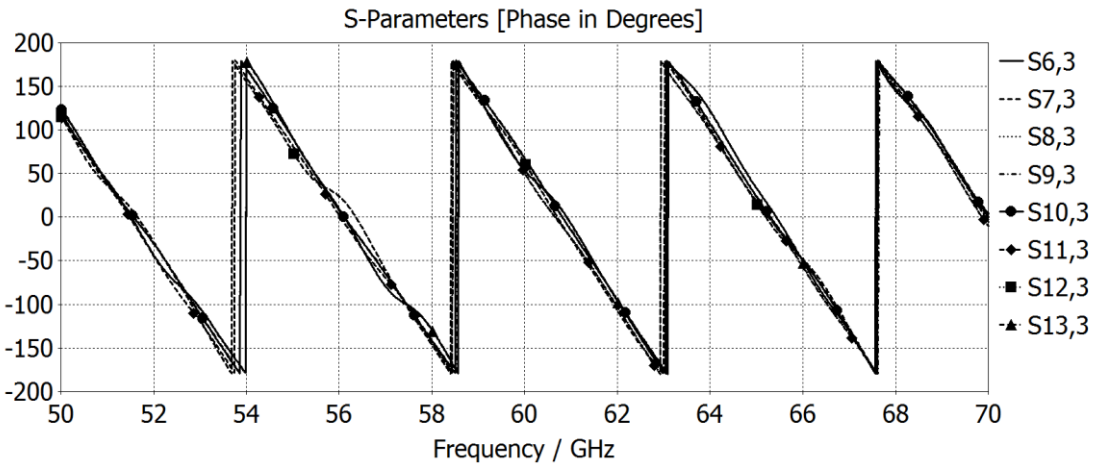
S-Parameters [Phase in Degrees]
200
150
100
50
0
-50
-100
-150
-200
50
52
54
56
58
60
62
64
66
68
70
Frequency / GHz
S6,3
S7,3
S8,3
S9,3
S10,3
S11,3
S12,3
S13,3

(d)

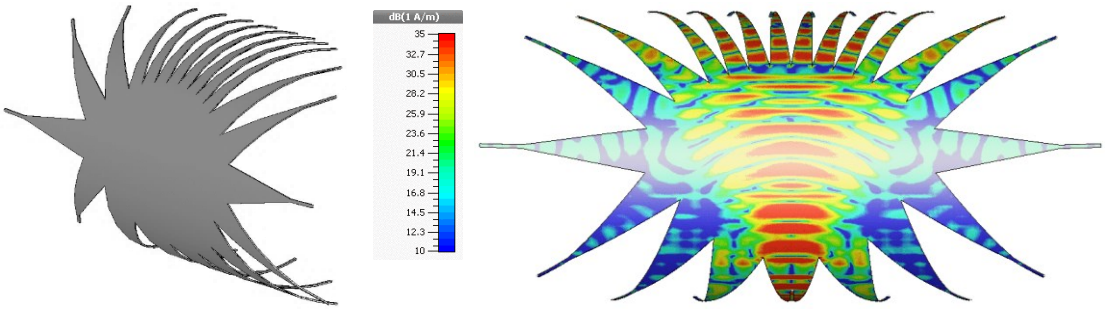

(e) (f)

Fig. 4.5. RF performance characteristics of the 60-GHz LCP-based RL based on the flexural case of the convex-circumferential bending, in which the device is bent around cylinders of radiuses R_1 = 20 mm and R_2 = 10 mm: (a) surface currents for the excited input beam port 1; (b) linear progressive phase behaviour for the excited beam port 1; (c) surface currents for the excited input beam port 3; (d) linear progressive phase behaviour for the excited input beam port 3; (e) extreme flexural structure of the developed RL; (f) surface current distributions for the excited central beam port 3 under the extreme condition of the convex-circumferential bending.

4.7 Conformal 28-GHz 5×8 RL Based on the Flexural Case-IV

The advanced smart antenna technologies, developed based on the emerging mm-wave switched-beam networks, provide the advanced UDN infrastructures with the essential requirements, for the purpose of optimal operation and propagation based on the RF front-end antenna array systems. Employment of these electronic systems consequently results in the improvement of the overall network performance, which is further evaluated in terms of the improved SNR, which increases the achievable information capacity and throughput, and thus expediting the required Gbps data

transmission rate among the AP radio links. This can be achieved through effectively combining the generated directional, narrow, and high-gain beams to increase the array gain in the direction of interest (i.e., to enhance the coverage and to maximise the signal strength), as well as to realise the spatial diversity as the RF signal moves throughout the sector. The latter is also based on minimising the multipath fading by deploying the electronic beam steering functionality toward the desired RF signal and further steering a null toward an interfering one. In this regard, Figs. 6 and 7 thoroughly present the RF output characteristics of the designed wideband 28-GHz RL-BFN, which has been also bent under the introduced flexural case-IV. The output characteristics obtained as a result of this conformal bending can be utilised in the development of the advanced integrated mm-wave modules for the next-generation flexible and conformal wireless subsystems [90–96]. The presented results can be extended into the evaluation of the RL based on the inclusion of the error estimation, in terms of the margin of error, and the error sources using the numerical analysis, in order to determine the upper- and lower-boundaries of the device efficiency.

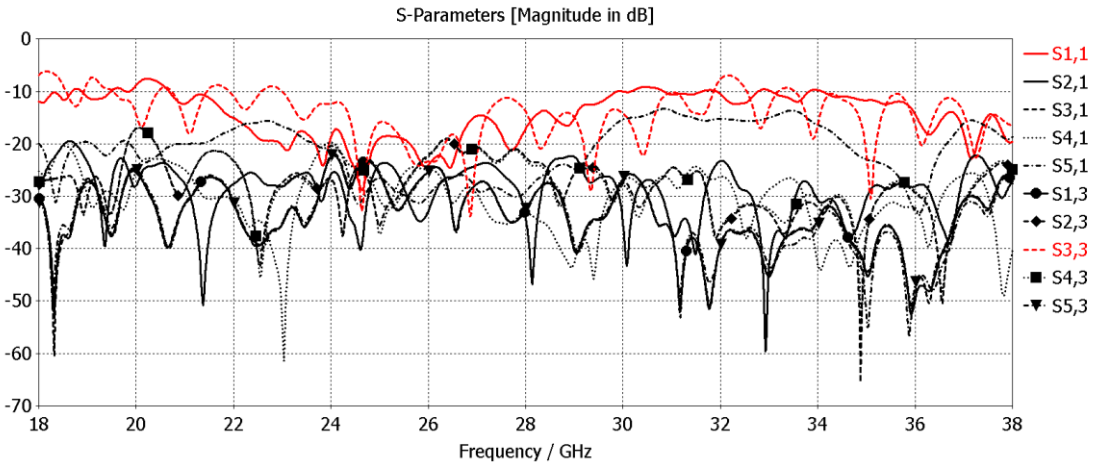

(a)

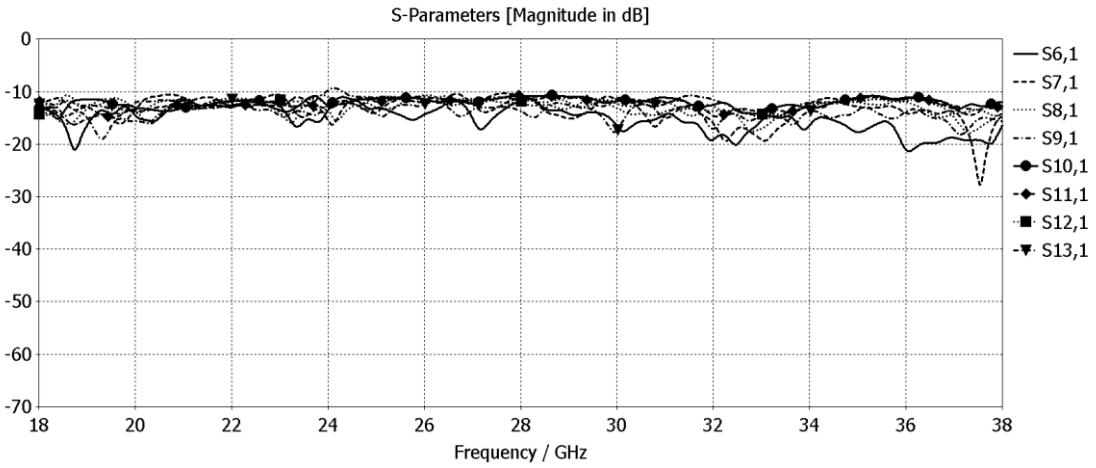

(b)

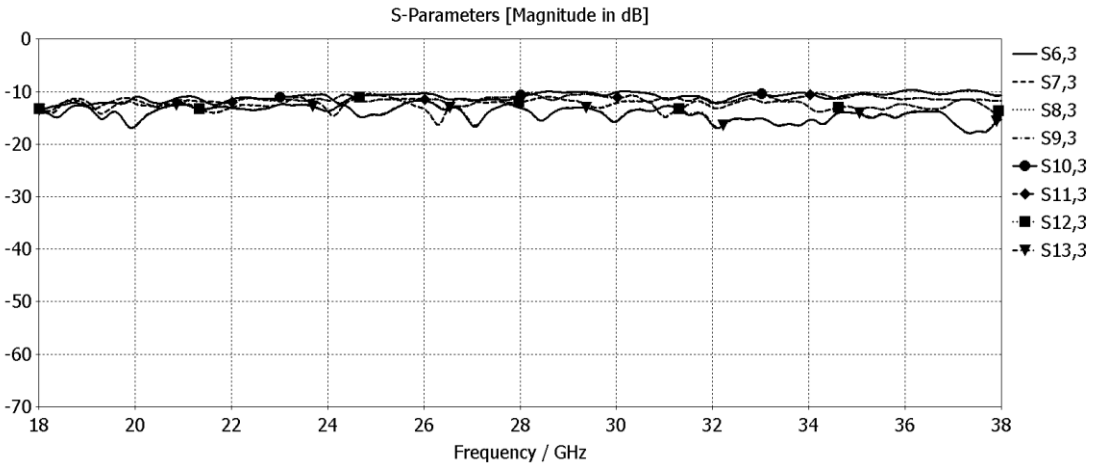

(c)

Fig. 4.6. Simulated *S*-parameters of the developed LCP-based wideband 28-GHz 5 × 8 RL based on the proposed flexural case of the convex-circumferential bending, in which the lens device is bent around cylinders of radius R = 60 mm: (a) reflection coefficient plots, as well as isolation plots for input beam ports 1 and 3 active; (b) transmission coefficient plots for beam port 1 active; (c) transmission coefficient plots for beam port 3 active.

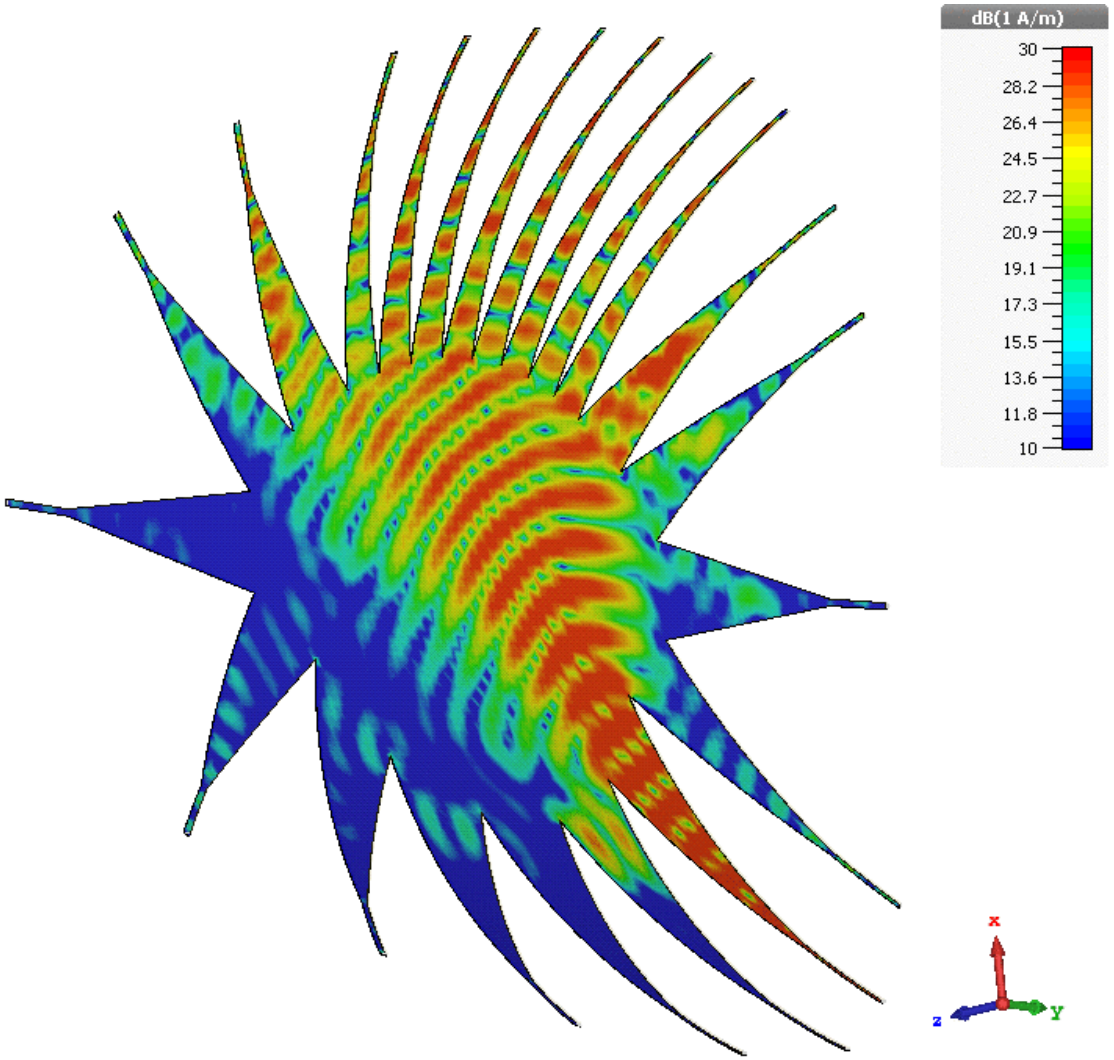
dB(1 A/m)
30
28.2
26.4
24.5
22.7
20.9
19.1
17.3
15.5
13.6
11.8
10
x
y
z

(a)

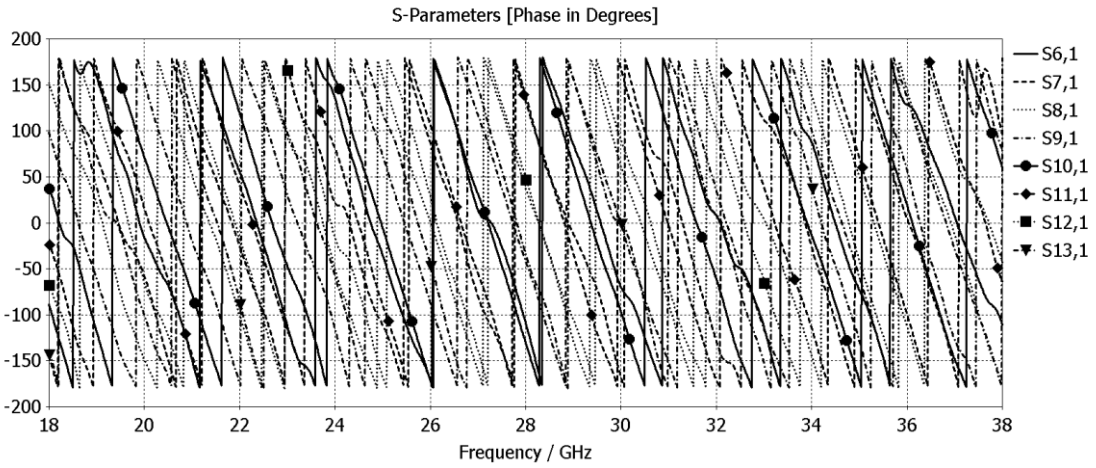
S-Parameters [Phase in Degrees]
200
150
100
50
0
-50
-100
-150
-200
18
20
22
24
26
28
30
32
34
36
38
Frequency / GHz
S6,1
S7,1
S8,1
S9,1
S10,1
S11,1
S12,1
S13,1

(b)

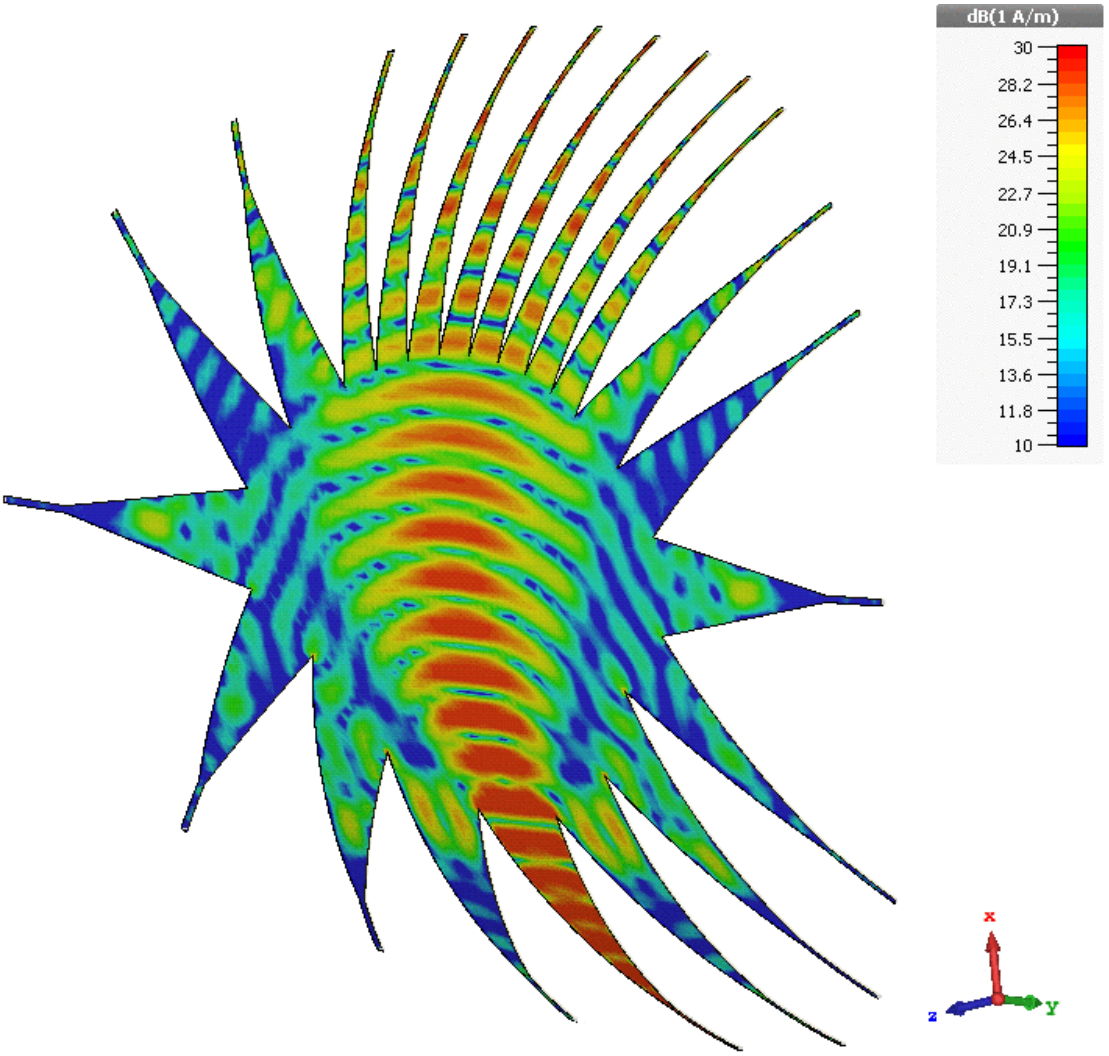
dB(1 A/m)
30
28.2
26.4
24.5
22.7
20.9
19.1
17.3
15.5
13.6
11.8
10
x
y
z

(c)

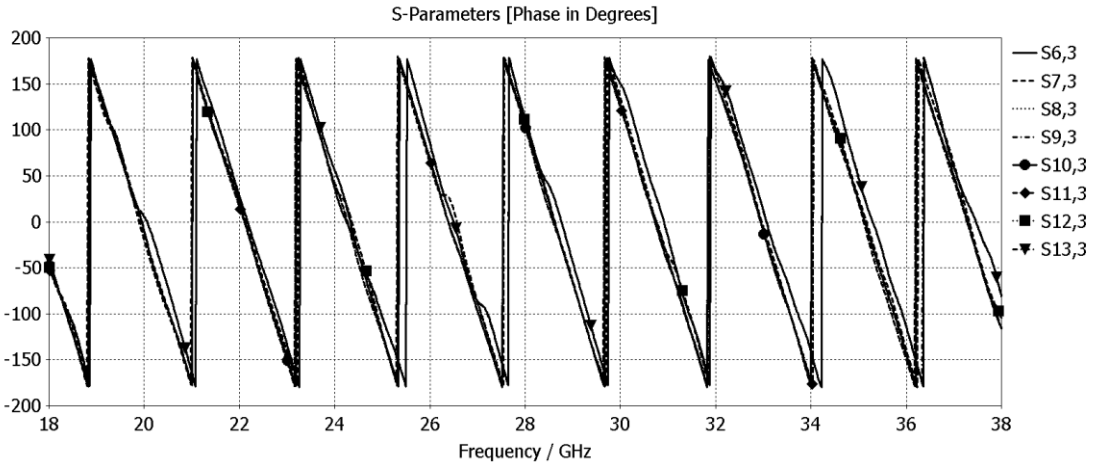
S-Parameters [Phase in Degrees]
200
150
100
50
0
-50
-100
-150
-200
18
20
22
24
26
28
30
32
34
36
38
Frequency / GHz
S6,3
S7,3
S8,3
S9,3
S10,3
S11,3
S12,3
S13,3

(d)

Fig. 4.7. Output characteristics of the developed LCP-based 28-GHz RL for the wideband operation, based on the flexural case of the convex-circumferential bending, in which the lens is bent around a cylinder of radius R = 60 mm: (a) surface current distributions for the excited input beam port 1, exerting the minimum device efficiency of 56.7%; (b) linear phase behaviour for the excited input beam port 1; (c) surface current distributions for the excited central input beam port 3, exerting the maximum device efficiency of 58.2%; (d) linear phase behaviour for the excited central input beam port 3.

In order to experimentally validate the HPC-based full-wave EM simulation results of the developed RL-BFN for the flexural case of the convex-circumferential bending, the fabricated LCP-based 28-GHz RL has been employed to appropriately conduct the mm-wave beamforming, and to be measured for the evaluation of the RF output performances in the conformal case. Hence, a setup has been accurately deployed in order for the RL-BFN to be properly placed for the measurement process using the VNA. The fabricated RL has been then bent around a cylinder of radius R = 60 mm, and the measurement has been effectively carried out to obtain the magnitude and phase characteristics of the BFN over the intended frequency band (i.e., Figs. 8 and 9). As already mentioned, the fabrication of the lens has been carried out using the LPKF ProtoLaser U4 laser-based circuit structuring technique to maintain the high-resolution realisation required for the high-performance, and to further minimise the fabrication errors and non-uniformity of the TLs, in comparison with the other RF circuit implementation methods. This has been thoroughly conducted, in order to maintain the output performance of the realised lens device, in terms of the main requirements for the RF electronic beam steering in the advanced wireless systems.

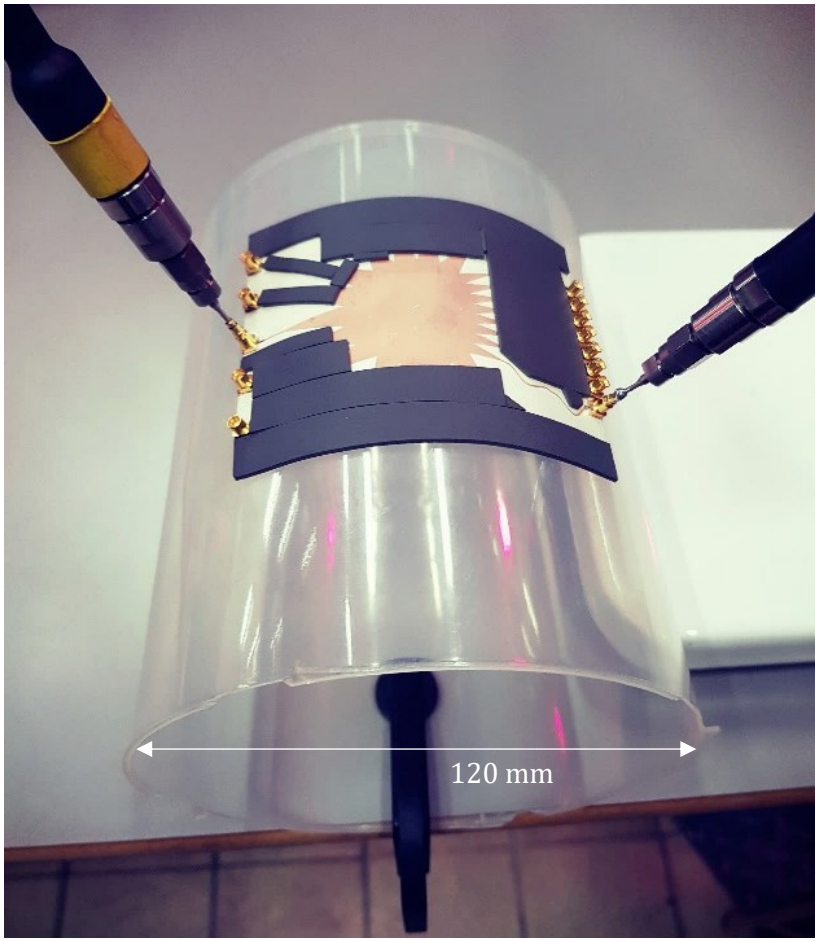

Fig. 4.8. Experimental conformal 28-GHz beamforming using the fabricated RL-BFN.

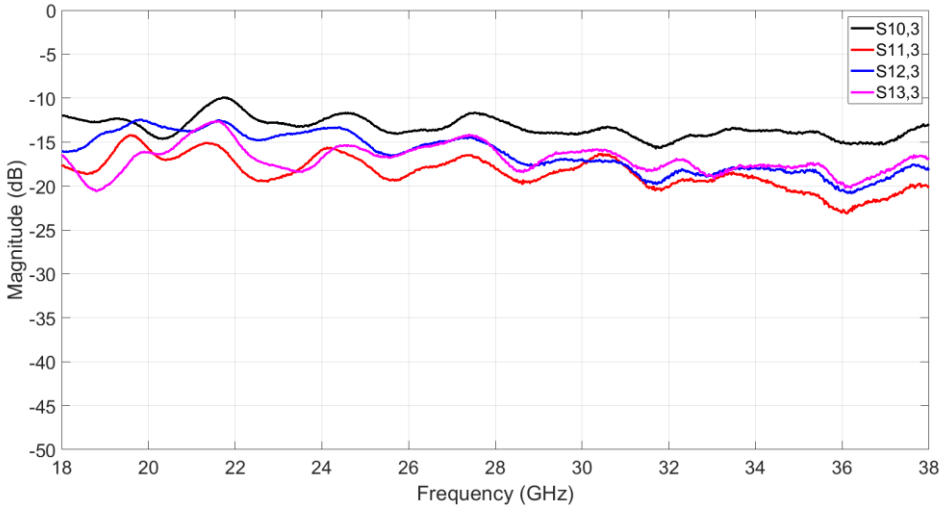

(a)

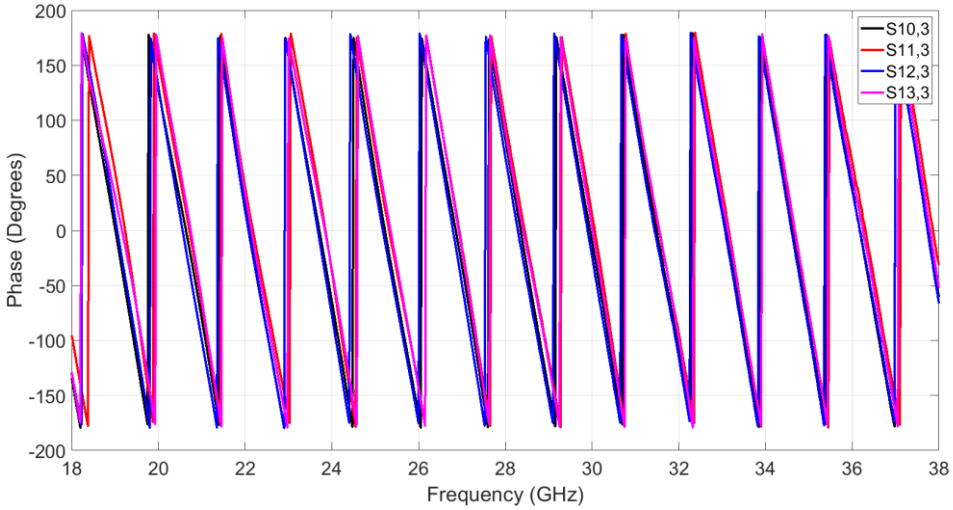

(b)

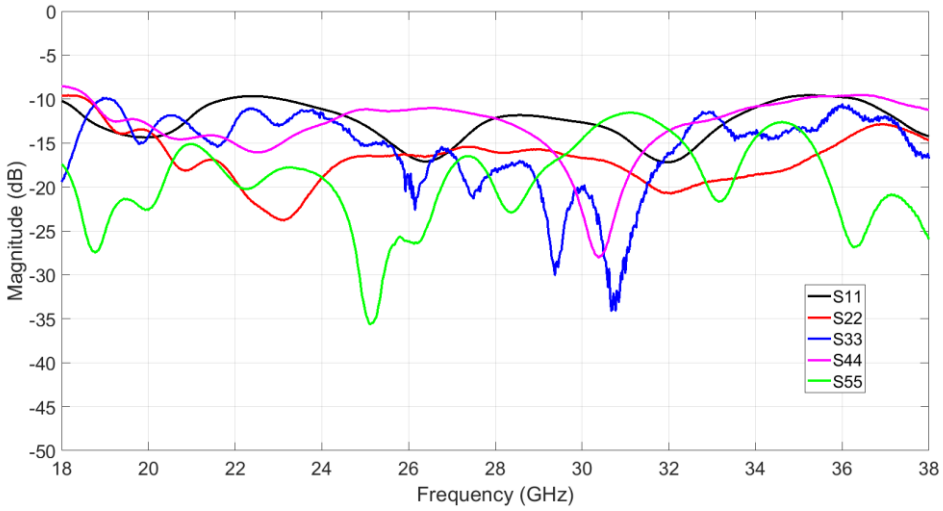

(c)

Fig. 4.9. Measured *S*-parameters of the conformal LCP-based 28-GHz RL for the wideband operation: (a) transmission coefficients for central input beam port 3 active; (b) linear progressive phase distribution plots for port 3 active; (c) reflection coefficients. It should be noted that the measured results are in a good agreement with the simulated results throughout the operating band; the slight deviation in the magnitude levels are due to the errors and mismatches caused by the cables, SMPM adapters, connectors, and soldering.

Fig. 10 (a) presents the computed AF plots based on the measured data for both the planar and conformal cases, for the excited beam ports one and three, along with 4 output ports utilised, due to the RL symmetry. It shows that the formed beams are steered toward the desired directions with the minimum phase error. In addition, the AFs, shown in Fig. 10 (b) and (c), have been further compared with the simulated and theoretical ones for the planar lens case, while exhibiting wider scanning beams.

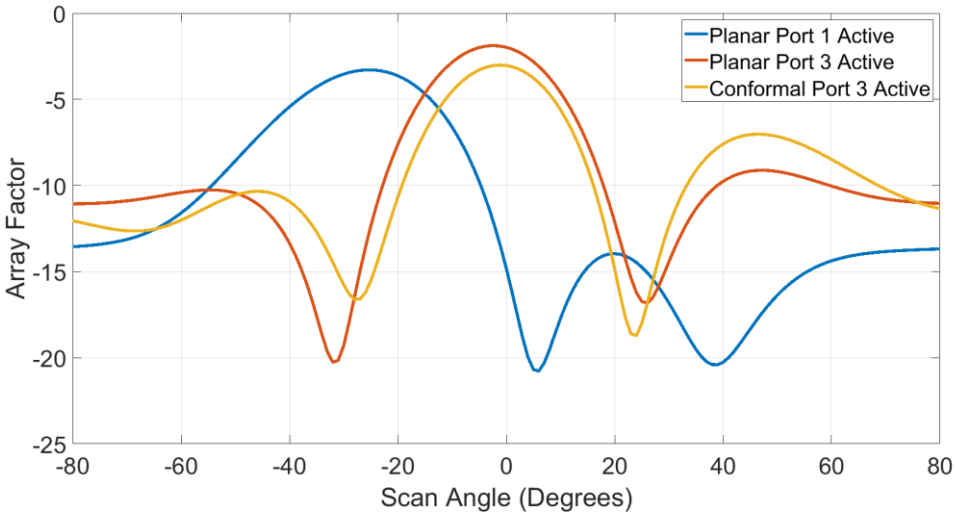

(a)

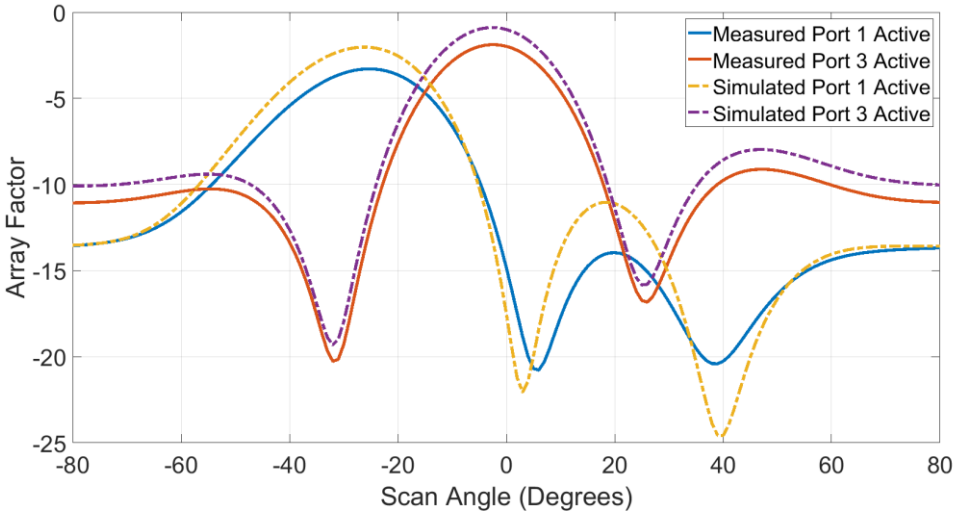

(b)

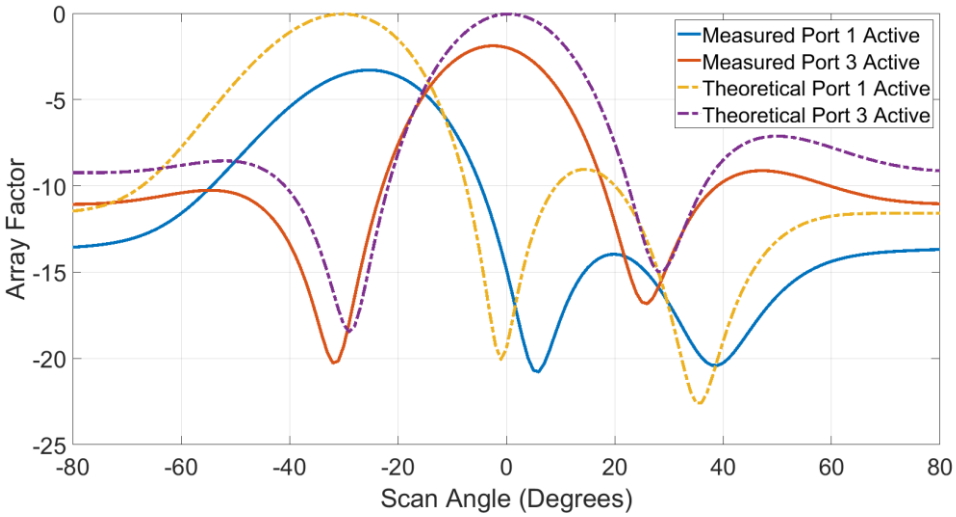

(c)

Fig. 4.10. Computed AF plots of the 5×8 RL for beam ports 1 and 3 active: (a) the measured case; (b) the measured and simulated cases; (c) the measured and theoretical cases.

In addition, as Fig. 11 presents, a set of AFs for the developed 7 × 10 28-GHz BFN has been generated, in order to depict the RF electronic beam scanning performance for the simulated planar case, for the excited input beam ports one and central four.

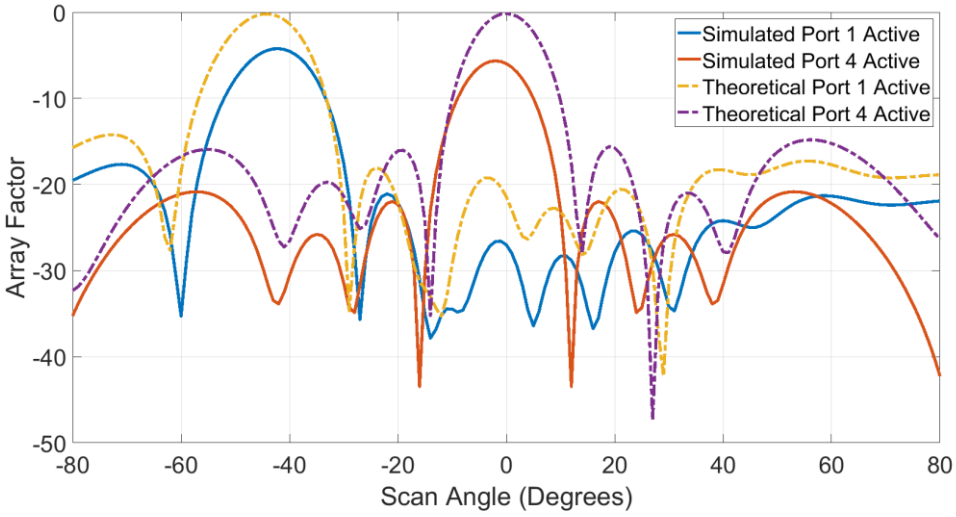

Fig. 4.11. Computed AF plots of the 7 × 10 28-GHz RL-BFN for beam ports 1 and 4 active.

4.8 Summary

This chapter presented the design, analysis, and performance evaluation of the 60- and 28-GHz RL-BFNs based on the employed LCP substrate, along with conducting the experimental feasibility analysis of the mm-wave beamforming for the potential deployment in the flexible and conformal electronic applications. The RF designs for the proposed flexures, including the concave-axial bending, convex-axial bending, concave-circumferential bending, and convex-circumferential bending, have been comprehensively carried out, and the output performances in terms of the flexural structure, surface current distributions, linear phase behaviour required for the RF electronic beam steering, and device efficiencies, have been presented in detail. The flexibility analysis can be potentially extended into the case of system performance evaluation under the crumpling deformation condition (i.e., the combination of the proposed flexural cases). Moreover, the investigation of the spillover loss reduction mechanisms can also be carried out to decrease the sidewall reflections within the lens cavity, and to further increase the device efficiency, for the implementation of the intended site-specific subsystems based on the RF beamforming techniques.

In addition, a number of AF plots for the developed RL-BFNs (i.e., 5 × 8 and 7 × 10) have been generated, in order to examine the performance and functionality of these formed beams for the potential antenna elements. The AF plots have been generated based on the measured and simulate data, for both the planar and conformal cases. Moreover, their output characterises have been thoroughly compared against their respective theoretical plots to assess the deficiencies and beam scanning behaviour, as in the ideal case, the phase error does not exist, unlike the real scanning scenarios.

Chapter 5:

Modelling and RF Performance Evaluation of Large-Scale 28-GHz Rotman Lens-Fed Array BFNs for Next-Generation Wireless Communication Subsystems

5.1 Introduction

The constituent equations of the trifocal RLs have been effectively utilised, in order to undertake the design of the extended RF structures based on the presented LCP-based 28-GHz RL. This section shows the conducted high-performance simulations regarding the comprehensive representation of the RF output characteristics of the developed RLs, designed specifically to serve as efficient passive feeding networks for the large-scale antenna systems, as part of the next-generation infrastructures.

5.2 Large-Scale Design and Evaluation: The 28-GHz 11×22 RL-BFN

Fig. 1 presents the designed large-scale mm-wave lens-based BFN for operation in the 18–38 GHz frequency band, with the switched-beam scanning coverage of ±30˚.

The RL has been fully developed based on the Rogers ULTRALAM LCP laminate with the dielectric constant of ε_r = 2.9, loss tangent of tanδ = 0.0025, substrate thickness of h = 0.18 mm, and top- and bottom-cladding of t = 17.5 μm. Figs. 2 and 3 provide the HPC-based full-wave simulations of the developed large-scale RL, and the output characteristics based on the S-parameters are discussed in the following sections.

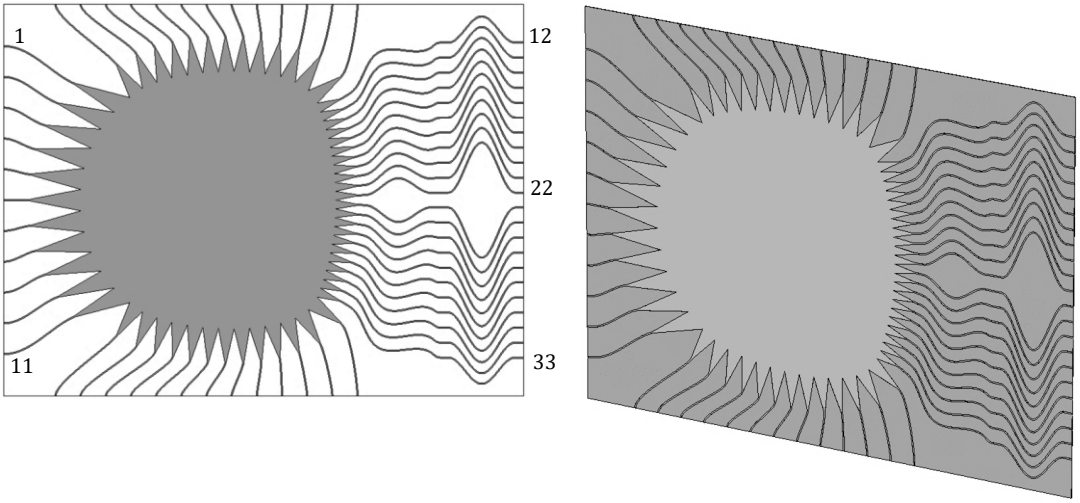

(a) (b)

Fig. 5.1. LCP-based wideband 28-GHz BFN: (a) large-scale RL with 11 input beam ports, 22 output array ports, and 26 dummy ports, with the dimensions of 139.97 × 185.86 mm^2, front view; (b) perspective view.

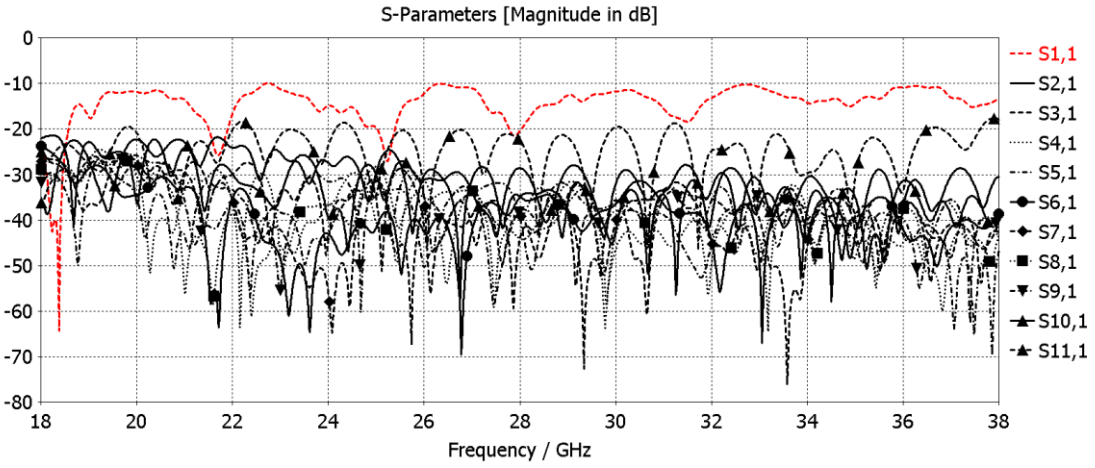

(a)

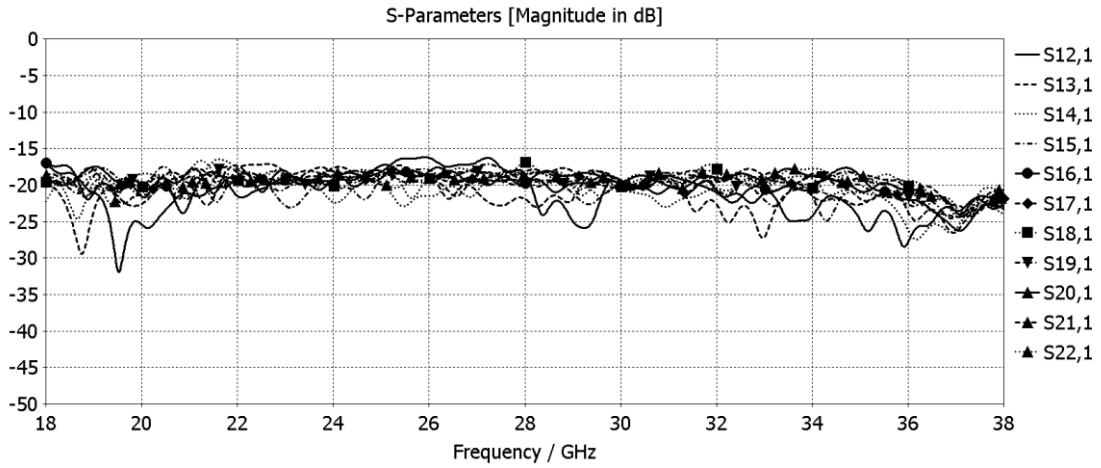

(b)

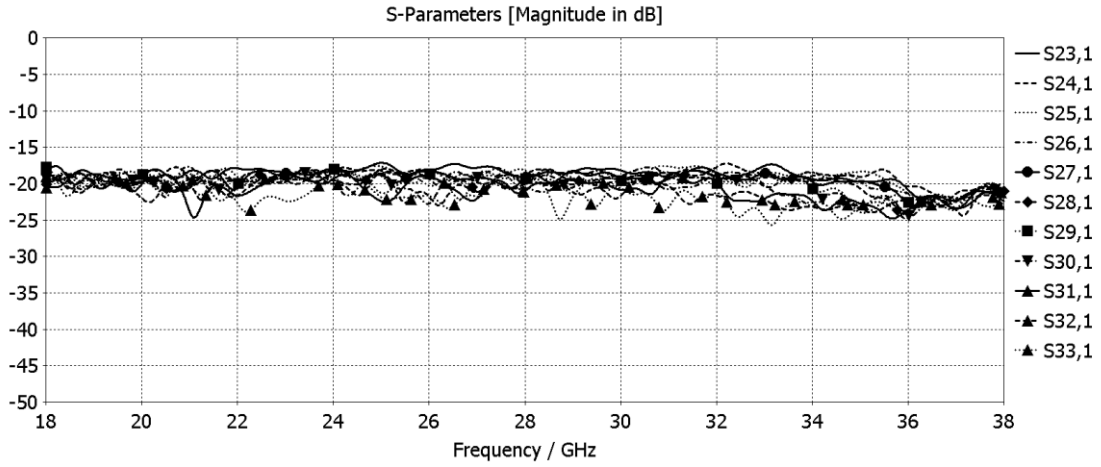

(c)

Fig. 5.2. Simulated *S*-parameters and output characteristics of the developed LCP-based wideband large-scale RL-BFN: (a) reflection coefficient and isolation plots for the excited input beam port 1; (b) transmission coefficient plots for input beam port 1 active, Set I (i.e., output array ports 12 to 22); (c) transmission coefficient plots for input beam port 1 active, Set II (i.e., output array ports 23 to 33).

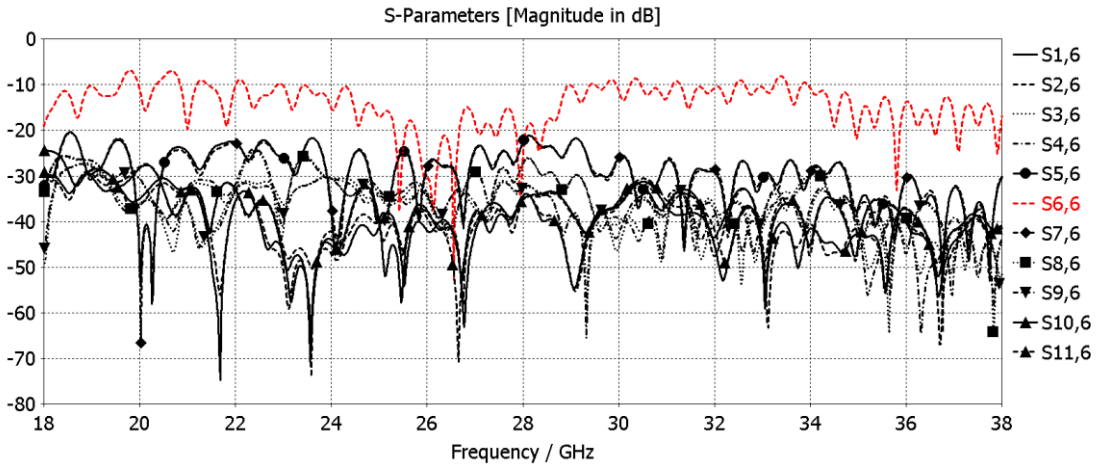
S-Parameters [Magnitude in dB]
0
-10
-20
-30
-40
-50
-60
-70
-80
18
20
22
24
26
28
30
32
34
36
38
Frequency / GHz
S1,6
S2,6
S3,6
S4,6
S5,6
S6,6
S7,6
S8,6
S9,6
S10,6
S11,6

(a)

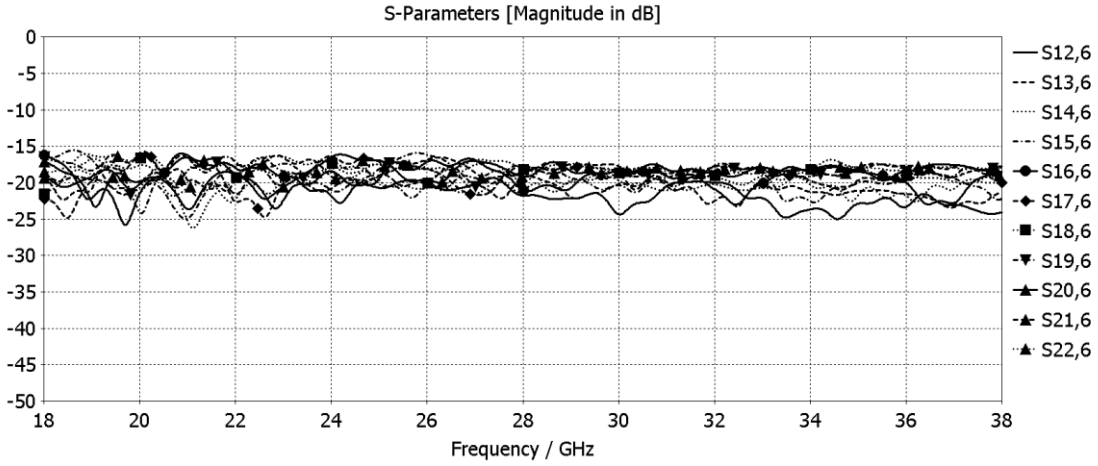
S-Parameters [Magnitude in dB]
0
-5
-10
-15
-20
-25
-30
-35
-40
-45
-50
18
20
22
24
26
28
30
32
34
36
38
Frequency / GHz
S12,6
S13,6
S14,6
S15,6
S16,6
S17,6
S18,6
S19,6
S20,6
S21,6
S22,6

(b)

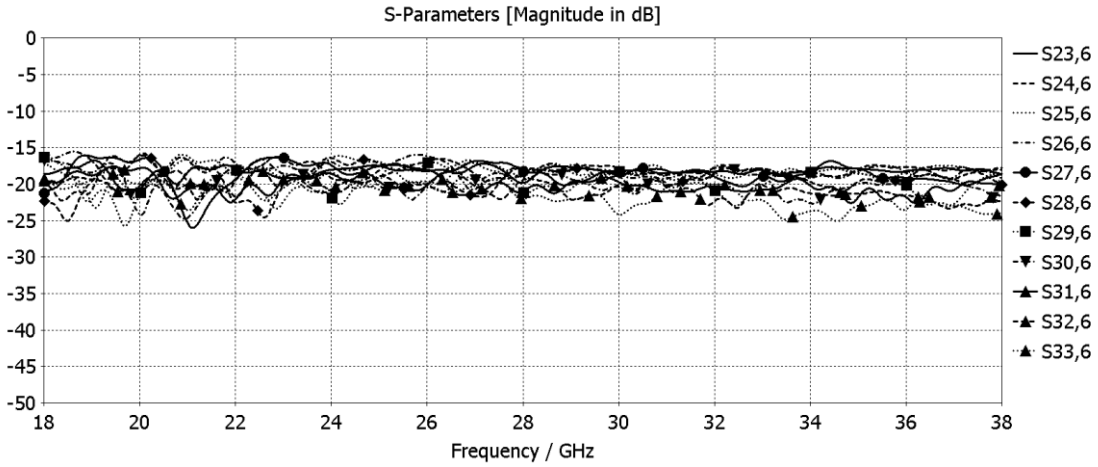
S-Parameters [Magnitude in dB]
0
-5
-10
-15
-20
-25
-30
-35
-40
-45
-50
18
20
22
24
26
28
30
32
34
36
38
Frequency / GHz
S23,6
S24,6
S25,6
S26,6
S27,6
S28,6
S29,6
S30,6
S31,6
S32,6
S33,6

(c)

Fig. 5.3. Simulated *S*-parameters and output characteristics of the developed LCP-based wideband large-scale RL-BFN: (a) reflection coefficient and isolation plots for the excited central beam port 6; (b) transmission coefficient plots for central beam port 6 active, Set I (i.e., output array ports 12 to 22); (c) transmission coefficient plots for central input beam port 6 active, Set II (i.e., output array ports 23 to 33).

Figs. 2 (a) and 3 (a) thoroughly present the reflection coefficient and isolation plots for the excited input beam ports one and six, respectively. The output results depict the desired RF behaviour of the planar LCP-based large-scale RL-BFN, in terms of maintaining the distributed power levels over the whole mm-wave frequency range of operation. Moreover, Figs. 2 (b) and (c) and Figs. 3 (b) and (c) clearly present the transmission coefficients for the activated beam ports one and six, respectively. As it can be observed from the comprehensive full-wave simulations, the large-scale RL feeding network exhibits the linear distributions of the power with the low-ripple RF profiles, across the operating frequency range of 18–38 GHz, over the whole set of array ports 12 to 33 (i.e., 22 output array ports); hence, confirming the wideband operation of the lens. These originally exploited RF characteristics of the developed large-scale RL can be effectively utilised in the future massive MIMO systems for the next-generation wireless communication architectures, to effectively overcome the imperfect ambient conditions in the mm-wave channels.

Furthermore, Figs. 4 (a) and (b) extensively illustrate the phase division behaviour of the large-scale BFN, when the input beam ports one and six are fed, respectively. It is worth noting that input beam ports one and six determine the boundaries of the minimum and maximum RF device efficiencies, since they are placed on the furthest

distance from the central focal point of the lens device, as well as on the central axis of the RL-BFN, respectively. The computed device efficiency at the centre frequency of 28-GHz is also obtained as 26.5%. The presented plots indicate the linear phase distributions across the output array ports of the large-scale RL-BFN; i.e., depicted in two different sets for beam ports one and six, for a clear representation; hence, substantially meeting the primary requirements of the electronic beam steering, for the efficient deployment of the mm-wave subsystems. The proposed large-scale BFN can be potentially employed as a powerful core of the communication system, in a number of intelligent wireless communication applications. The developed lens is able to provide the system with the essential electronic beam steering capabilities, in the RF scenarios in which the appropriate implementation of a large number of antenna systems based on the digital beamforming methods, as well as the circuit-based beamforming systems with higher device efficiencies, is enormously complex, costly, power consuming, lossy, bulky, and inflexible. The proposed RLs can hence provide the next-generation subsystems with high-performance alternatives.

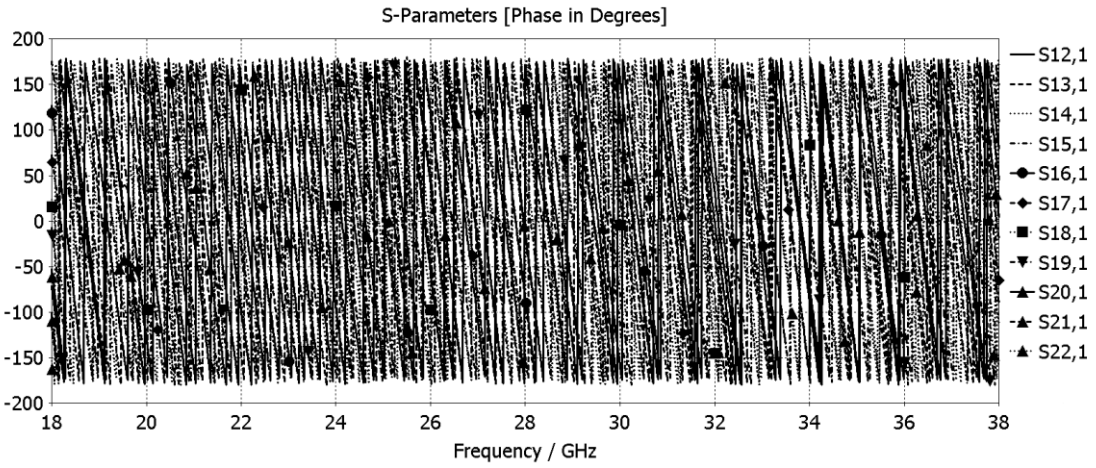

(a)

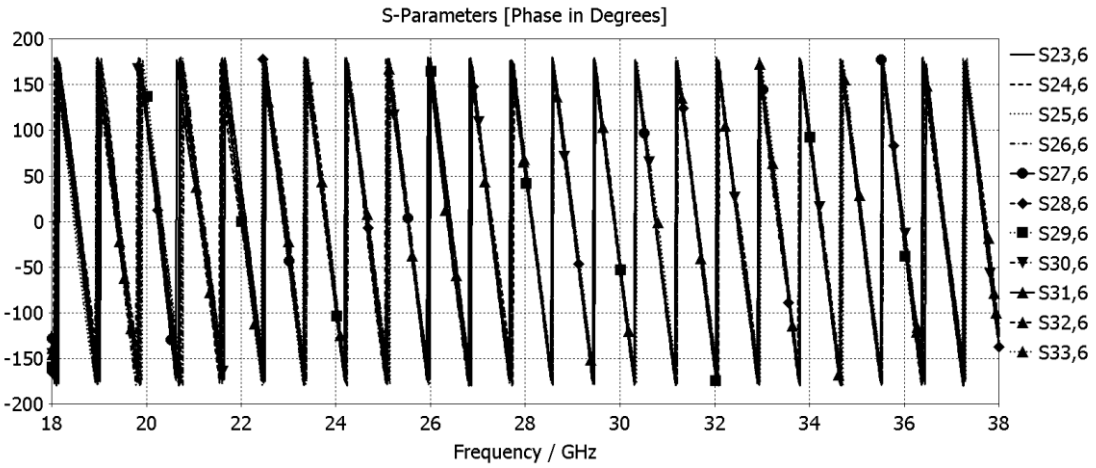

(b)

Fig. 5.4. Simulated *S*-parameters and output characteristics of the developed LCP-based wideband large-scale RL-BFN: (a) linear progressive phase distributions for beam port 1 active, Set I (i.e., output array ports 12 to 22); (b) linear progressive phase distributions for central input beam port 6 active, Set II (i.e., output array ports 23 to 33).

Figs. 5 (a) to (f) thoroughly present the surface current distributions of the designed planar LCP-based large-scale RL at the centre frequency, for the activated ports one to six, respectively. This high-resolution full-wave representation clearly illustrates the behaviour of the EM wave, while travelling within the lens cavity, starting from the excited input beam ports, then across the electrically-large lens structure, and further over the output array contour to efficiently distribute the EM energy among the array ports. It should be noted that the EM scale used in this representation of the surface currents is the same scale as the one for the developed 28-GHz 5 × 8 RL, i.e., Chapter 3, Fig. 5 (f). The surface currents confirm the high-performance of the lens device to be potentially utilised as a feeding in the large-scale MIMO systems.

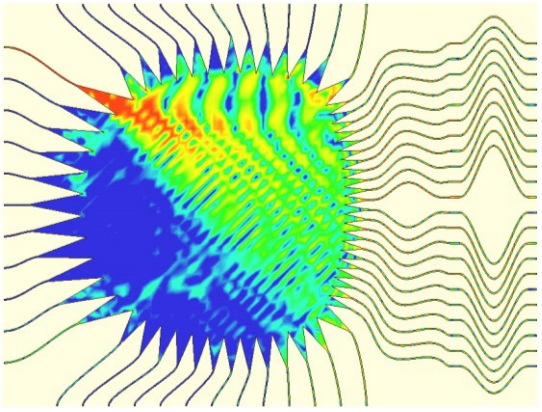

(a)

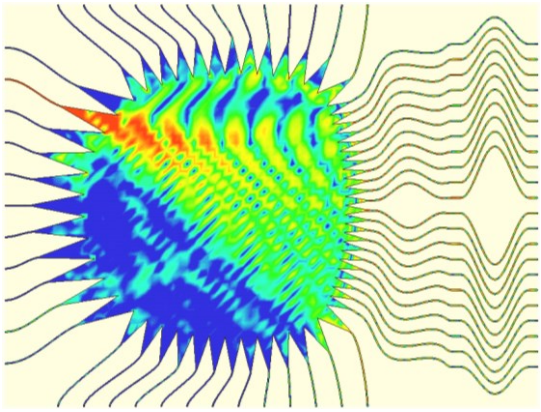

(b)

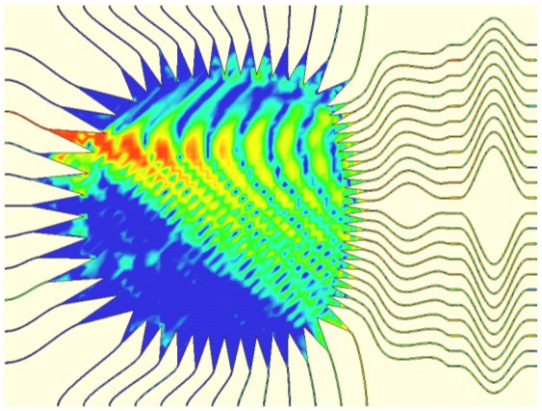

(c)

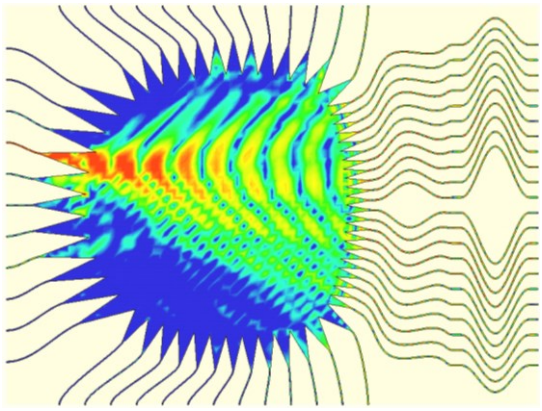

(d)

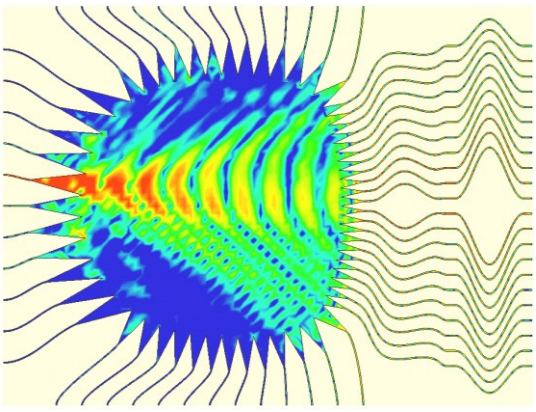

(e)

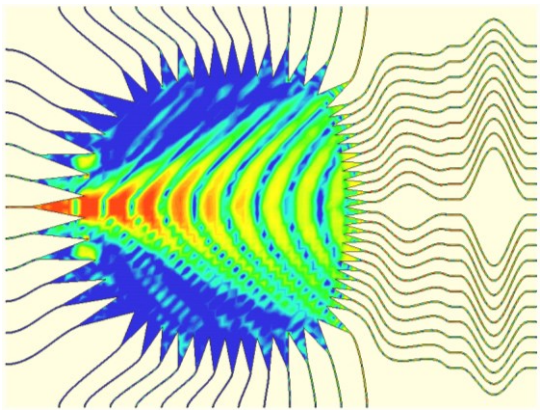

(f)

Fig. 5.5. Surface current distributions of the LCP-based large-scale 11 × 22 BFN, for the excited input beam ports at mm-wave centre frequency f = 28-GHz: (a) input beam port 1 active; (b) input beam port 2 active; (c) input beam port 3 active; (d) input beam port 4 active; (e) input beam port 5 active; (f) central input beam port 6 active.

5.3 Large-Scale Design: The 32- and 64-Element RL-BFNs

The presented LCP-based 11 × 22 RL has been extended into two other large-scale RF structures, as shown in Figs. 6 to 8 (i.e., representing the RL structures, surface current distributions, and linear phase outputs, respectively) to appropriately feed the 32- and 64-element phased array systems. The RLs have been developed based on the trifocal constituent equations, which are effectively used to design these LCP-based RLs. The inherent mechanism of these RL-BFNs to appropriately perform the electronic beam scanning, is also based on equalising the electrical path from a beam port to an output array port across the large-scale antenna array contour, with the time-delay of the corresponding planar wavefront from a given far-field direction; consequently resulting in the RF beam generation in the corresponding direction.

In order to efficiently deploy the intelligent wireless communications, the advanced RF beamformers, as the dominant component of most multibeam antenna systems, as well as the core of the hybrid RF networks, are able to significantly improve the performance of the mm-wave wireless transceivers. This is achieved by maintaining the consistent characteristics, improving the throughput and data rate of the system, and accommodating the directional transmissions. As thoroughly presented in this work, these compact and lightweight RL-BFNs offer cost-effective solutions for the

scenarios in which a large number of antenna elements are of crucial importance to steer the direction of the main lobe of the radiation, to compensate the path loss, and to realise the reliable communication links. This is currently deployed based on the costly and high power consumption methods using the conventional MIMO systems with separate chains and digital units, along with complex signal processing. Hence, the developed RL-BFNs precisely enable the desired distributions of amplitude and phase coefficients, to properly excite a corresponding number of array elements for the electronically steerable beam scanning, thereby facilitating a higher EIRP in the transmit (Tx) mode, as well as an improved SNR in the receive (RX) mode, as part of the implementation of the next-generation mm-wave wireless transceivers.

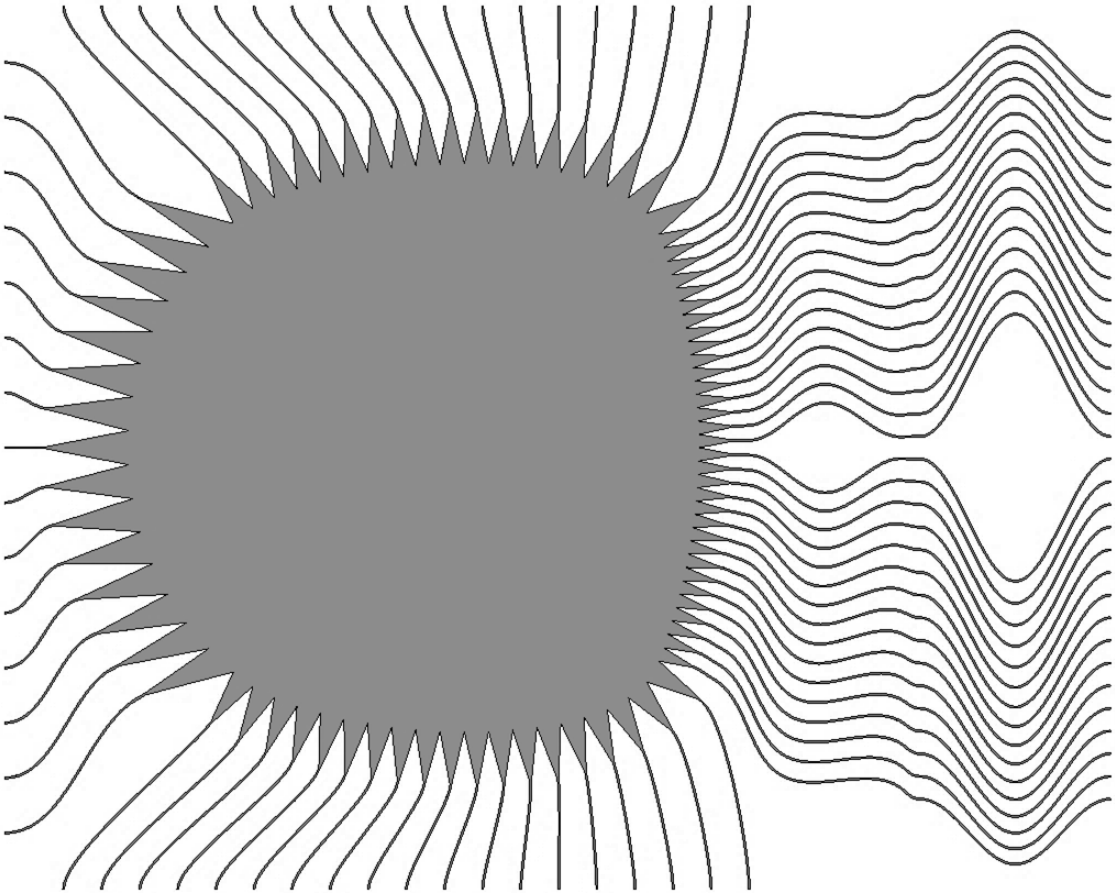

(a)

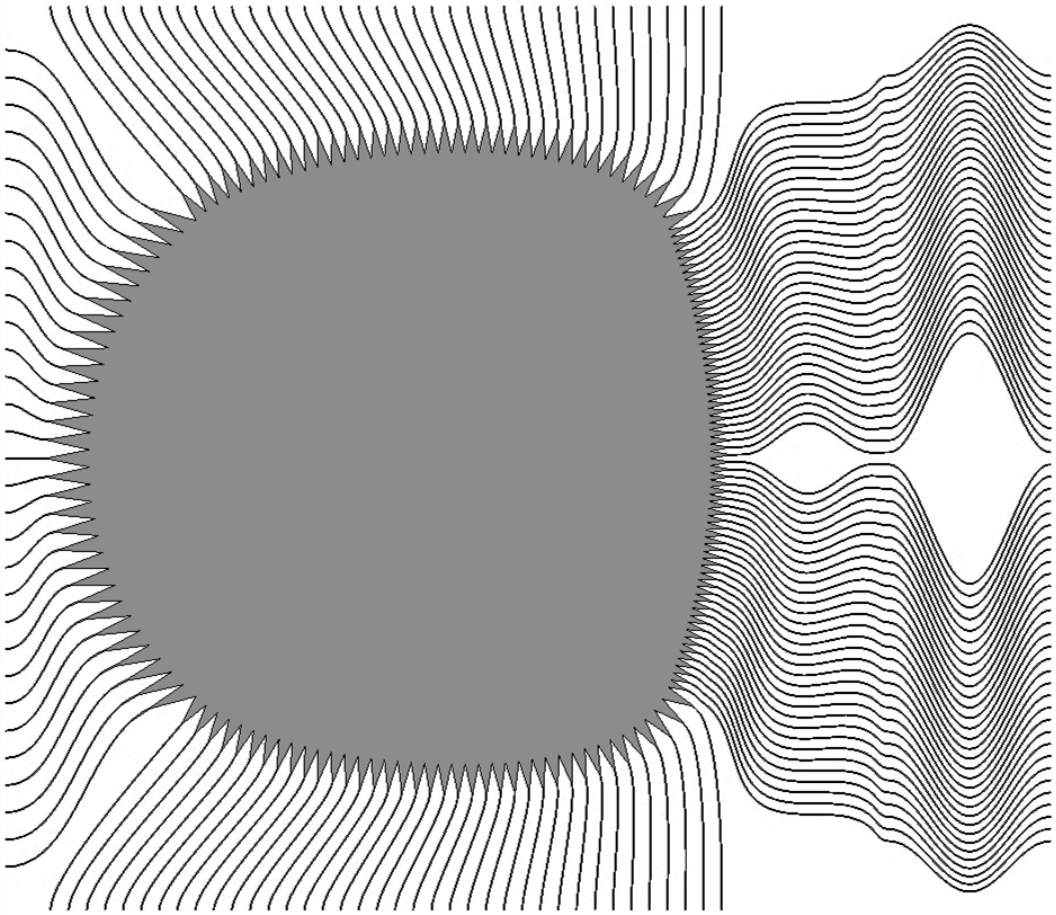

(b)

Fig. 5.6. Large-scale RLs: (a) RL with 15 beam ports, 32 array ports, and 38 dummy ports, with the dimensions of 208.49 × 261.20 mm^2; (b) RL with 31 beam ports, 64 array ports, and 76 dummy ports, with the dimensions of 398.23 × 460.64 mm^2.

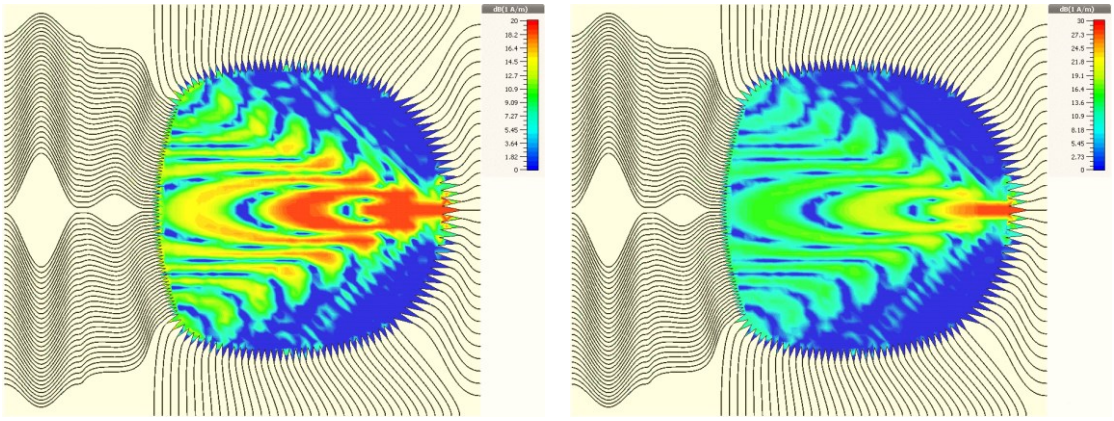

(a) (b)

Fig. 5.7. Surface current distributions of the LCP-based wideband large-scale 31 × 64 RL for the excited central beam port 16 at mm-wave centre frequency f = 28-GHz: (a) surface currents based on the scaling case-I; (b) surface current based on the scaling case-II.

Hence, as Fig. 8 presents, the developed large-scale RL is able to maintain the linear progressive phase distributions across the output contour, which can be effectively utilised as the high-performance front-end to theoretically implement a full massive MIMO testbed with 64 array elements capable of generating 31 directional links for the RF electronic beam steering in the next-generation wireless subsystems.

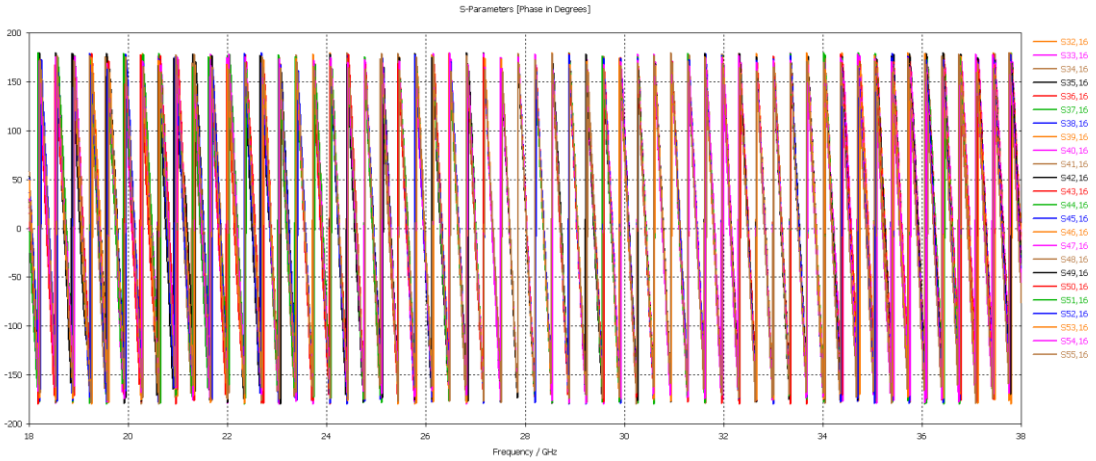

(a)

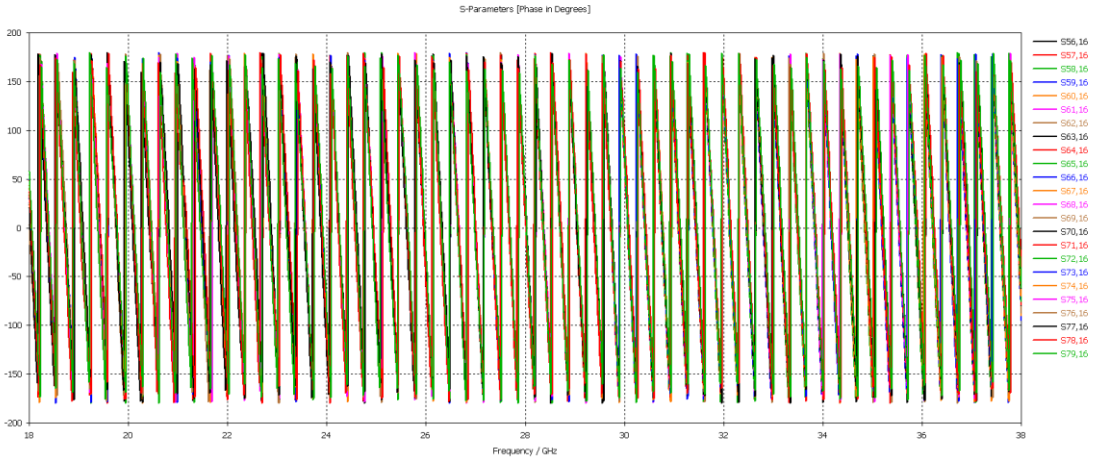

(b)

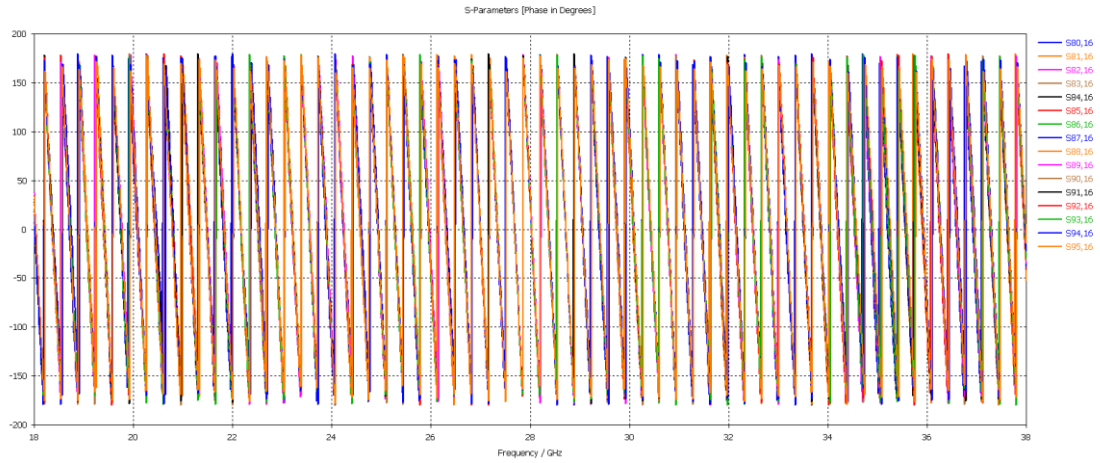

(c)

Fig. 5.8. Linear progressive phase distributions of the developed LCP-based wideband large-scale 28-GHz 31 × 64 RL for the excited central input beam port 16: (a) Set I (i.e., output array ports 32 to 55); (b) Set II (i.e., output array ports 56 to 79); (c) Set III (i.e., output array ports 80 to 95).

5.4 Summary

This chapter has thoroughly undertaken the design and performance evaluations of the mm-wave large-scale RL-BFNs, based on the HPC-based full-wave simulations. The presented results confirm the high-performance operation of the RLs, in terms of exhibiting significant output characteristics, including the linear and low-ripple amplitude distributions across the output array ports, progressive phase division, wideband operation of the RLs with the minimised phase error, and efficient surface current distributions over the output array contours. The proposed RLs include the LCP-based large-scale 11 × 22, 15 × 32, and 31 × 64 array RL-BFNs, realised based

on the original trifocal constituent design equations, and further optimised in terms of the intrinsic parameters' functionalities, for the operating frequency of 28-GHz.

This investigation can also be extended into the evaluations of the large-scale BFNs for the conformal systems. The LCP-based RLs have the remarkable potential to be utilised in the conformal wireless communication systems. Therefore, this thorough RF performance analysis can be extended into the case of introducing the proposed flexures into the structures of the designed large-scale RL-BFNs. This would lead to the appropriate feasibility study of implementing such flexible large-scale networks, according to the aerodynamic and hydrodynamic properties of the bearing surfaces, as well as the configurations of the intended wireless system infrastructures. Hence, the core of this conducted design and performance analysis can also be considered as a generalised RF design framework for the optimal numerical evaluations of the BFNs for the next-generation wireless communication systems and applications.

Chapter 6:

Conclusion and Future Work

6.1 Concluding Remarks

This thesis has undertaken complete design and performance analysis of mm-wave array beamforming networks, based on the Rotman lens-fed concept. The primary objective of this work has been to develop a number of novel, flexible, efficient, high-performance, and low-profile lens-fed mm-wave RF beamformers based on the LCP substrates. This has been comprehensively performed for the potential employment in the next-generation millimetre-wave wireless communications. Furthermore, the deployed methods for the development of these array beamforming networks, along with the specific approaches for the representation of the RF output characteristics, have been intended to be proposed as the generalised frameworks for the optimal implementation of these types of RF passive switched-beam subsystems. Moreover, this work has covered a number of solutions and experimental evaluations for the practical implementations of the conformal and flexible subsystems that are able to conduct the RF beam steering for the advanced communication infrastructures.

In this regard, and for the sake of brevity, this section hereby overviews the key contributions of this work in the area of mm-wave lens-based array beamformers:

- Providing an original wireless communications-centric perspective over the next-generation communication systems, as well as the important role of the RF beamforming systems, as the primary means of directional transmissions at the AP levels, to maintain the high-performance of the networks.
- Numerical design and performance evaluation of a low-profile and wideband LCP-based planar 28-GHz 5 × 8 RL-BFN, for operation in the 18–38 GHz band.
- Numerical design and performance evaluation of a low-profile and wideband LCP-based planar 28-GHz 7 × 10 BFN, for operation in the 18–38 GHz band.
- Numerical design and performance evaluation of a low-profile and wideband LCP-based planar 60-GHz 5 × 8 RL-BFN, for operation in the 50–70 GHz band.
- Analytical design and numerical performance evaluation of a low-profile and wideband LCP-based planar 28-GHz 11 × 22 large-scale RL-fed beamformer, for operation in the 18–38 GHz band.
- Analytical design and numerical performance evaluation of a low-profile and wideband LCP-based planar 28-GHz 31 × 64 large-scale RL-fed beamformer, for operation in the 18–38 GHz band.
- Analytical design and numerical performance evaluation of a low-profile and wideband LCP-based conformal 28-GHz 5 × 8 RL-fed array beamformer, for operation in the 18–38 GHz band.
- Analytical design and numerical performance evaluation of low-profile and wideband LCP-based flexible 60-GHz 5 × 8 RL-fed array beamformers, for operation in the 50–70 GHz band.

- Experimental design and measured performance evaluation of a low-profile and wideband LCP-based planar 28-GHz 5 × 8 RL-fed array beamformer, for the high-performance operation in the 18–38 GHz frequency band.
- Experimental design and measured performance evaluation of a low-profile and wideband LCP-based conformal 28-GHz 5 × 8 RL-fed array beamformer, for the high-performance operation in the 18–38 GHz band.

6.2 Future Work

This work can be further extended into a number of other RF scenarios, as follows:

- Fabrication and measured performance analysis of the flexible 60-GHz RL.
- Experimental mm-wave array beamforming based on the developed large-scale RL-BFNs for the next-generation communications and massive MIMO.
- Implementation of the proposed array subsystems using the inkjet printing method, along with the comparative performance evaluations of the RLs.
- Incorporation of the EM techniques; e.g., the transformation optics (TO); for introducing the enhancements, such as size reduction and miniaturisation, in the structures of the RLs, along with the RF output performance evaluations.
- Feasibility analysis of the realised conformal 28-GHz RL to be deployed as a six-port junction component for the next-generation RF homodyne receivers.

Appendix A:

Microwave Absorbing Material Characterisation

A.1 Results and Discussion

The thin and flexible microwave absorbing material (i.e., ECCOSORB FGM-40) has been effectively employed for the measurement process. The material has been used for terminating the RL ports, except the two ones under the test. This novel method has been proposed for the lens device to introduce an additional degree of freedom (DoF) for the circuits and systems integration at the RF transceiver level, to reduce the complexity and overhead of the measurement process, and to reduce the cost of the subsystem implementation at the mm-wave frequency bands. As Fig. A. 1 shows, the absorber is used as an efficient method for terminating the ports instead of using a large number of RF connectors and 50-Ω loads. Furthermore, in order to assess the performance of the wideband absorber at the intended band (i.e., 17–20 GHz), the material has been accurately characterized using the deployed setup based on the dielectric probe technique. Moreover, the obtained data have been further loaded into the designed LCP-based TL model, as also realized in the RL, in order to examine the RF performance of the microwave absorbing material, in terms of the effective attenuation and reflectivity in a desired wideband RF frequency domain.

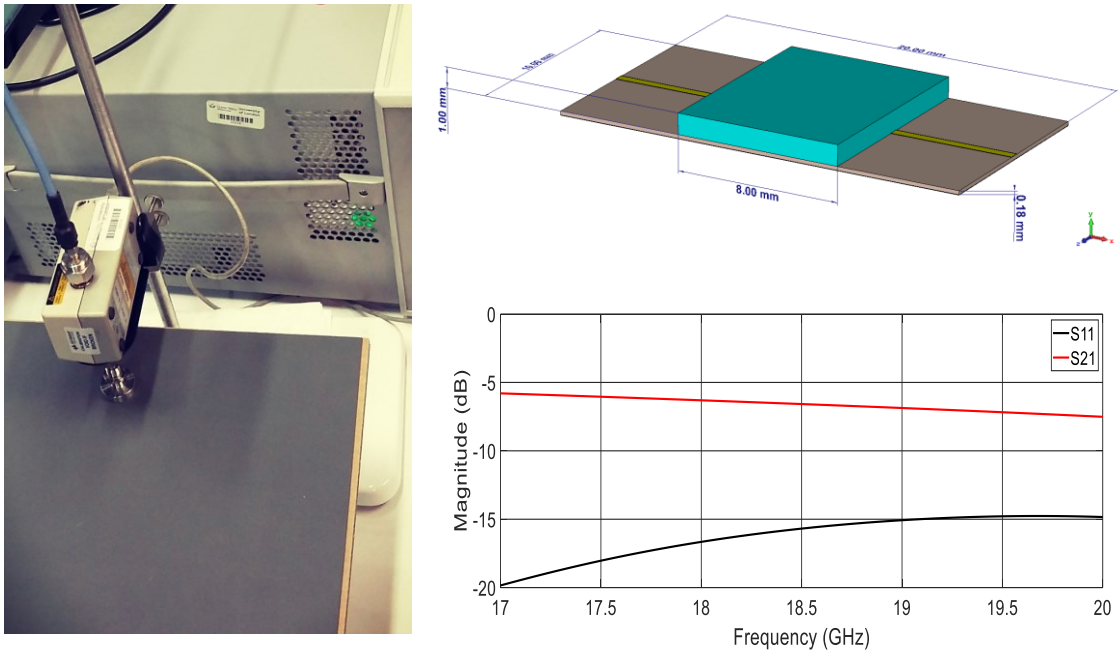

(a) (b)

Fig. A.1. Absorbing microwave material characterization: (a) deployed setup based on the dielectric probe technique for measuring the material properties; (b) simulated TL model loaded with the measured data (i.e., upper), and output characteristics (i.e., lower).

Appendix B:

Trifocal Rotman Lens-Based Array BFNs

B.1 Generalised Conceptual and Analytical Modelling

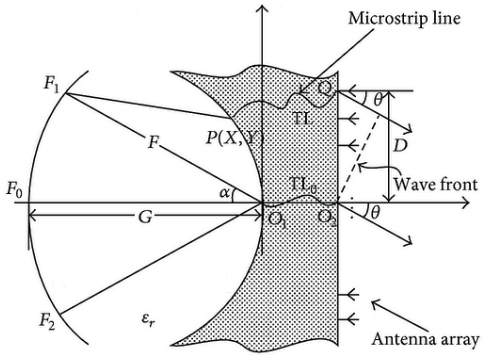

$$(F_1P)\sqrt{\varepsilon_{rc}} + W\sqrt{\varepsilon_{rt}} + D\sqrt{\varepsilon_{re}}\sin(\theta) = F\sqrt{\varepsilon_{rc}} + W_0\sqrt{\varepsilon_{rt}}; \tag{B.1}$$

$$(F_2P)\sqrt{\varepsilon_{rc}} + W\sqrt{\varepsilon_{rt}} - D\sqrt{\varepsilon_{re}}\sin(\theta) = F\sqrt{\varepsilon_{rc}} + W_0\sqrt{\varepsilon_{rt}}; \tag{B.2}$$

$$(F_0P)\sqrt{\varepsilon_{rc}} + W\sqrt{\varepsilon_{rt}} = G\sqrt{\varepsilon_{rc}} + W_0\sqrt{\varepsilon_{rt}}. \tag{B.3}$$

where

$$(F_1P)^2 = (-F\cos(\alpha) - X)^2 + (-F\sin(\alpha) + Y)^2 \tag{B.4}$$

$$= F^2 + X^2 + Y^2 + 2FX\cos(\alpha) - 2FY\sin(\alpha);$$

$$(F_2P)^2 = (-F\cos(\alpha) - X)^2 + (-F\sin(\alpha) - Y)^2 \tag{B.5}$$

$$= F^2 + X^2 + Y^2 + 2FX\cos(\alpha) + 2FY\sin(\alpha);$$

$$(F_0P)^2 = (G + X)^2 + Y^2. \tag{B.6}$$

Normalising equations (1)–(3) by the electrical length of the central focal length (i.e., $(G)\sqrt{\varepsilon_{rc}}$) results in equations (7)–(9). Moreover, w stands for the transmission path length difference ($W - W_0$), also normalised with respect to the central line length (i.e., G); β as the ratio of off-axis focal point length (i.e., F) to on-axis focal length G, is appropriately selected, in order to reduce the fundamental phase error in the lens.

$$\frac{(F_1P)}{G} = \frac{F}{G} - \frac{W - W_0}{G}\frac{\sqrt{\varepsilon_{rt}}}{\sqrt{\varepsilon_{rc}}} - \frac{D\sin(\theta)}{G}\frac{\sqrt{\varepsilon_{re}}}{\sqrt{\varepsilon_{rc}}} = \beta - w\frac{\sqrt{\varepsilon_{rt}}}{\sqrt{\varepsilon_{rc}}} - \frac{D\sin(\theta)}{G}\frac{\sqrt{\varepsilon_{re}}}{\sqrt{\varepsilon_{rc}}}; \tag{B.7}$$

$$\frac{(F_2P)}{G} = \frac{F}{G} - \frac{W - W_0}{G}\frac{\sqrt{\varepsilon_{rt}}}{\sqrt{\varepsilon_{rc}}} + \frac{D\sin(\theta)}{G}\frac{\sqrt{\varepsilon_{re}}}{\sqrt{\varepsilon_{rc}}} = \beta - w\frac{\sqrt{\varepsilon_{rt}}}{\sqrt{\varepsilon_{rc}}} + \frac{D\sin(\theta)}{G}\frac{\sqrt{\varepsilon_{re}}}{\sqrt{\varepsilon_{rc}}}; \tag{B.8}$$

$$\frac{(F_0P)}{G} = 1 - \frac{W - W_0}{G}\frac{\sqrt{\varepsilon_{rt}}}{\sqrt{\varepsilon_{rc}}} = 1 - w\frac{\sqrt{\varepsilon_{rt}}}{\sqrt{\varepsilon_{rc}}}. \tag{B.9}$$

By properly normalising (4)–(6) with respect to G, equations (10)–(12) are derived; x and y are also the normalised parameters of X and Y values with respect to G.

$$\begin{aligned}\frac{(F_1P)^2}{G^2} &= \frac{F^2}{G^2} + \frac{X^2}{G^2} + \frac{Y^2}{G^2} + 2\frac{FX\cos(\alpha)}{G^2} - 2\frac{FY\sin(\alpha)}{G^2} \\ &= \beta^2 + x^2 + y^2 + 2\beta x\cos(\alpha) - 2\beta y\sin(\alpha);\end{aligned} \tag{B.10}$$

$$\begin{aligned}\frac{(F_2P)^2}{G^2} &= \frac{F^2}{G^2} + \frac{X^2}{G^2} + \frac{Y^2}{G^2} + 2\frac{FX\cos(\alpha)}{G^2} + 2\frac{FY\sin(\alpha)}{G^2} \\ &= \beta^2 + x^2 + y^2 + 2\beta x\cos(\alpha) + 2\beta y\sin(\alpha);\end{aligned} \tag{B.11}$$

$$\frac{(F_0P)^2}{G^2} = \frac{(G+X)^2}{G^2} + \frac{Y^2}{G^2} = (1+x)^2 + y^2. \tag{B.12}$$

Squaring (7)–(9) and further equating with (10)–(12), result in equations (13)–(15).

$$\left(\beta - w\frac{\sqrt{\varepsilon_{rt}}}{\sqrt{\varepsilon_{rc}}} - \frac{D\sin(\theta)}{G}\frac{\sqrt{\varepsilon_{re}}}{\sqrt{\varepsilon_{rc}}}\right)^2$$

$$= \beta^2 + w^2\frac{\varepsilon_{rt}}{\varepsilon_{rc}} + \left(\frac{D\sin(\theta)}{G}\right)^2\frac{\varepsilon_{re}}{\varepsilon_{rc}} - 2\frac{\beta D\sin(\theta)}{G}\frac{\sqrt{\varepsilon_{re}}}{\sqrt{\varepsilon_{rc}}} + 2\frac{wD\sin(\theta)}{G}\frac{\sqrt{\varepsilon_{rt}\varepsilon_{re}}}{\varepsilon_{rc}}$$

$$- 2\beta w\frac{\sqrt{\varepsilon_{rt}}}{\sqrt{\varepsilon_{rc}}} = \beta^2 + x^2 + y^2 + 2\beta x\cos(\alpha) - 2\beta y\sin(\alpha);$$

$$\xrightarrow{\text{I}} w^2\frac{\varepsilon_{rt}}{\varepsilon_{rc}} + \left(\frac{D\sin(\theta)}{G}\right)^2\frac{\varepsilon_{re}}{\varepsilon_{rc}} - 2\beta w\frac{\sqrt{\varepsilon_{rt}\varepsilon_{re}}}{\varepsilon_{rc}} = x^2 + y^2 + 2\beta x\cos(\alpha). \tag{B.13}$$

$$\left(\beta - w\frac{\sqrt{\varepsilon_{rt}}}{\sqrt{\varepsilon_{rc}}} + \frac{D\sin(\theta)}{G}\frac{\sqrt{\varepsilon_{re}}}{\sqrt{\varepsilon_{rc}}}\right)^2$$

$$= \beta^2 + w^2\frac{\varepsilon_{rt}}{\varepsilon_{rc}} + \left(\frac{D\sin(\theta)}{G}\right)^2\frac{\varepsilon_{re}}{\varepsilon_{rc}} + 2\frac{\beta D\sin(\theta)}{G}\frac{\sqrt{\varepsilon_{re}}}{\sqrt{\varepsilon_{rc}}} - 2\frac{wD\sin(\theta)}{G}\frac{\sqrt{\varepsilon_{rt}\varepsilon_{re}}}{\varepsilon_{rc}}$$

$$- 2\beta w\frac{\sqrt{\varepsilon_{rt}}}{\sqrt{\varepsilon_{rc}}} = \beta^2 + x^2 + y^2 + 2\beta x\cos(\alpha) + 2\beta y\sin(\alpha);$$

$$\xrightarrow{\text{II}} \frac{\beta D\sin(\theta)}{G}\frac{\sqrt{\varepsilon_{re}}}{\sqrt{\varepsilon_{rc}}} - \frac{wD\sin(\theta)}{G}\frac{\sqrt{\varepsilon_{rt}\varepsilon_{re}}}{\varepsilon_{rc}} = \beta y\sin(\alpha). \tag{B.14}$$

$$\left(1 - w\frac{\sqrt{\varepsilon_{rt}}}{\sqrt{\varepsilon_{rc}}}\right)^2 = 1 - 2w\frac{\sqrt{\varepsilon_{rt}}}{\sqrt{\varepsilon_{rc}}} + w^2\frac{\varepsilon_{rt}}{\varepsilon_{rc}} = (1+x)^2 + y^2;$$

$$\xrightarrow{\text{III}} 2x + x^2 + y^2 = w^2\frac{\varepsilon_{rt}}{\varepsilon_{rc}} - 2w\frac{\sqrt{\varepsilon_{rt}}}{\sqrt{\varepsilon_{rc}}}. \tag{B.15}$$

The unknown parameters of the RL-BFN (i.e., X, Y, and $W - W_0$) are then solved from the above equations, as in equations (16)–(21).

$$\xrightarrow{\text{II}} y = \frac{D\sin(\theta)}{G\sin(\alpha)}\frac{\sqrt{\varepsilon_{re}}}{\sqrt{\varepsilon_{rc}}} - \frac{wD\sin(\theta)}{\beta G\sin(\alpha)}\frac{\sqrt{\varepsilon_{rt}\varepsilon_{re}}}{\varepsilon_{rc}}$$

$$= \frac{\boldsymbol{D\sin(\theta)}}{\boldsymbol{G\sin(\alpha)}}\frac{\sqrt{\varepsilon_{re}}}{\sqrt{\varepsilon_{rc}}}\left(1 - \frac{w}{\beta}\frac{\sqrt{\varepsilon_{rt}}}{\sqrt{\varepsilon_{rc}}}\right) = \boldsymbol{\eta}\frac{\sqrt{\varepsilon_{re}}}{\sqrt{\varepsilon_{rc}}}\left(1 - \frac{w}{\beta}\frac{\sqrt{\varepsilon_{rt}}}{\sqrt{\varepsilon_{rc}}}\right); \tag{B.16}$$

$$\xrightarrow{\text{I \& III}} x = \frac{\varepsilon_{re} d^2 (\sin(\theta))^2}{2\varepsilon_{rc}(\beta\cos(\alpha) - 1)} + \frac{(1-\beta)w}{\beta\cos(\alpha) - 1}\sqrt{\frac{\varepsilon_{rt}}{\varepsilon_{rc}}}; \tag{B.17}$$

$$\xrightarrow{yields} a\frac{\varepsilon_{rc}}{\varepsilon_{rt}}w^2 + b\sqrt{\frac{\varepsilon_{rc}}{\varepsilon_{rt}}}w + c = 0; w = \frac{\sqrt{\varepsilon_{rt}}}{\sqrt{\varepsilon_{rc}}}\frac{-b \pm \sqrt{b^2 - 4ac}}{2a}. \tag{B.18}$$

where

$$a = 1 - \left(\frac{1-\beta}{1-\beta\cos(\alpha)}\right)^2 - \left(\frac{\eta^2}{\beta^2}\frac{\varepsilon_{re}}{\varepsilon_{rc}}\right); \tag{B.19}$$

$$b = -2 + \left(\frac{2\eta^2}{\beta}\frac{\varepsilon_{re}}{\varepsilon_{rc}}\right) + \left(\frac{2(1-\beta)}{1-\beta\cos(\alpha)}\right) - \left(\frac{\eta^2 (\sin(\alpha))^2 (1-\beta)}{(1-\beta\cos(\alpha))^2}\frac{\varepsilon_{re}}{\varepsilon_{rc}}\right); \tag{B.20}$$

$$c = \left[-\eta^2 + \left(\frac{\eta^2 (\sin(\alpha))^2}{1-\beta\cos(\alpha)}\right) - \left(\frac{\eta^2 (\sin(\alpha))^4}{4(1-\beta\cos(\alpha))}\right)\right]\frac{\varepsilon_{re}}{\varepsilon_{rc}}. \tag{B.21}$$

According to the above formulations of the trifocal RL-BFNs, it can be summarised that in order to design the RF lens device, a number of steps have to be appropriately conducted, to determine a set of lens parameters regarding the physical, electrical, and TL properties of the RF device. Firstly, the PHY parameters should be taken into account that mainly include the following items: 1) the system impedance in ohms; 2) the medium to design the lens in, which affects the connecting TL structure and behaviour; 3) the shape of the beam port contour, i.e., the circular focal one; 4) the distance between the centre of the output array contour and the centre of the focal contour; 5) the ratio of on-axis focal length to off-axis focal length, to control the shape of the focal arc; 6) the dielectric parameters of the RF substrate, as well as the parameters affecting the metallisation of the lens. Secondly, the electrical properties of the lens device are considered, which mainly include: 1) the design frequency for which the geometry is scaled; 2) the operating range of frequency; 3) the spacing of

the linear array elements along the outer contour, to control how the energy would be distributed across the array aperture by each beam port; 4) the maximum angle the lens device would be used to scan over, i.e., the angle between the lens axis and the outermost beam port; 5) the ratio of the maximum to off-axis focal point angle; 6) the number of beam ports; 7) the maximum size a beam port can grow before it reduces to allow the insertion of a dummy port; 8) the taper angle, and the length of the tapered TLs; 9) the number of array elements; 10) the maximum size an array port can grow before it reduces to allow the insertion of a dummy port; 11) the rate or curvature for the upper-contour between the focal and array contours; 12) the maximum size a dummy port can grow before it reduces to allow the insertion of another dummy port. Thirdly, the TL properties are considered, in order to calculate the geometry for the bounding box of the lens, which include: 1) the type of TL used, which deals with the geometry of the line; 2) the height of the intermediate interface for the TLs, that allows the lines to be moved apart more; 3) the percentage of the way between the taper bounding location and the element at which an intermediate interface is located; 4) the position of the lens terminations (i.e., connectors or array elements) from the bounding location; 5) the spacing between each beam, array, and dummy terminal connections; 6) the curvature of the lines from the lens beam taper points to the connection terminals.

References

[1] M. Agiwal, A. Roy, and N. Saxena, "Next generation 5G wireless networks: A comprehensive survey," *IEEE Communications Surveys & Tutorials*, vol. 18, no. 3, pp. 1617–1655, Third Quarter 2016.

[2] M. Shafi *et al.*, "5G: A tutorial overview of standards, trials, challenges, deployment, and practice," *IEEE J. Selected Areas in Communications*, vol. 35, no. 6, pp. 1201–1221, Jun. 2017.

[3] C. Dehos *et al.*, "Millimeter-wave access and backhauling: The solution to the exponential data traffic increase in 5G mobile communications systems?," *IEEE Communications Magazine*, vol. 52, no. 9, pp. 88–95, Sep. 2014.

[4] T. S. Rappaport *et al.*, "Millimeter wave mobile communications for 5G cellular: It will work!," *IEEE Access*, vol. 1, pp. 335–349, May 2013.

[5] Y. Zhu *et al.*, "Demystifying 60GHz outdoor picocells," in *20th Annual International Conference on Mobile Computing and Networking (MobiCom)*, Sep. 2014, pp. 5–16.

[6] L. Verma, M. Fakharzadeh, and S. Choi, "Backhaul need for speed: 60 GHz is the solution," *IEEE Wireless Communications*, vol. 22, no. 6, pp. 114–121, Dec. 2015.

[7] Q.-U.-A. Nadeem *et al.*, "3D massive MIMO systems: Modeling and performance analysis," *IEEE Transactions on Wireless Communications*, vol. 14, no. 12, pp. 6926–6939, Dec. 2015.

[8] X. Ge *et al.*, "5G wireless backhaul networks: Challenges and research advances," *IEEE Network*, vol. 28, no. 6, pp. 6–11, Nov.-Dec. 2014.

[9] C. Masouros *et al.*, "Large scale antenna arrays with increasing antennas in limited physical space," *China Communications*, vol. 11, no. 11, pp. 7–15, Nov. 2014.

[10] C.-M. Chen *et al.*, "Finite large antenna arrays for massive MIMO: Characterisation and system impact," *IEEE Transactions on Antennas and Propagation*, vol. 65, no. 12, pp. 6712–6720, Dec. 2017.

[11] I. Uchendu and J. R. Kelly, "Survey of beam steering techniques available for millimeter wave applications," *Progress In Electromagnetics Research B*, Vol. 68, pp. 35–54, 2016.

[12] A. Rahimian and F. Mehran, "RF link budget analysis in urban propagation microcell environment for mobile radio communication systems link planning," in *International Conference on Wireless Communications and Signal Processing (WCSP)*, Nov. 2011, pp. 1–5.

[13] L. C. Godara, "Applications of antenna arrays to mobile communications, part I: Performance improvement, feasibility, and system considerations," *Proceedings of the IEEE*, vol. 85, no. 7, pp. 1031–1060, Jul. 1997.

[14] L. C. Godara, "Application of antenna arrays to mobile communications, part II: Beam-forming and direction-of-arrival considerations," *Proceedings of the IEEE*, vol. 85, no. 8, pp. 1195–1245, Aug. 1997.

[15] J. Zhang *et al.*, "5G millimeter-wave antenna array: Design and challenges," *IEEE Wireless Communications*, vol. 24, no. 2, pp. 106–112, Apr. 2017.

[16] C.-X. Mao, S. Gao, and Y. Wang, "Broadband high-gain beam-scanning antenna array for millimeter-wave applications," *IEEE Transactions on Antennas and Propagation*, vol. 65, no. 9, pp. 4864–4868, Sep. 2017.

[17] W. Hong, "Solving the 5G mobile antenna puzzle: Assessing future directions for the 5G mobile antenna paradigm shift," *IEEE Microwave Magazine*, vol. 18, no. 7, pp. 86–102, Nov. -Dec. 2017.

[18] F. Sohrabi and W. Yu, “Hybrid digital and analog beamforming design for large-scale antenna arrays,” *IEEE Journal of Selected Topics in Signal Processing*, vol. 10, no. 3, pp. 501–513, Apr. 2016.

[19] S. Payami, M. Ghoraishi and M. Dianati, “Hybrid beamforming for large antenna arrays with phase shifter selection,” *IEEE Transactions on Wireless Communications*, vol. 15, no. 11, pp. 7258–7271, Nov. 2016.

[20] A. F. Molisch *et al.*, “Hybrid beamforming for massive MIMO: A survey,” *IEEE Communications Magazine*, vol. 55, no. 9, pp. 134–141, Sep. 2017.

[21] F. Sohrabi and W. Yu, “Hybrid analog and digital beamforming for mmWave OFDM large-scale antenna arrays,” *IEEE Journal on Selected Areas in Communications*, vol. 35, no. 7, pp. 1432–1443, Jul. 2017.

[22] Q. Bai and R. Langley, “Crumpling of PIFA textile antenna,” *IEEE Transactions on Antennas and Propagation*, vol. 60, no. 1, pp. 63–70, Jan. 2012.

[23] Q. Bai, J. Rigelsford, and R. Langley, “Crumpling of microstrip antenna array,” *IEEE Transactions on Antennas and Propagation*, vol. 61, no. 9, pp. 4567–4576, Sep. 2013.

[24] V. Semkin *et al.*, “Beam switching conformal antenna array for mm-wave communications,” *IEEE Antennas and Wireless Propagation Letters*, vol. 15, pp. 28–31, 2016.

[25] D. Betancourt *et al.*, “Bending and folding effect study of flexible fully printed and late-stage codified octagonal chipless RFID tags,” *IEEE Transactions on Antennas and Propagation*, vol. 64, no. 7, pp. 2815–2823, Jul. 2016.

[26] J. G. D. Hester, J. Kimionis, and M. M. Tentzeris, “Printed motes for IoT wireless networks: State of the art, challenges, and outlooks,” *IEEE Transactions on Microwave Theory and Techniques*, vol. 65, no. 5, pp. 1819–1830, May 2017.

[27] Y. Xia, B. Muneer, and Q. Zhu, "Design of a full solid angle scanning cylindrical-and-conical phased array antennas," *IEEE Transactions on Antennas and Propagation*, vol. 65, no. 9, pp. 4645–4655, Sep. 2017.

[28] K. A. Yinusa, "A dual-band conformal antenna for GNSS applications in small cylindrical structures," *IEEE Antennas and Wireless Propagation Letters*, vol. 17, no. 6, pp. 1056–1059, Jun. 2018.

[29] J. Jang *et al.*, "Smart small cell with hybrid beamforming for 5G: Theoretical feasibility and prototype results," *IEEE Wireless Communications*, vol. 23, no. 6, pp. 124–131, 2016.

[30] A. I. Zaghloul, S. J. Weiss, W. K. Coburn, "Antenna developments for military applications," *ACES Journal*, vol. 25, no. 1, pp. 41–53, Jan. 2010.

[31] N. J. G. Fonseca, A. Ali and H. Aubert, "Cancellation of beam squint with frequency in serial beamforming network-fed linear array antennas," *IEEE Antennas and Propagation Magazine*, vol. 54, no. 1, pp. 32–39, Feb. 2012.

[32] A. Rahimian, "Investigation of Nolen matrix beamformer usability for capacity analysis in wireless MIMO systems," in *19th Asia-Pacific Conference on Communications (APCC)*, Aug. 2013, pp. 622–623.

[33] C. E. Patterson *et al.*, "A 60-GHz active receiving switched-beam antenna array with integrated Butler matrix and GaAs amplifiers," *IEEE Transactions on Microwave Theory and Techniques*, vol. 60, no. 11, pp. 3599–3607, Nov. 2012.

[34] W. Rotman and R. Turner, "Wide-angle microwave lens for line source applications," *IEEE Transactions on Antennas and Propagation*, vol. 11, no. 6, pp. 623–632, Nov. 1963.

[35] A. G. Anbaran, A. Mohammadi, and A. Abdipour, "Capacity enhancement of ad hoc networks using a new single-RF compact beamforming scheme," *IEEE Transactions on Antennas and Propagation*, vol. 63, no. 11, pp. 5026–5034, Nov. 2015.

[36] V. Venkateswaran, F. Pivit, and L. Guan, “Hybrid RF and digital beamformer for cellular networks: Algorithms, microwave architectures, and measurements,” *IEEE Transactions on Microwave Theory and Techniques*, vol. 64, no. 7, pp. 2226–2243, Jul. 2016.

[37] F. Foglia Manzillo *et al.*, “A multilayer LTCC solution for integrating 5G access point antenna modules,” *IEEE Transactions on Microwave Theory and Techniques*, vol. 64, no. 7, pp. 2272–2283, Jul. 2016.

[38] B. Avser, J. Pierro, and G. M. Rebeiz, “Random feeding networks for reducing the number of phase shifters in limited-scan arrays,” *IEEE Transactions on Antennas and Propagation*, vol. 64, no. 11, pp. 4648–4658, Nov. 2016.

[39] K. Tekkouk *et al.*, “Wideband and large coverage continuous beam steering antenna in the 60-GHz band,” *IEEE Transactions on Antennas and Propagation*, vol. 65, no. 9, pp. 4418–4426, Sep. 2017.

[40] H. T. Chou and H. J. Huang, “Multilevel subarray modularization to construct hierarchical beamforming networks for phased array of antennas with low complexity,” *IEEE Transactions on Antennas and Propagation*, vol. 65, no. 11, pp. 5819–5828, Nov. 2017.

[41] G. de Alwis and M. Delahoy, “60 GHz band millimetre wave technology,” *Australian Communications and Media Authority (ACMA)*, pp. 1–32, Dec. 2004.

[42] A. V. Raisanen and A. Lehto, *Radio Engineering for Wireless Communication and Sensor Applications*, Artech House, 2003.

[43] C. A. Balanis, *Antenna Theory: Analysis and Design, 4th Edition*, John Wiley & Sons, 2016.

[44] R. C. Hansen, *Phased Array Antennas, 2nd Edition*, John Wiley & Sons, 2009.

[45] P. S. Hall and S. J. Vetterlein, "Review of radio frequency beamforming techniques for scanned and multiple beam antennas," *IEE Proceedings H - Microwaves, Antennas and Propagation*, vol. 137, no. 5, pp. 293–303, Oct. 1990.

[46] R. C. Hansen, "Design trades for Rotman lenses," *IEEE Transactions on Antennas and Propagation*, vol. 39, no. 4, pp. 464–472, Apr. 1991.

[47] P. K. Singhal, R. D. Gupta, and P. C. Sharma, "Recent trends in design and analysis of Rotman-type lens for multiple beamforming," *International Journal of RF and Microwave Computer-Aided Engineering*, vol. 8, no. 4, pp. 321–338, Jul. 1998.

[48] P. S. Simon, "Analysis and synthesis of Rotman lenses," in *22nd AIAA International Communications Satellite Systems Conference & Exhibit (ICSSC)*, May 2004, pp. 1–11.

[49] C. Penney, "Rotman lens design and simulation in software," *IEEE Microwave Magazine*, vol. 9, no. 6, pp. 138–139, Dec. 2008.

[50] J. Dong and A. I. Zaghloul, "Extremely high-frequency beam steerable lens-fed antenna for vehicular sensor applications," *IET Microwaves, Antennas & Propagation*, vol. 4, no. 10, pp. 1549–1558, Oct. 2010.

[Online]. Available: https://vtechworks.lib.vt.edu/handle/10919/29081.

[51] W. Zongxin *et al.*, "A multibeam antenna array based on printed Rotman lens," *International Journal of Antennas and Propagation*, article ID: 179327, pp. 1–6, 2013.

[52] A. Rahimian, "Design and performance of a Ku-band Rotman lens beamforming network for satellite systems," *Progress In Electromagnetics Research M*, vol. 28, pp. 41–55, 2013.

[53] S. Vashist, M. K. Soni, and P. K. Singhal, "A review on the development of Rotman lens antenna," *Chinese Journal of Engineering*, vol. 2014, article ID: 385385, pp. 1–9, Jul. 2014.

[54] M. Rajabalian and B. Zakeri, “Optimisation and implementation for a non-focal Rotman lens design,” *IET Microwaves, Antennas & Propagation*, vol. 9, no. 9, pp. 982–987, Jun. 2015.

[55] R. Rotman, M. Tur, and L. Yaron, “True time delay in phased arrays,” *Proceedings of the IEEE*, vol. 104, no. 3, pp. 504–518, Mar. 2016.

[56] H. Liao, “CMOS-based microwave and millimeter wave phased antenna arrays and applications,” *Ph.D. dissertation*, University of California, Davis, 2013.

[57] W. Lee *et al.*, “Compact two-layer Rotman lens-fed microstrip antenna array at 24 GHz,” *IEEE Transactions on Antennas and Propagation*, vol. 59, no. 2, pp. 460–466, Feb. 2011.

[58] J. Kim *et al.*, “Asymmetric ground Rotman lens for multilayer packages,” *IEEE Microwave and Wireless Components Letters*, vol. 24, no. 5, pp. 303–305, May 2014.

[59] I. S. Song *et al.*, “60GHz Rotman lens and new compact low loss delay line using LTCC technology,” in *IEEE Radio and Wireless Symposium (RWS)*, Jan. 2009, pp. 663–666.

[60] W. Lee *et al.*, “Beamforming lens antenna on a high resistivity silicon wafer for 60 GHz WPAN,” *IEEE Transactions on Antennas and Propagation*, vol. 58, no. 3, pp. 706–713, 2010.

[61] S. Lee *et al.*, “A V-band beam-steering antenna on a thin-film substrate with a flip-chip interconnection,” *IEEE Microwave and Wireless Components Letters*, vol. 18, no. 4, pp. 287–289, Apr. 2008.

[62] I. Ju *et al.*, “V-band beam-steering ASK transmitter and receiver using BCB-based system-on-package technology on silicon mother board,” *IEEE Microwave and Wireless Components Letters*, vol. 21, no. 11, pp. 619–621, Nov. 2011.

[63] K. Tekkouk *et al.*, “Multibeam SIW slotted waveguide antenna system fed by a compact dual-layer Rotman lens,” *IEEE Transactions on Antennas and Propagation*, vol. 64, no. 2, pp. 504–514, Feb. 2016.

[64] N. Jastram and D. S. Filipovic, “Design of a wideband millimeter wave micromachined Rotman lens,” *IEEE Transactions on Antennas and Propagation*, vol. 63, no. 6, pp. 2790–2796, Jun. 2015.

[65] C.-L. Cho *et al.*, “Inkjet-printed multilayer bandpass filter using liquid crystal polymer system-on-package technology,” *IEEE Transactions on Components, Packaging and Manufacturing Technology*, vol. 6, no. 4, pp. 622–629, Apr. 2016.

[66] P. Cabrol and P. Pietraski, “60 GHz patch antenna array on low cost liquid-crystal polymer (LCP) substrate,” in *IEEE Long Island Systems, Applications and Technology Conference (LISAT)*, May 2014, pp. 1–6.

[67] D. Liu and Y. P. Zhang, “Integration of array antennas in chip package for 60-GHz radios,” *Proceedings of the IEEE*, vol. 100, no. 7, pp. 2364–2371, Jul. 2012.

[68] N. Kingsley, G. E. Ponchak, and J. Papapolymerou, “Reconfigurable RF MEMS phased array antenna integrated within a liquid crystal polymer (LCP) system-on-package,” *IEEE Transactions on Antennas and Propagation*, vol. 56, no. 1, pp. 108–118, Jan. 2008.

[69] A. Lamminen *et al.*, “Dual-circular polarised patch antenna array on LCP for 60 GHz millimetre-wave identification,” in *8th European Conference on Antennas and Propagation (EuCAP)*, Apr. 2014, pp. 537–541.

[70] J. Saily *et al.*, “Millimetre-wave beam-switching Rotman lens antenna designs on multi-layered LCP substrates,” in *10th European Conference on Antennas and Propagation (EuCAP)*, Apr. 2016, pp. 1–5.

[Online]. Available: https://www.mathworks.com/matlabcentral/fileexchange/50490-rotman-lens-design-with-hfss-link.

[71] A. Lamminen *et al.*, "Gain enhanced millimetre-wave beam-switching Rotman lens antenna designs on LCP," in *11th European Conference on Antennas and Propagation (EuCAP)*, Mar. 2017, pp. 2781–2785.

[72] T. K. Vo Dai and O. Kilic, "Compact Rotman lens structure configurations to support millimetre wave devices," *Progress In Electromagnetics Research B*, vol. 71, pp. 91–106, 2016.

[73] D. C. Thompson *et al.*, "Characterization of liquid crystal polymer (LCP) material and transmission lines on LCP substrates from 30 to 110 GHz," *IEEE Transactions on Microwave Theory and Techniques*, vol. 52, no. 4, pp. 1343–1352, Apr. 2004.

[74] R. Hosono *et al.*, "Development of millimeter-wave devices based on liquid crystal polymer (LCP) substrate," *IEICE Electronics Express*, vol. 14, no. 20, pp. 1–13, Oct. 2017.

[75] M. Clemens and T. Weiland, "Discrete electromagnetism with the finite integration technique," *Progress In Electromagnetics Research*, vol. 32, pp. 65–87, 2001.

[76] T. Weiland, M. Timm, and I. Munteanu, "A practical guide to 3-D simulation," *IEEE Microwave Magazine*, vol. 9, no. 6, pp. 62–75, Dec. 2008.

[77] T. Weiland, "Electromagnetic simulators – status and future directions," *IET Science, Measurement & Technology*, vol. 11, no. 6, pp. 681–686, Sep. 2017.

[78] A. Attaran and S. Chowdhury, "Fabrication of a 77 GHz Rotman lens on a high resistivity silicon wafer using lift-off process," *International Journal of Antennas and Propagation*, vol. 2014, 471935, pp. 1–9, 2014.

[79] J. M. Mesquita *et al.*, "Influence of deformations on the matching of a flexible dual-band antenna," in *7th European Conference on Antennas and Propagation (EuCAP)*, Apr. 2013, pp. 3283–3285.

[80] H. L. Kao *et al.*, "Bending effect of an inkjet-printed series-fed two-dipole antenna on a liquid crystal polymer substrate," *IEEE Antennas and Wireless Propagation Letters*, vol. 13, pp. 1172–1175, 2014.

[81] S. M. Saeed, C. A. Balanis, and C. R. Birtcher, "Inkjet-printed flexible reconfigurable antenna for conformal WLAN/WiMAX wireless devices," *IEEE Antennas and Wireless Propagation Letters*, vol. 15, pp. 1979–1982, 2016.

[82] A. Alemaryeen and S. Noghanian, "Crumpling effects and specific absorption rates of flexible AMC integrated antennas," *IET Microwaves, Antennas & Propagation*, vol. 12, no. 4, pp. 627–635, Mar. 2018.

[83] Z. Hamouda *et al.*, "Flexible UWB organic antenna for wearable technologies application," *IET Microwaves, Antennas & Propagation*, vol. 12, no. 2, pp. 160–166, Feb. 2018.

[84] L. Song and Y. Rahmat-Samii, "A systematic investigation of rectangular patch antenna bending effects for wearable applications," *IEEE Transactions on Antennas and Propagation*, vol. 66, no. 5, pp. 2219–2228, May 2018.

[85] S. Kutty and D. Sen, "Beamforming for millimetre wave communications: An inclusive survey," *IEEE Communications Surveys & Tutorials*, vol. 18, no. 2, pp. 949–973, Second Quarter 2016.

[86] J. Ala-Laurinaho *et al.*, "2-D beam-steerable integrated lens antenna system for 5G E-band access and backhaul," *IEEE Transactions on Microwave Theory and Techniques*, vol. 64, no. 7, pp. 2244–2255, Jul. 2016.

[87] M. Xiao *et al.*, "Millimeter wave communications for future mobile networks," *IEEE Journal on Selected Areas in Communications*, vol. 35, no. 9, pp. 1909–1935, Sep. 2017.

[88] X. Wang *et al.*, "Millimeter wave communication: A comprehensive survey," *IEEE Communications Surveys & Tutorials*, vol. 20, no. 3, pp. 1616–1653, Third Quarter 2018.

[89] B. Yang *et al.*, "Digital beamforming-based massive MIMO transceiver for 5G millimeter-wave communications," *IEEE Transactions on Microwave Theory and Techniques*, vol. 66, no. 7, pp. 3403–3418, Jul. 2018.

[90] A. T. Castro and S. K. Sharma, "Inkjet-printed wideband circularly polarized microstrip patch array antenna on a PET film flexible substrate material," *IEEE Antennas and Wireless Propagation Letters*, vol. 17, no. 1, pp. 176–179, Jan. 2018.

[91] M. Tighezza *et al.*, "Flexible wideband antenna for 5G applications," *Microwave and Optical Technology Letters*, vol. 60, no. 1, pp. 38–44, Jan. 2018.

[92] J. Pourahmadazar and T. A. Denidni, "Millimeter-wave planar antenna on flexible polyethylene terephthalate substrate with water base silver nanoparticles conductive ink," *Microwave and Optical Technology Letters*, vol. 60, no. 4, pp. 887–891, Apr. 2018.

[93] M. A. Monne *et al.*, "Inkjet-printed flexible MEMS switches for phased-array antennas," *International Journal of Antennas and Propagation*, vol. 2018, 4517848, pp. 1–10, Mar. 2018.

[94] J. Du and C. Roblin, "Stochastic surrogate models of deformable antennas based on vector spherical harmonics and polynomial chaos expansions: Application to textile antennas," *IEEE Transactions on Antennas and Propagation*, vol. 66, no. 7, pp. 3610–3622, Jul. 2018.

[95] M. A. Al-Tarifi, M. S. Sharawi, and A. Shamim, "Massive MIMO antenna system for 5G base stations with directive ports and switched beamsteering capabilities," *IET Microwaves, Antennas & Propagation*, vol. 12, no. 10, pp. 1709–1718, Aug. 2018.

[96] S. F. Jilani *et al.*, "Low-profile flexible frequency-reconfigurable millimetre-wave antenna for 5G applications," *Flexible and Printed Electronics*, vol. 3, no. 3, 035003, pp. 1–8, Aug. 2018.